Università degli Studi della Basilicata

PhD Program

SCIENCES

Curriculum: Geo-Sciences

GEOCHEMISTRY OF PALEOFLUIDS IN MINERALIZATION ALONG SEISMOGENIC FAULTS IN THE IRPINIA AREA (SOUTHERN ITALY)

Scientific disciplinary sector:

Geochemistry and Volcanology, Geo/08

PhD Pragram Coordinator:

Prof.ssa Patrizia Falabella

PhD Candidate:

Filippo Zummo

Supervisor:

Prof. Michele Paternoster (DISBA, Unibas)

Co-Advisor:

Dott. Antonio Caracausi (INGV, Palermo)

Prof. Fabrizio Agosta (DISBA, Unibas)

XXXVII Cycle

PhD Program

SCIENCES

Curriculum: Geo-Sciences

GEOCHEMISTRY OF PALEOFLUIDS IN MINERALIZATION ALONG SEISMOGENIC FAULTS IN THE IRPINIA AREA (SOUTHERN ITALY)

Scientific disciplinary sector:

Geochemistry and Volcanology, Geo/08

PhD Pragram Coordinator:

Prof.ssa Patrizia Falabella

PhD Candidate:

Filippo Zummo

Supervisor:

Prof. Michele Paternoster (DISBA, Unibas)

Co-Advisor:

Dott. Antonio Caracausi (INGV, Palermo)

Prof. Fabrizio Agosta (DISBA, Unibas)

XXXVII Cycle

INDEX

Abstract

The present PhD Thesis Dissertation includes the results of a integrated and multidisciplinary study of fault-related calcite veins from the Contursi Hydrothermal basin (Irpinia area, southern Italy). The whole Contursi hydrothermal activity takes place within a seismically active portion of the southern Apennines of Italy, where destructive earthquakes unfortunately have occurred in recent times. The Contursi village lies close (ca. 1 – 5 km) to the epicentral area of the M_W = 6.9, 1980 Irpinia earthquake, and the local fault system is well-exposed along the numerous fault scarps dissecting Mesozoic shallow-water carbonates pertaining to the Apennine Platform. The Contursi hydrothermal activity is characterized by the outgassing of deep sourced CO_2 coupled with mantle-derived volatiles such as He (Buttitta et al., 2023). In order to gain news insight into the modalities of crustal-scale fluid circulation along active extensional fault systems, in this work I has been investigated the paleofluids that precipitated calcite minerals within fault-related veins of the aforementioned Contursi Hydrothermal Basin. Specifically, tackle the source of the mineralizing paleofluids and the modalities of fault-related fluid circulation by integrating the results of field structural studies with microstructural, stable isotopes ($\delta^{13}C$ and $\delta^{18}O$) and trace elements characterizations of the calcite veins, and both noble gases and δD-H_2O of Fluid Inclusion (FI).

The studied fault-related calcite veins crosscut the Mesozoic Apennine Carbonate platform exposed in the Contursi area, which is about 40 km^2-wide and characterized by the exposure of high-angle fault forming two main sets roughly striking NNW-SSE and ENE-WSW, respectively. There, in close proximity to the main slip surfaces, both comb and slip-parallel calcite veins (labelled as C and SP, respectively) were sampled. In accordance with previous works, both C and SP-veins are interpreted as co-seismic or early post-seismic features, whose formation as brittle extensional fractures occurred during multiple seismic ruptures. Most of the sampled fault-related calcite veins include blocky calcite crystals, whose precipitation from the fault-controlled paleofluids, likely post-dated the occurrence of the aforementioned brittle fracturing. Only two samples show a fibrous texture of the calcite crystals, which are interpreted as syn-kinematics, and formed during small increments of shear-induce dilation and mineral precipitation. Due to their variable sized and inner texture, incremental crack and seal processes are documented for some studied calcite veins samples.

Most of calcite veins samples show $\delta^{13}C$ and $\delta^{18}O$ values similar to those that characterize the Mesozoic marine carbonate field (Apennine Carbonate platform). Such an isotopic signature is consistent with mineral precipitation form paleofluids in an isotopic equilibrium with the encompassing carbonate host rocks. This interpretation is supported by the calculated $\delta^{18}O_{parentalfluids}$ values, δD values measured in Fluid Inclusion (FI) and trace and REE content, which all point out towards the long residence time of the mineralizing fluids within the faulted carbonate host rocks. In addition, since the homogenization temperatures (between 100 °C and 130°C) obtained by FIs analysis are similar to the maximum burial temperatures experienced by the Apennine Carbonate Platform host rock (100°C – 120°C), assuming a geothermal gradient of ~30 °C/km, and taking known values of groundwater

temperature into account, the geochemical data are interpreted as due calcite precipitation within the fault-related veins from paleofluids that localized at depths of ca. 3 ~ 4 km, and interacted with the Mesozoic carbonates. Differently, some calcite veins are characterized by $\delta^{13}C$ values similar to those reported above, but by a pronounced depletion in $\delta^{18}O$ which, together with the high homogenization temperature assessed for the FIs, are consistent with the paleofluids derived from a deep reservoir from depths of ca. 8 ~ 10 km. Accordingly, similar to the conceptual model invoked for crustal-scale fault-related fluid flow in the High Agri Valley of southern Italy, results point out to an ascendance of deep fluids towards the Earth's surface that likely occurred thanks to the temporary rupture of the tectonic mélange forming the sole thrust of the southern Apennine fold-and-thrust belt, and the main seal of overpressurized fluids entrapped within the Apulian carbonates.

Regarding to the results of noble gases analyses performed on the FIs trapped within the calcite veins, most of the investigated samples shows R/Ra values comprised between 0.53 and 1.38 Ra, which is consistent with a prevalent crustal component added to mantle one (up to 20%), and also with a negligible meteoric component. The variability of He isotopic signature in the FIs, that is not consistent with narrower range of He ratios for the current outgassing, can be due to early trapping processes (probably earthquakes occurred in the past). Based on co-seismic dilatancy model, an "early trapping" hypothesis for He isotopic signal, the following model of fault-related fluid circulation in the Contursi Hydrothermal basin is here proposed: the co-seismic dilatancy formed transient of high-permeability pathways through the upper crust, allowing the ascendence of likely overpressured fluids from rock volumes underneath the impermeable tectonic mélange made up of Apulian carbonates. During ascendence towards the Earth's surface, these overpressured fluids characterized by crustal and mantle derived He (up to 20%), reached shallower crustal volumes (1-5 km), and were either in thermal and isotopic equilibrium or in disequilibrium with the Apennine carbonates generating the two distinct groups of calcite veins and associated FIs. For the fluids in thermal and isotopic equilibrium with the Apennine carbonate host rock, the mixing with the meteoric and/or shallow derived fluid cannot be excluded, as demonstrated through noble gas analysis (i. e. $^{40}Ar/^{36}Ar$ and relationship with R/Ra values) of some of the study samples. The high-permeability pathways permitting the rapid ascendance of deeper fluids towards shallow crustal conditions is still active in the Irpinia area, as suggested by soil gas measurements indicating a current outgassing of mantle-derived fluids. However, regarding the mantle component measured in the study sample, two possible scenarios are envisioned. First, the mantle-derived fluids derive from outgassing of magmatic intrusion at depth. Second, a through-going structural discontinuity that crosscut the whole crust down to the mantle channeled the deep fluids a depth.

In conclusion, the results of this study showed that the Contursi hydrothermal basin forms a great natural laboratory to gaining a new knowledge on modalities of crustal-scale fluid circulation associated with crustal deformation and earthquake faulting. Such investigations are fundamental to understanding the role of deep fluids in crustal deformation over time, and in the processes of earthquakes nucleation and rupture propagation. Moreover, this

study provides hints upon long-time multidisciplinary integrated monitoring approach in tectonically active continental regions, so that the new insights can be helpful to improve earthquake forecast.

Chapter 1 – Introduction

1.1 Aim of this work

The fault-related fluid circulation in the upper crust can be governed by the spatio-temporal evolution of deformation and associated structural diagenesis of the fault rocks and associated fault-related fractured rock volumes (Sibson, 2000; Balsamo et al., 2016; Ferraro et al., 2020). Such an evolution is forming an even more puzzling problem if associated with the seismic cycles characterizing active faults. This makes challenging to interpret the episodes of fluid ascendance from depth along seismically active fault zones. For this reason, the analysis of fault-related mineralization is key to assess the fluid origin, the modalities of fluid circulation through the fault zones, and the extent of fluid-rock interactions (Agosta and Kirschner, 2003; Buttitta et al., 2023; Marchesini et al., 2022; Randazzo et al., 2021; Smeraglia et al., 2016 and 2018).

In the analysis of the fault rocks and fault-related fractures exhumed form shallow crustal levels, the dilution of deep-seated fluids with the local groundwater and/or atmospheric fluids might mask the original isotopic signature of the former. In fact, the reactive volatiles (e.g. CO_2) dissolved in water are speciated (e.g. carbonate equilibrium), and their concentration and isotopic composition are modified by water-gas-rock interaction processes and solute precipitation (Gilfillan et al., 2009). In this regard, noble gases, chemically inert elements, are excellent tracers of both fluid sources and physical processes within the crust (Caracausi and Paternoster, 2015; Curzi et al., 2022; Kendrick and Burnard, 2013; Pik and Marty, 2009). He is the lightest of noble gases and in natural fluids is present as two isotopes, ^3He and ^4He, with the former being mainly primordial and stored in the mantle, and the latter continuously produced by the decay of U and Th in the Earth's interior (Ozima and Podosek, 2002). In stable continental regions, the He flux is dominated by the radiogenic ^4He produced in the crust (O'Nions and Oxburgh, 1988). In contrast, the primordial ^3He escapes to the atmosphere in regions exhibiting active tectonics and volcanism; this makes the He isotopic ratio ($^3He/^4He$) a powerful tool for recognizing mantle and crust components in absence of other geological and geochemical evidence (e.g. Caracausi and Sulli, 2019; O'Nions and Oxburg, 1983; Boles et al., 2015). Worldwide, regions characterized by high magnitudes earthquakes such as California, USA, SW Japan, the Anatolian Plateau, Turkey, eastern Tibetan Plateau and both Belice and Irpinia in Italy, exhibit a crustal ^4He released from the seismogenic faults diluted with a mantle-derived He component (Boles et al., 2015; Caracausi et al., 2005; Dogan et al., 2009; Italiano et al., 2000; Liu et al., 2023; Kulongoski et al., 2013; Sano et al., 2016 Zhang et al., 2021). Recently, it has been shown that this dilution varies spatially in accordance with the distribution of seismicity (Caracausi et al., 2022). Moreover, such a dilution might also vary over time as observed during the Kumamoto 2016 earthquake (Japan, Mw = 7.3), reflecting the earthquake magnitude, the host rock lithology, and the seismic cycle (Sano et al., 2016).

Fluid ingress and circulation during fault activity is documented by the presence of tectonic mineralization, such as slickenfibers, veins (Sibson, 1992 and 2000; Schirripa Spagnolo et al., 2024 and reference therein) which

precipitate during different phases of the seismic cycle (e.g., Uysal et al., 2011; Smeraglia et al., 2016; Unal-Imer et al., 2016; Coppola et al., 2021). In this regard, the veins along faults can record episodes of dynamic dilatation and potentially fracturing during seismic events (Boullier et al., 2004; Williams et al., 2017; Smeraglia et al., 2018). For this reason, the study of fault-related veins and eventually fluid inclusions trapped within minerals represents phases of geological activity that occurred with crustal deformation and possibly with past high-magnitude earthquakes occurred in the studied area. The Fluid Inclusions (FIs) are considered as a small volume of paleo-fluids (gas and liquid), entrapped within host minerals and provides indispensable information about geological processes, such as temperature and pressure of homogenization and entrainment (from high temperatures at depth towards low temperature near Earth's surface). The study of abundance, orientation and chemistry of FIs provides a history of formation and alteration over time (Randive et al., 2014; Goldstein, 2003).

In this framework, the Contursi Hydrothermal basin (Irpinia, southern Italy) is located in the western portion of the southern Apennines fold-and-thrust belt. This belt developed since Oligo-Miocene times due to the progressive collision between the African and European plates, and interactions with the intervening Adria-Apula plate (Patacca et al., 1990). Regional-scale thrusting took place by mean of both thin-skinned and thick-skinned tectonics (Shiner et al., 2004), forming a complex multi-duplex that now day trending approximately N150° direction, subparallel to the strike direction of the main thrust faults (Patacca and Scandone, 2007). The structural pattern of the Contursi hydrothermal basin has been interpreted as a N-S trending graben where the main discontinuities border the high relief massifs of Mesozoic carbonate rocks. Starting from post orogenic deformation, the axial zone of the southern Apennines has been dissected by NW-SE striking seismogenic faults with depth up to 15 km (Ascione et al., 2013; Amoroso et al., 2017).

This latter basin is close to the epicentral area of the Mw 6.9 Irpinia earthquake (November 1980, Bernard and Zollo, 1989), which is between 1 and 5 km away from the Contursi town. The seismic volume responsible of the 1980 earthquake is characterized by high values of fracture porosity, and by saturated fractures (Amoroso et al., 2014, 2017). In fact, as reported by geophysical studies and continuous seismicity monitoring conducted in the study area (Amoroso et al., 2017; De Landro et al., 2022), the Vp/Vs and Vp*Vs changes are located at depths of 1-5 km and 8-12 km. The authors have demonstrated that the deeper reservoir is characterized by pulsating overpressure fluids (like CO_2), whereas it is recharged by meteoric water infiltrating downwards.

In the study area, the active faults form preferential pathways that efficiently transfer deep-seated fluids at shallow crustal levels (Buttitta et al., 2023; Caracausi and Paternoster, 2015). Such a transfer is likely due to the volumes of fault-related fractures encompassing the cataclastic fault rocks and major slip surfaces, which act as efficient fluid conduit for fault-parallel flow (Faulkner et al., 2013). In carbonates, within host rocks similar to those exposed in the Irpinia area, the high-angle extensional faults often exhibit high values of secondary porosity and permeability (Agosta et al., 2009; Giuffrida et al., 2020; Smeraglia et al., 2022), with fault rocks having lower

values of both porosity and permeability (Ferraro et al., 2020). As such, the fractured fault-related volumes might form volumetrically thick hydraulic conduits allowing fluids to adjectively ascend from the Earth's interior towards the atmosphere as documented by integrated geological and geochemical data (Caracausi et al., 2022; Curzi et al., 2022). Moreover, at Contursi, the low-enthalpy hydrothermal system characterized by a groundwater temperature in between 7 and 47 °C (Gori et al., 2023) allows the current mantle-derived He outgassing (Buttitta et al., 2023; Italiano et al., 2000). Furthermore, the nearby Mefite D'Ansanto gas emission site, about 30 km away from Contursi, shows a high heat flow with values up to ca. 215 mW/m^2 (Doglioni et al., 1996) and $^3He/^4He$ ratios up to 2.84 Ra, which is like those characterizing the active volcanoes in the Campania region of Italy (Vesuvio and Campi Flegrei), about 80 km away.

On this basis, the present PhD thesis is focused on integrated and multidisciplinary study of the fault-related calcite mineralization veins located in the Contursi hydrothermal basin and surrounding outcrops, a tectonically active area of the southern Italy where a relationship between fluid degassing and seismicity is recognized (Chiodini et al., 2004; Chiodini et., 2020; Caracausi and Paternoster 2015; Caracausi et al., 2022). Through structural and microstructural study of mineralization veins related to seismogenic fault systems, combined with geochemical and isotopic analyses, it aims to understand the fluid origin, circulation-patterns, and to provide new insights into the processes regulating paleo- and modern-fluid degassing and relationships with the seismicity and crustal deformation in tectonically active continental regions. Understanding these relationships is a crucial factor for unveiling the circulation and upwelling modes of the fluids in the crust over time and the propagation of seismogenetic faults and their modes and timing of activation. This is also crucial to open new perspective about the hazardous nature of the processes regulating the fluids degassing related to the seismic cycle and potentially earthquake processes.

1.2 Thesis organization

The research project is divided into six Chapters.

The first three chapters, concern the theoretical background, state of art, aim of work, sampling sites, geology-structural and hydrogeological setting are presented.

Particularly: ***Chapter 1*** contains a state of the art and brief introduction to the goal of this research and the thesis organization.

In ***Chapter 2:*** the main sampling sites and methods outlines used for this PhD thesis are described. ***Chapter 3:*** A geological-structural and hydrogeochemical survey of the study area is carried out. This is followed by three further chapters in which the results and discussions of structural-microstructural and geochemical-isotopic data of mineralization veins related to faults and trapped fluid inclusions are discussed. In particular, ***Chapter 4*** results from analyses of calcite veins and associated fluid inclusions are presented*:* ***Chapter 5 and Chapter 6*** discussion

of both structural-microstructural and isotopic-geochemical results on calcite veins and fluid assuming paleofluid circulation patterns model in the fault zones of the Contursi hydrothermal basin relationship with possible seismic activities. Analytical methods used for this study are described in the following Appendices:

Appendices 1: Structural and microstructural methods

Appendices 2: Geochemical and Isotopically methods

Appendices 3: Fluid inclusions (FIs) method

Parts of this thesis (*Sub-Chapters 4.1, 4.3.2* and part of *5.2)* are published in one paper in:

Zummo et al., 2024. "*Tracing a mantle component in both paleo and modern fluids along seismogenic faults of southern Italy*" Geochemistry, Geophysics, Geosystems. https://doi.org/10.1029/2024GC011816; other one is in preparation.

Chapter 2 – Sampling sites and methods

The sampling sites for the collection of calcite veins was conducted after literature review of seismically active faults in the area, which focused on the application of combined structural-microstructural and geochemical-isotopic analyses (Fig. 2.1). The PhD project mainly consisted in the following action: (i) 1:50000 scale geological map, from the available geological literature ("468 sheet Eboli" from CARG "Cartografia Geologica") used for guide sampling; (ii) mesoscale structural analysis of the outcropping faults and fractures; (iii) sampling of fault-related calcite veins; (iv) microstructural and textural analysis of the thin sections obtained from the hand samples; (v) geochemical and isotopic analysis (such as trace elements, REEY-patterns; carbon and oxygen stable isotopes in calcite minerals; (vi) Fluid Inclusions (FIs) analysis: petrographic, micro-thermometry, δD-H_2O and noble gases (He, Ne, Ar).

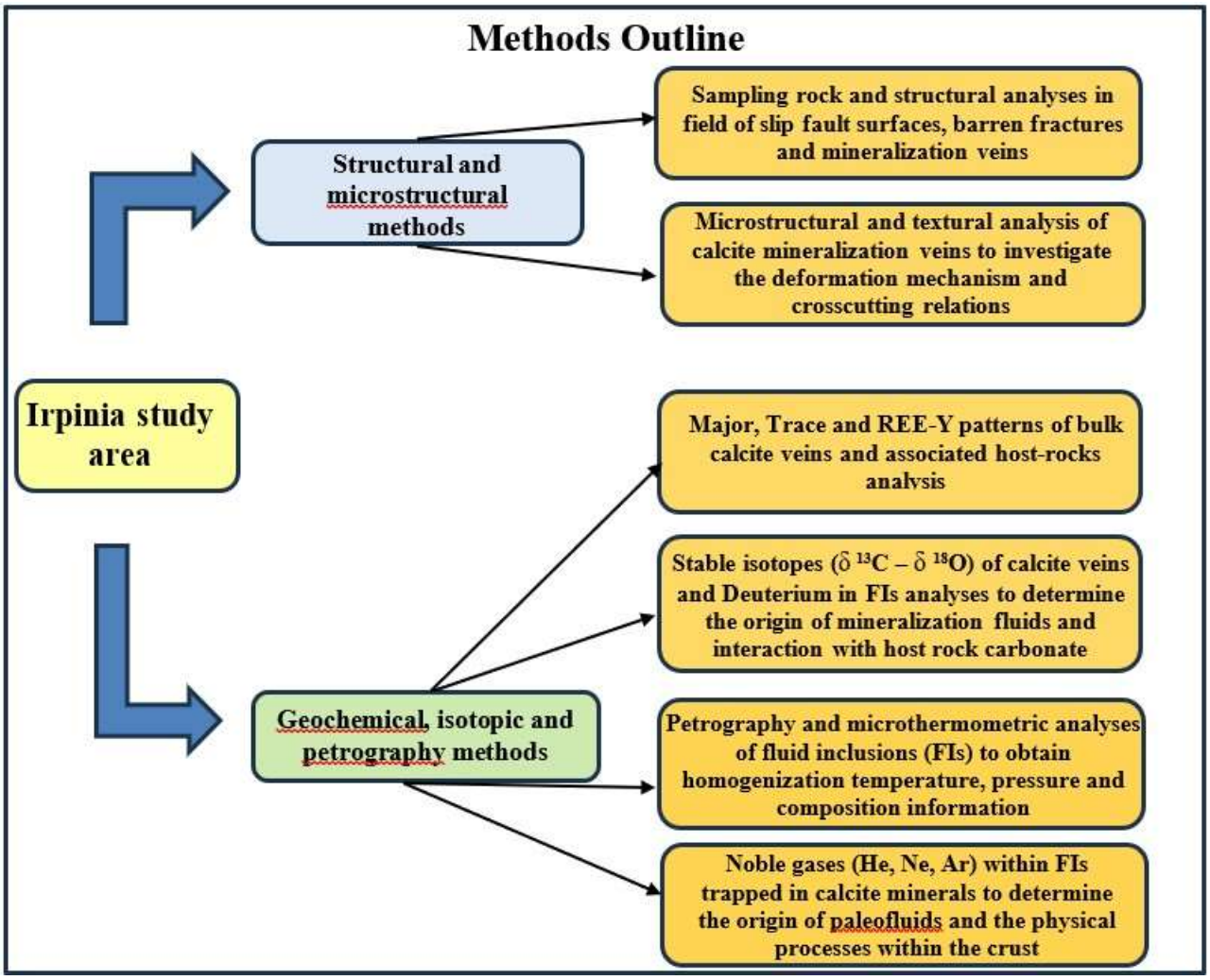

Fig. 2.1 Methods outline for the PhD thesis

2.1. SAMPLING SITES

Field activities and associated rock sampling were carried out during the years 2022 and 2023. The outcrops selected for this study were first identified by using the available 1:50.000 scale geological map of the area (468 sheet, "Eboli" CARG). Then, as it will be shown later, the collection of 18 fault-related calcite veins was carried out sampling as well as 7 host rock samples representative of two different tectonic units and 4 travertine samples found in the Tufaro's sinkhole.

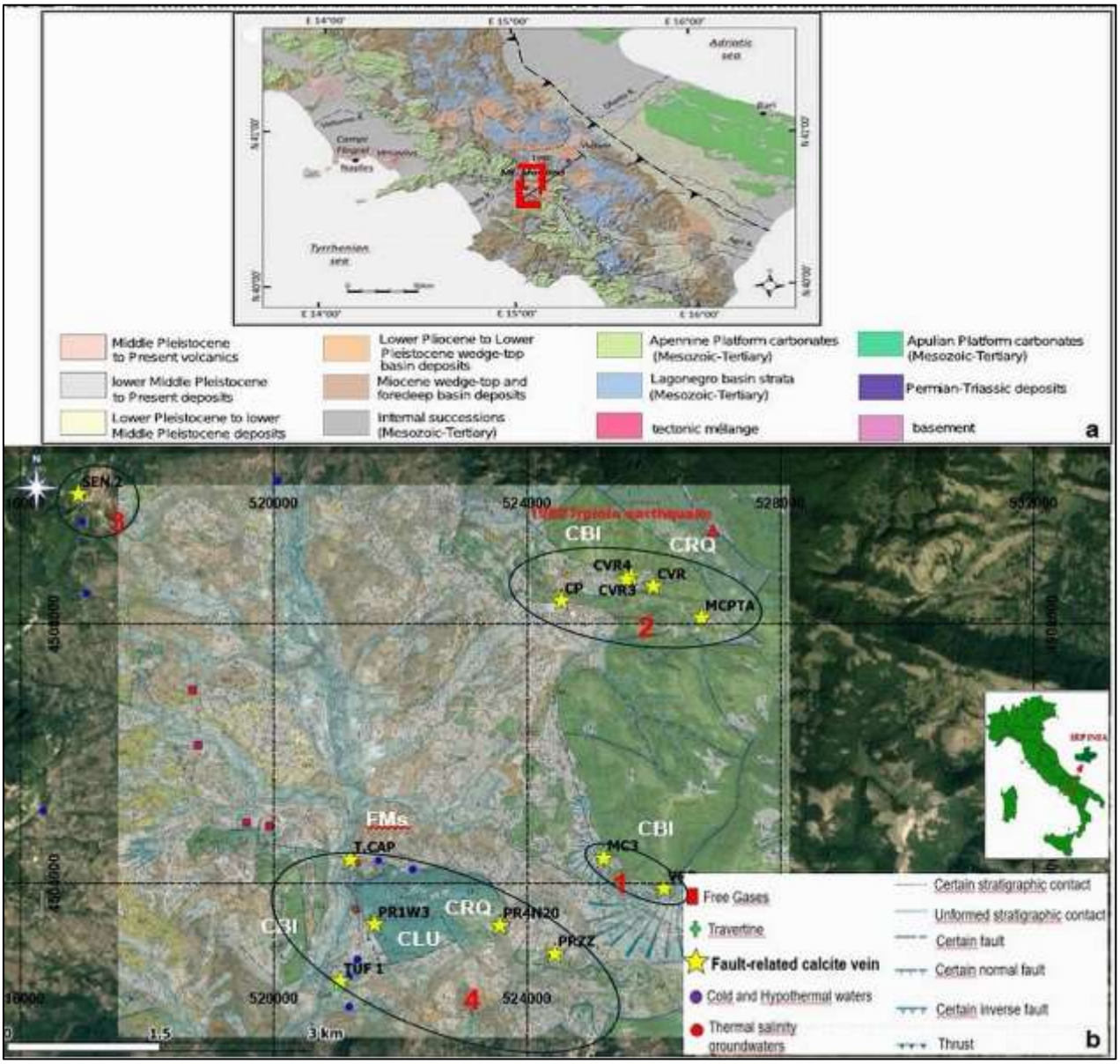

Fig.2.2 (a) *Tectonic setting of the 1980 Irpinia earthquake, and geological sketch map of the southern Apennines; in red rectangle, area for this study (modified after Ascione et al., 2013).* ***(b)*** *Detailed geological map (CARG, "CARtografia Geologica") of the study area with sampling sites of mineralization veins related to extensional fault. In details, the symbolism: the yellow stars are the sampling sites of mineralization veins in extensional fault; green crosses are the travertine deposits; red rectangles are the free gas emission in the area (Buttitta et al., 2023); red and blues circles are a warm and cold groundwater, respectively (Gori et al.,2023) and red triangle a 1980 Mw. 6.9 Irpinia earthquake (Ciotoli et al., 2013).*

Based on the spatial distribution of the sampling sites, the study area is subdivided into the following sub-areas (Fig. 2.2b):

1) Vallone Raio and Monte Castello faults;
2) Colliano and Monte Carpineta faults;
3) Senerchia area
4) Contursi hydrothermal basin: Terme Capasso - Terme Tufaro - Monte Pruno - Monte Perrazze

The list of both fault-related and host rock samples is reported in table 2.1.

The current tectono-stratigraphic setting of the study area shows that, from top to bottom, the following units are exposed in the field (data from the Italian Geological Cartography, CARG):

- The Sele Vally tectonic units in particolar with the Mt. San Arcangelo formation (**FMS**), havana and gray marly limestones, silty clay marl; marine basin environment, Upper Paleog
- The Carbonate tectonic Units in particolar with the:
  - Dolomitic limestone and limestones formation (**CLU**) platform environment, Low Giura
  - Limestone with gastropods formation (**CRQ**), platform environment, Low Cret
  - Bio lithoclastic limestones with rudists formation (**CBI**); upper slope environment- Low Cret
  - Saccharoid Brown dolomites with megalodon, and light stratified dolomites with fenestrae (**DBS**); platfrom environment- Upper Cret.

The main mineralization focus of this study consists of comb-veins (C-veins) and slip parallel (SP-veins), which are respectively oriented ca. perpendicular and parallel to the main master fault planes (Appendices, Fig.2.1). The nomenclature adopted for the comb veins was first proposed by Hancock and Barka (1987) and Stewart and Hancock (1990), who initially interpreted them as tension cracks reflecting down-dip displacement of the footwall blocks, and co-seismic stress release localizing deep overpressured fluids ingress and flow (Smeraglia et al., 2018 and reference therein).

The mineralization that cutting Apennine carbonate platform sequences and employed for this study (18 samples, show in Table 2.1 and Fig. 2.2), were collected from an area that was approximately 40 km^2-wide, from 12 medium-high angle fault segments-oriented NE-SW and WNW-ESE within the hydrothermal system of Contursi Terme ($T \leq 47$ °C). There, four main sites were chosen (Fig. 2.2): (1) Vallone Raio and Monte Castello faults (MC3 and VRD2, VRD02 samples respectively); (2) Colliano and Monte Carpineta fault sites (CVR, CR3, CVR4, CP2 and MCPTA samples respectively); (3) Senerchia sities (SEN 2.1 and SEN 2.1.1 samples); (4) Contursi hydrothermal basin (T.CAP, PR1W3, TUF 1, TUF1.1, PR4N20, PZZ1 samples). The calcite veins crosscut Lower Jurassic limestones, Upper Cretaceous dolomitic limestones, or Upper Paleogene marly limestones. Only the TUF. 1.1 calcite vein sample was not sampled near fault plane, but rather in a sinkhole structure with associated gas emissions.

Tab.2.1. *Description of the samples studied: sample identification, typology (HR= host rock; FR= fault rock, comb and parallel vein), geographical coordinates and lithology.*

N°	ID Samples	Location	Tipology	Latitude (N)	Longitude (E)	Lithology (CARG)
1	**MC3_V1**	Monte Castello (Contursi Terme)	Blocky calcite Comb-vein	40°41'24.37"N	15°17'55.70" E	CBI (Carbonate tectonic Unit)
2	**MC3_V2**	Monte Castello (Contursi Terme)	Fibrous calcite Comb-vein	40°41'24.37"N	15°17'55.70" E	CBI (Carbonate tectonic Unit)
3	**MC3_H**	Monte Castello (Contursi Terme)	Host rock	40°41'24.37"N	15°17'55.70" E	CBI (Carbonate tectonic Unit)
4	**VRD02**	Vallone Raio (Contursi Terme)	Blocky calcite comb and parallel veins	40°41'08.96"N	15°18'35.48"E	CBI (Carbonate tectonic Unit)
5	**VRD1.1**	Vallone Raio (Contursi Terme)	Blocky calcite comb and parallel veins	40°41'08.96"N	15°18'35.48"E	CBI (Carbonate tectonic Unit)
6	**VRD2**	Vallone Raio (Contursi Terme)	Blocky calcite comb and parallel veins	40°41'08.96"N	15°18'35.48"E	CBI (Carbonate tectonic Unit)
7	**CVRH**	Colliano Villa Rosa	Host rock	40°43'39.35"N	15°18'28.15" E	CBI (Carbonate tectonic Unit)
8	**CVR**	Colliano Villa Rosa	Blocky calcite vein	40°43'39.35"N	15°18'28.15" E	CBI (Carbonate tectonic Unit)
9	**CVRN30**	Colliano Villa Rosa	Blocky calcite vein	40°43'39.35"N	15°18'28.15" E	CBI (Carbonate tectonic Unit)
10	**CVR3**	Colliano Villa Rosa	Blocky calcite vein	40°43'44.53"N	15°18'28.15" E	CBI (Carbonate tectonic Unit)
11	**CVR4**	Colliano Villa Rosa	Blocky calcite vein	40°43'44.53"N	15°18'13.63" E	CBI (Carbonate tectonic Unit)
12	**CP2H**	Colliano	Host rock	40°43'33.00"N	15°17'25.18" E	CBI (Carbonate tectonic)
13	**CP2**	Colliano	Blocky calcite comb vein	40°43'33.00"N	15°17'25.18" E	CBI (Carbonate tectonic)
14	**MCPTA**	Monte Carpineta (Colliano)	Blocky calcite comb-vein	40°43'24.93"N	15°19'01.95" E	CBI (Carbonate tectonic)
15	**SEN 2.1**	Senerchia	Blocky calcite comb and slip veins	40°44'28.05"N	15°12'01.50" E	CLU (Carbonate tectonic unit)
16	**SEN 2.1.1**	Senerchia	Blocky calcite comb-vein	40°44'28.05"N	15°12'01.50" E	CLU (Carbonate tectonic unit)

17	**T.CAPH**	Terme Capasso (Contursi Terme)	Host rock	40°41'24.05"N	15°15'04.73"E	FMS (Sele Valley tectonic unit- Mt. San Arcangelo formation)
18	**T.CAP**	Terme Capasso (Contursi Terme)	Blocky calcite vein	40°41'24.05"N	15°15'04.73"E	FMS (Sele Valley tectonic unit- Mt. San Arcangelo formation)
19	**PR1W3**	Monte Pruno (Contursi Terme)	Blocky calcite vein	40°40'51.03"N	15°15'21.49" E	CLU (Carbonate tectonic unit)
20	**PR1E**	Monte Pruno (Contursi Terme)	Blocky calcite parallel vein	40°40'51.03"N	15°15'21.49" E	CLU (Carbonate tectonic unit)
21	**TUF_HR**	Terme Tufaro (Contursi Terme)	Host rock	40°40'23.33"N	15°14'56.21"E	FMS **(**Sele Valley tectonic unit- Mt. San Arcangelo formation)
22	**TUF 1**	Terme Tufaro (Contursi Terme)	Blocky calcite vein	40°40'23.33"N	15°14'56.21"E	FMS **(**Sele Valley tectonic unit- Mt. San Arcangelo formation)
23	**TUF 1.1**	Terme Tufaro (Contursi Terme)	Blocky calcite vein	40°40'23.33"N	15°14'56.21"E	FMS **(**Sele Valley tectonic unit- Mt. San Arcangelo formation)
24	**TUF_TRV1**	Terme Tufaro (Contursi Terme)	Travertine	40°40'23.33"N	15°14'56.21"E	FMS **(**Sele Valley tectonic unit- Mt. San Arcangelo formation)
25	**TUF_TRV2**	Terme Tufaro (Contursi Terme)	Travertine	40°40'23.33"N	15°14'56.21"E	FMS **(**Sele Valley tectonic unit- Mt. San Arcangelo formation)
26	**TUF_TRV3**	Terme Tufaro (Contursi Terme)	Travertine	40°40'23.33"N	15°14'56.21"E	FMS **(**Sele Valley tectonic unit- Mt. San Arcangelo formation)
27	**TUF_TRV4**	Terme Tufaro (Contursi Terme)	Travertine	40°40'23.33"N	15°14'56.21"E	FMS **(**Sele Valley tectonic unit- Mt. San Arcangelo formation)
28	**PR4N20H**	Monte Pruno (Contursi Terme)	Host rock	40°40'50.87"N	15°16'43.48"E	CRQ (Carbonate tectonic unit)
29	**PR4N120**	Monte Pruno (Contursi Terme)	Blocky calcite vein	40°40'50.87"N	15°16'43.48"E	CRQ (Carbonate tectonic unit)
30	**PR4N20**	Monte Pruno (Contursi Terme)	Blocky calcite vein	40°40'50.87"N	15°16'43.48"E	CRQ (Carbonate tectonic unit)
31	**PZZ1**	Mt. Perrazze (Contursi Terme)	Blocky calcite comb vein	40°40'36.95"N	15°17"20.80"E	CLU (Carbonate tectonic unit)
32	**PZZ3_FR**	Mt. Perrazze (Contursi Terme)	Fault rock	40°40'36.95"N	15°17"20.80"E	CLU (Carbonate tectonic unit)

The sampled veins commonly include either whitish or greyish calcite crystals, with the latter ones probably associated with organic matter. Their cutting the Jurassic-Cretaceous limestone Platform environment, and havana and gray marly limestones, silty clay marl, marine basin environment. Their have widths range from a few millimeters up to about 1 – 1.5 cm. The most mineralization veins were studied were reported in Fig. 2.3.

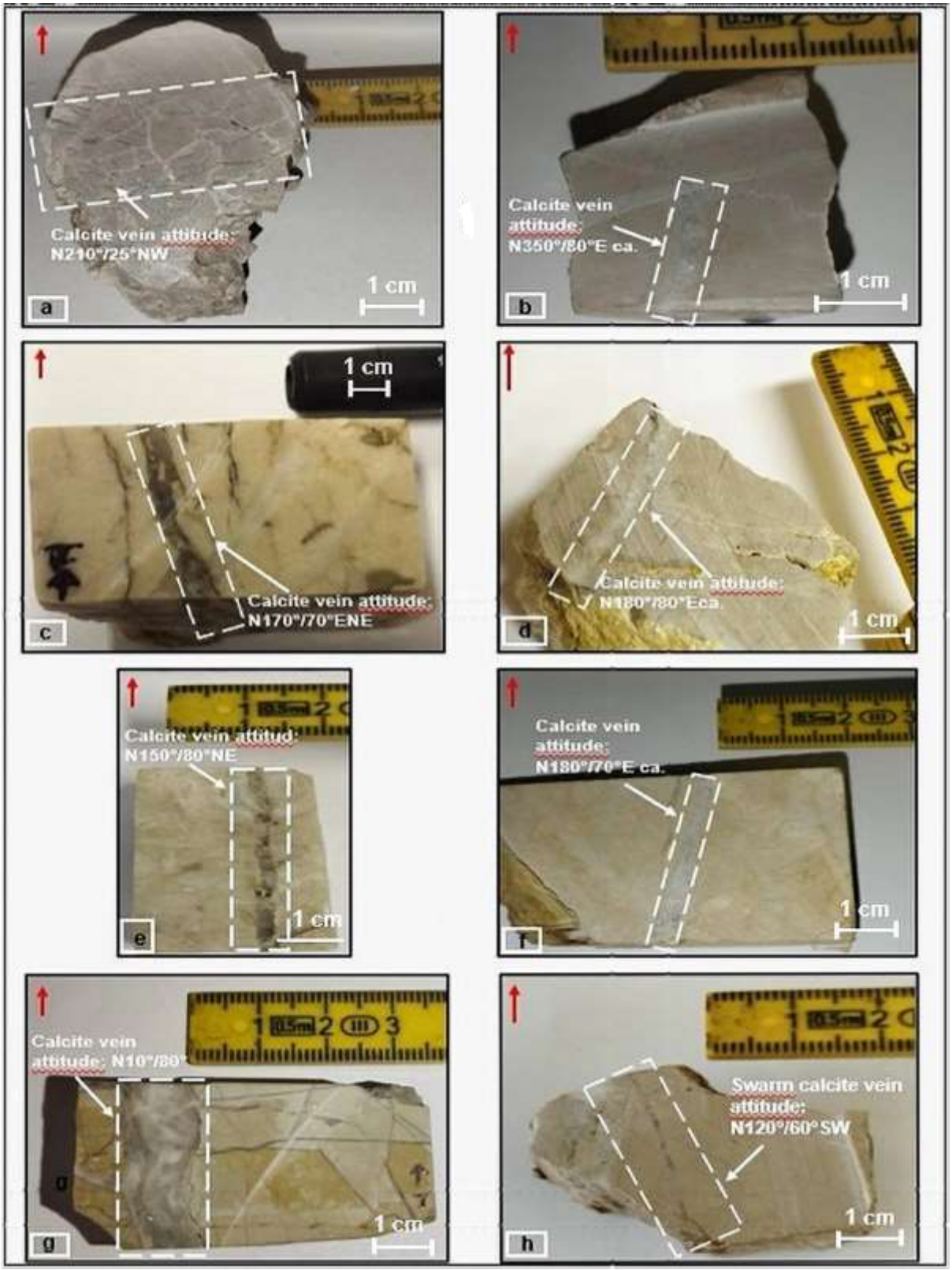
Calcite vein attitude:
N210°/25°NW
1 cm
a
Calcite vein
attitude:
N350°/80°E ca.
1 cm
b
1 cm
Calcite vein attitude:
N170°/70°ENE
c
Calcite vein attitude:
N180°/80°E ca.
1 cm
d
Calcite vein attitud
N150°/80°NE
1 cm
e
Calcite vein
attitude:
N180°/70°E ca.
1 cm
f
Calcite vein
attitude: N10°/80°
g
1 cm
g
Swarm calcite vein
attitude:
N120°/60°SW
1 cm
h

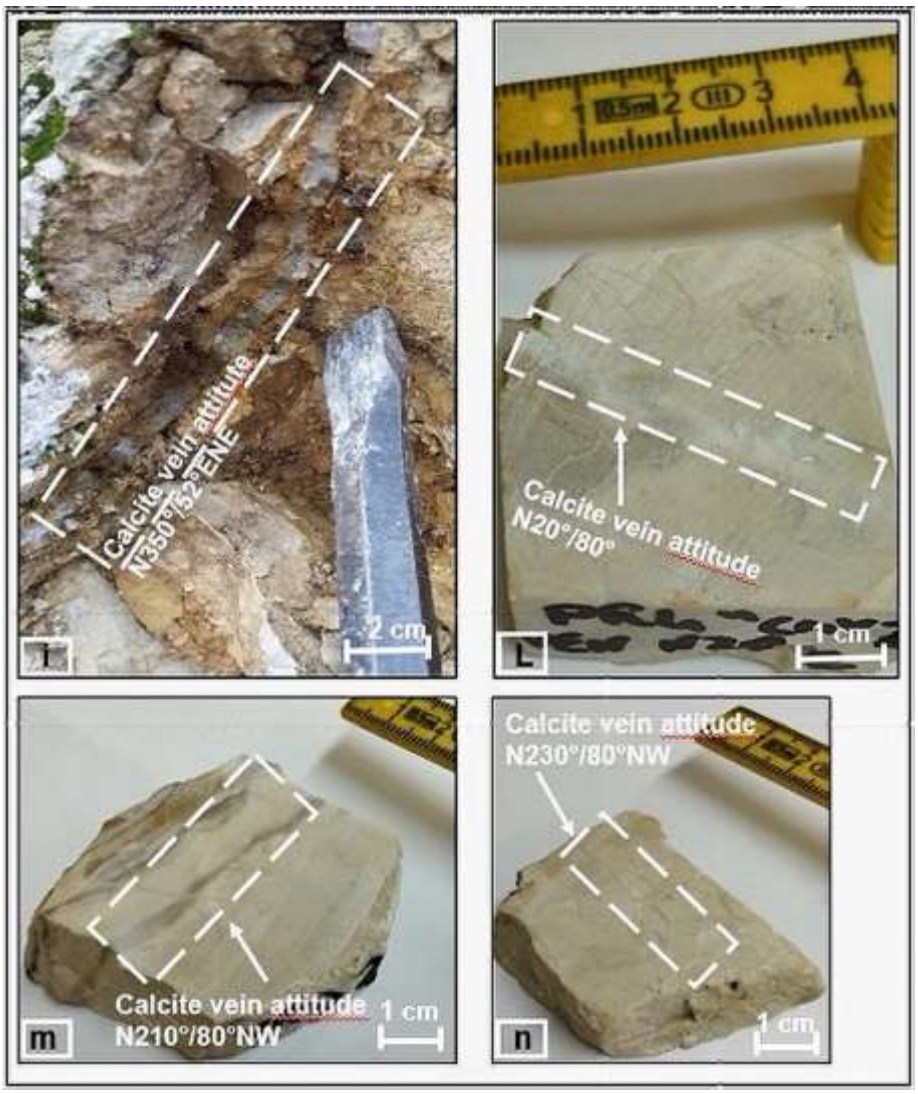

Fig.2.3 *Photomicrographs of most of the comb and slip parallel calcite veins samples used in this PhD thesis, divided into main four micro-areas:* ***(a)*** *SEN 2.1 sample by Senerchia area;* ***(b, c, m)*** *VRD02, MC3, VRD2 samples by V.ll.ne Raio and Mt. Castello fault, respectively;* ***(e, h, i, n)*** *MCPTA, CVR3, CVR, CP1 samples from Mt. Carpineta faults area and Colliano respectively;* ***(d, f, g, l)*** *PR1W3, T.CAP, TUF1.1, PR4N20 samples from Contursi thermal area.*

Chapter 3 – Geological setting of the Irpinia area (Southern Italy)

3.1. GEOLOGY AND TECTONICS

The structure of the southern Apennines is related with the Meso-Cenozoic tectonic processes that involved the African and European plates. The different tectonic phases of rifting, drifting, and shortening that occurred over time, lead the backbone of the Apennines to have a E-NE verging, duplexes geometries and out-of-sequence thrusting, mainly due to orogenic contraction that was active since upper Eocene-Oligocene up to late Pliocene.

The study area (Fig.2.2) is located in the western portion of the southern Apennines fold and thrust belt (Fig.3.1). This belt developed since Oligo-Miocene times due to the progressive collision between the African and European plates, and interactions with the intervening Adria-Apula plate (Patacca et al., 1990). Regional-scale thrusting took place by mean of both thin-skinned and thick-skinned tectonics (Shiner et al., 2004), forming a complex multi-duplex that now day trend approximately N150° direction, subparallel to the strike of main thrust faults (Patacca and Scandone, 2007). The tectono-stratigraphic units of the belt have been dissected by Plio-Quanternary high-angle faults associated with the aperture of the Tyrrhenian Sea and/or with the gravitational collapse of the contractional edifice (Vezzani et al., 2010). Extension currently occurs along the axial zone of the belt, whereas thrusting takes place along its frontal, peri-Adriatic sector (Fig. 3.1c). Focusing on the axial sector of the southern Apennines, its uplifting began during the Middle to Upper Pleistocene due to active extensional faults rooted at depth down to ca. 15 km, as suggested by surface and sub-surface geology, borehole breakout, and fault plane earthquakes. The greatest amount of stretching trends NE-SW direction, with a computed extension rate is ca. 3-5 mm/y (Ascione et al., 2013).

In the study area, the main tectono-stratigraphic units of the belt consist of a deep-seated carbonate of the Apennine Platform, and basinal rocks of the Lagonegro Basin (Patacca and Scandone 2007; Ciarcia et al., 2009). At regional scale, low angle thrust faults juxtapose the platform carbonates, at the hanging wall, against the Lagonegro units, at the footwall. The entire accretionary wedge overrides the buried Apulian Platform (Fig. 3.1a, b). The deformed Apulian carbonates currently host the largest hydrocarbon reserves of southern Europe, and form CO_2 geological traps generating overpressure reservoirs (Shiner et al., 2004). The origin of large earthquakes within this tectonic context is believed being associated with the presence of fluids within the crust that can reach overpressure conditions at up 15 km depths due to the low permeability of the rock formations that inhibit their circulation.

The study area is characterized by a high seismogenic potential (Slejko et al. 1998) and has been affected by background seismicity Mw < 4 (http://isnet-bulletin.fisica.unina.it/cgi-bin/isnet-even3ts/isnet.cgi) during the recent decades. The epicenter of last catastrophic earthquake in the region, which occurred in November 1980 (Mw 6.9, Bernard and Zollo, 1989) was located between 1 and 5 km from the Contursi hydrothermal basin. This area is characterized by the presence of seismogenic faults and by fluids with high pore pressures that are capable of generating aftershocks (Amoroso et al., 2017, and reference therein). Fault plane solutions show both normal

and oblique (trastensional) slip kinematics, confirming the dominant SW–NE extensional regime. The background low magnitude seismicity appears to be spread into a large volume, and the related stress field is closely linked with the major fault segments activated during the 1980 Irpinia earthquake. In addition, microseismicity seems to be controlled by high pore pressure of water-saturated Apulian carbonates within a fault-bounded crustal volume (D'Agostino et al., 2018; Picozzi et al., 2022). The presence of crustal fluids represents a fundamental issue to be considered in hazard studies, considering the strong relationship that emerged between seismicity and high-fluid pressure during the recent strong earthquakes in the Apennines (e.g., the Mw 6.0, 1997, Colfiorito earthquake and the Mw 6.3, 2009 L'Aquila earthquake) (Chiarabba et al., 2020; Chiodini et al., 2020).

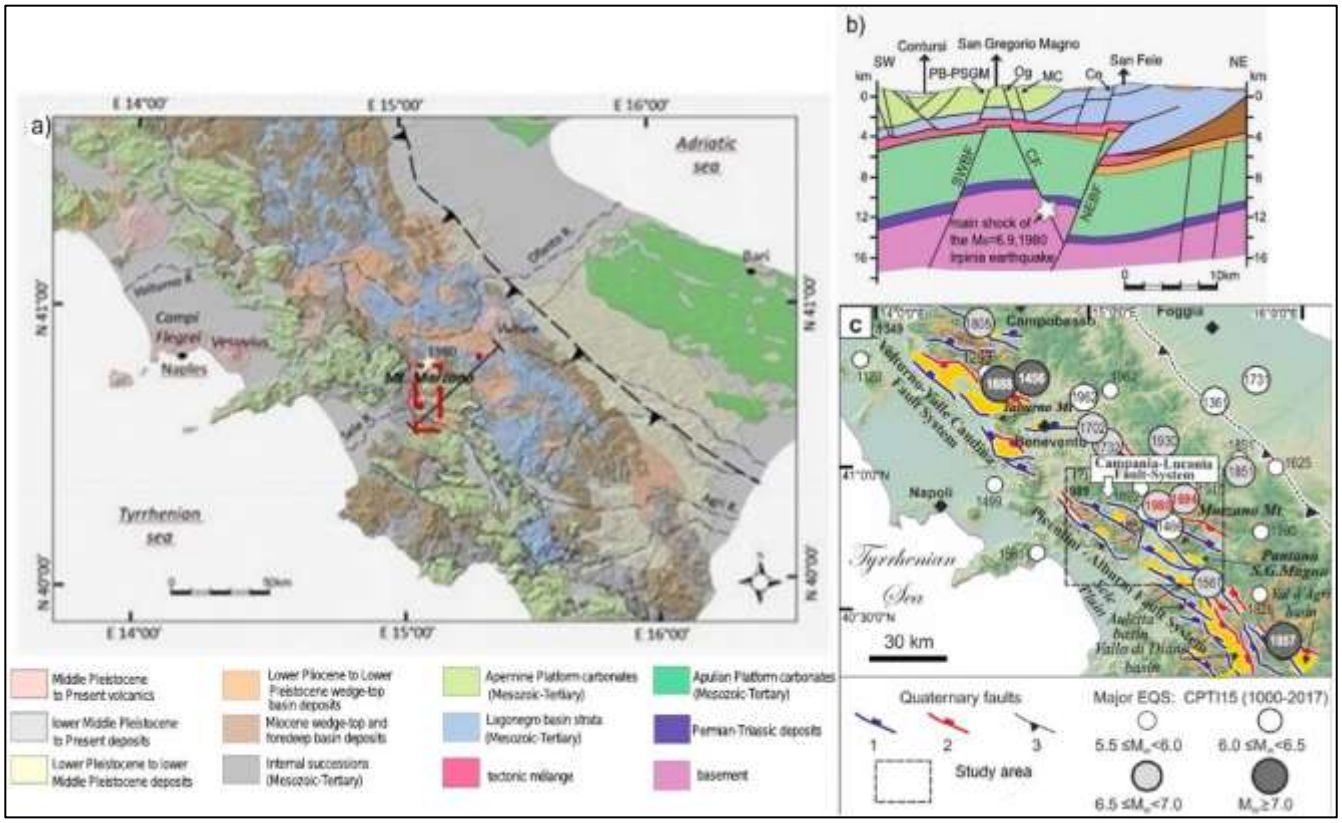

Fig. 3.1. *Tectonic setting of the 1980 Irpinia earthquake.* ***(a)*** *Geological sketch map of the southern Apennines; in red rectangle, area for this study (modified after Ascione et al., 2013).* ***(b)*** *Cross section [after Ascione et al., 2013]. Star shows hypocenter of the Ms 6.9, 1980 Irpinia earthquake; SWBF: SW Boundary Fault; CF: Central Fault; NEBF: NE Boundary Fault.* ***(c)*** *Active faults in Southern Italy with major historical and instrumental earthquakes from Parametric Catalogue of Italian Earthquakes, CPTI15 v2. Key: 1, east-dipping normal faults; 2, west-dipping normal faults; 3 thrust faults (modified after Bello et al., 2021).*

In the Irpinia area, tomographic images reveal two kinds of reservoirs (Impronta et al., 2014; Amoroso et al., 2017). A low-Vp/Vs dome-shaped body, about 20 km-long and 15 km-wide, which is located between 6 km and 11 km depth underneath the Forcuso Mt. located in the northern part of the Irpinia region of southern Italy. This geophysical evidence shows presence of pressurized CO_2-rich rock volumes below the Apulian platform carbonates which are due to by fluid-rich mantle melts intruded into the crust (Impronta et al., 2014; Amoroso et

al., 2017; Ascione et al., 2020). This pressurized volume well correlates with high heat flow values (100 – 215 mW/m^2) observed along the Forcuso Mt. antiform structure. Active faults in Irpinia region control the gas leakage from the crust, also influencing the leakage areas distribution at the surface. Furthermore, 30 km north to the study area, a very significant amount of non-volcanic deep CO_2-rich gas emission (~ 2000 T/d) principal expression is documented at the Mefite D'Ansanto gas emission site, which forms a high heat flow anomaly of the southern Apennines (up to about 215 mW/m^2; Doglioni et al., 1996). There, the $^3He/^4He$ ratio is up 2.84 Ra; this is a value similar to those the characterize the active volcanoes of the Campania region of Italy (Vesuvio and Campi Flegrei), ca. 70 km west to the study area. The aforementioned data therefore suggests that the active rule of lithospheric faults in trasfering fluids at regional scale and/or along with magmatic intrusions could transfer within the crust (e.g., Italiano et al., 2000; Caracausi and Paternoster, 2015; Buttitta et al., 2023).

In the central portion of the Irpinia area (e.g. approximately within the Marzano segment in which the 1980 earthquake nucleated), tomographic images show a high Vp/Vs broad region between 4 km and 6 km which is interpreted as fractured, fluid-saturated carbonates (Impronta et al., 2014; Amoroso et al., 2014). The physical modeling of 3D velocity images (Amoroso et al., 2017) lead to estimate a porosity of carbonates in the Marzano segment around 4% - 5%, and a fluid composition consisting of brine–CO_2 and/or CH_4 –CO_2. The occurrence of pressure changes in fluid-filled cracks within carbonates is considered one of the main trigger mechanisms of micro-earthquakes in the Irpinia region.

In particular, the studied ***Contursi hydrothermal basin*** is located along the Sele River Valley, whose structural setting was previously interpreted as consisting of a NS- trending graben (Coppola and Pescatore, 1989), where high-angle faults border the carbonate massifs (Mt. Marzano and Mt. Cervialto) and flanks the Neogene-Quaternary continental deposition topping the Mesozoic carbonate. This sector is thought as playing as an extensional transfer zone between the Marzano and Cervialto fault segments.

3.2. HYDROGEOLOGY

The southern Apennines is mainly characterized by Meso-Cenozoic carbonates that act as huge karst aquifers bounded by a low permeability deposit (i.e., aquitards and/or aquicludes), such as syn-orogenic siliciclastic marine deposits or Messinian evaporites (Celico et al., 2006). The upper Sele river valley is bordered to East and West by two carbonates mountain range: Mt. Marzano-Ogna and Picentini Mts, respectively (Fig. 3.2).

They constitute two main aquifers of the study area because of their large volume and high hydraulic conductivity enhanced by diffuse fracturing and intense karst processes (Celico and Civita, 1976; Wasowki et al., 2002). They fed several springs located along their fault boundaries, where aquicludes of turbidite deposits are in direct contact with carbonate rocks. The Picentini Mts. constitute a 600 km^2 wide large karst system and encompass four large mountain groups (Corniello et al., 2010), recognized as different hydrogeological basin. Among these basins, the

Mt. Polveracchio aquifer (Fig.3.2) is characterized by a complex geo-structural setting that affects groundwater flow-paths strictly constrained by tectonic discontinuities. Along the northern and north-easting margin, the hydrogeological limit consists of a fault between Acerno and Calabritto localities, where the main groundwater outlet is the Acquara-Ponticchio spring. Along the western margin, the boundary is represented by fault system separating Mt. Accellica from Mt. Polvercchio. Further south, the Polveracchio basin is buffered by impermeable lithotypes of the Lagonegro units (Fig.3.2). Finally, along the eastern margin, in the upper Sele river, the boundary consists of a tectonic thrusting front.

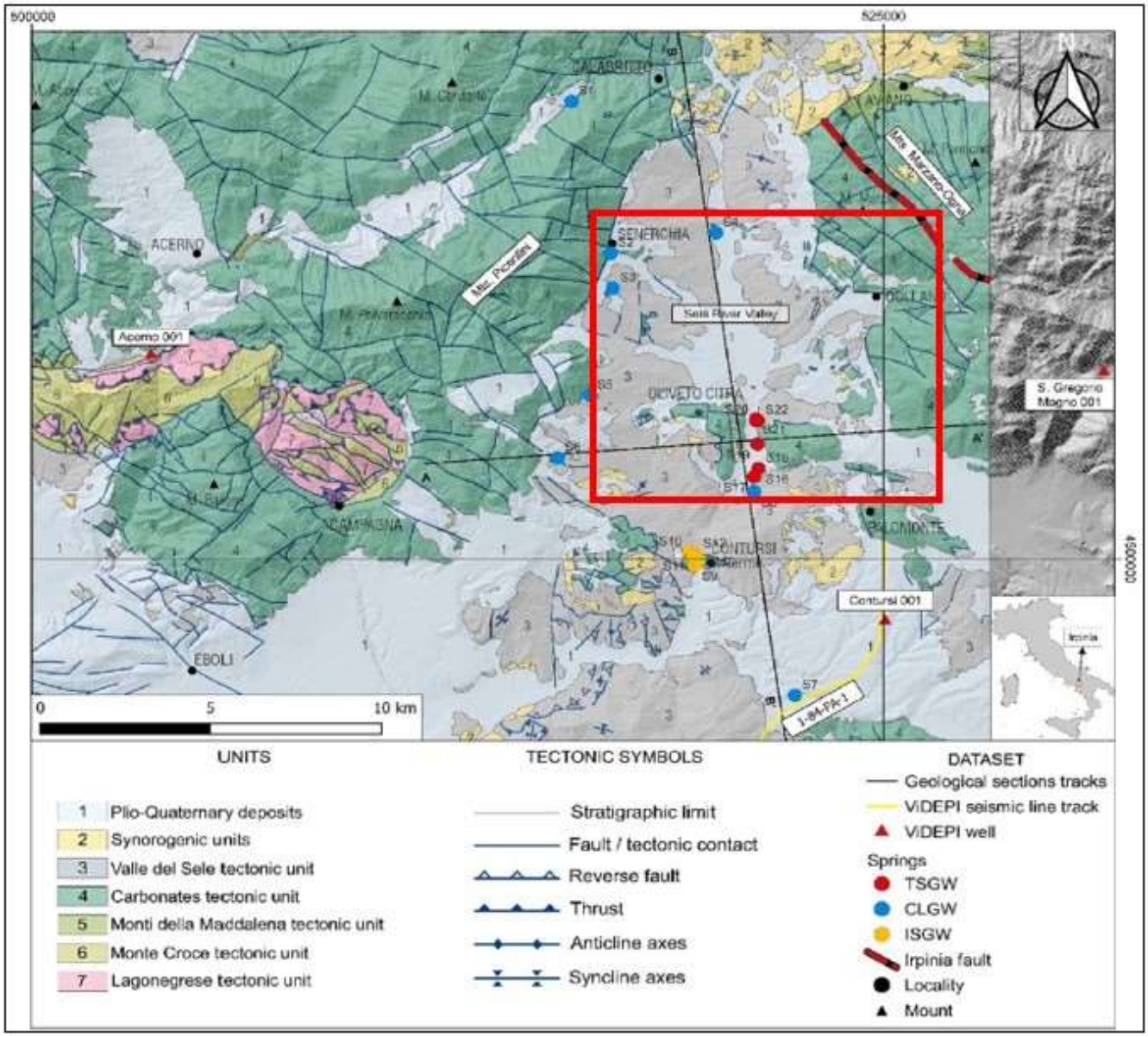

Fig.3.2. *Location of the hydrogeochemical study composition of groundwaters in Upper Sele river Valley (Gori et al., 2023). In red rectangle are show the study area.*

3.2.1 The chemical composition of groundwater in Contursi Hydrothermal basin

In a recent paper proposed by Gori et al. (2023), the authors through a multidisciplinary approach, combining hydrogeochemistry to geo-structural setting and isotopic study, propose an interpretative model of groundwater flow path for the Contursi area, where deep-seated tectonic discontinuities play a significant role for the upwelling of saline deep thermal fluids in shallow aquifers. The study area is characterized by groundwater resources divided in three main groups, according to the Electrical Conductivity (EC) and Temperature (T) value (Fig.3.3):

- *A first group*, represented by a Cold and Low salinity groundwaters (CLGW) with a Ca(Mg)-HCO_3 composition. These waters have the lowest EC (< 700 µS/cm) and T values (from 7.8 to 14.3 °C). The pH value is alkaline between 7,2 and 8,4.
- *A second groups*, with an Intermediate Salinity Groundwater (ISGW) show a T value between 13,8 and 18,5 °C, EC value from 1090 to 1981 µS/cm. The pH value is slightly acid (from 6,0 to 6,8), ISGW belongs to Ca-mg-HCO3 hydrofacies like CLGW.
- *A third group* of Thermal and Salinity Groundwater (TSGW); in details this group is a brackish-type water type, according to the classification of Drever (1997), having EC value from 2560 to 6470 µS/cm.

The latter are thermal with T values between 25 and 47 °C, slightly acid (pH values from 6,2 to 6,4). They are characterized by a Na-HCO_3-Cl composition and show a marked enrichment in sulphate respect to other groups. These waters show also a bubbling gas phase and have high dissolved CO_2 value. Among minor and trace elements (F, Li, B, Rb, Sr, Cs, SiO_2 and Ba), TSGW show the highest concentrations up to three orders of magnitude higher than CLGW and ISGW. The Langelier-Ludwing diagrams (Fig.3.4) by Gori et al. (2023), clarifies that T and EC increase (Fig. 3.3). This is related to a gradual enrichment of the Cl-SO_4 and Na contents, starting from Ca(Mg)-HCO_3 composition of could samples (CLGW type) up to Na-HCO_3-Cl composition of thermal samples (TSGW type). The separation between CLGW and TSGW groups is well-marked, while most springs of ISGW groups show an intermediate composition, suggesting the presence of mixing processes between the cold end-member and the thermal one.

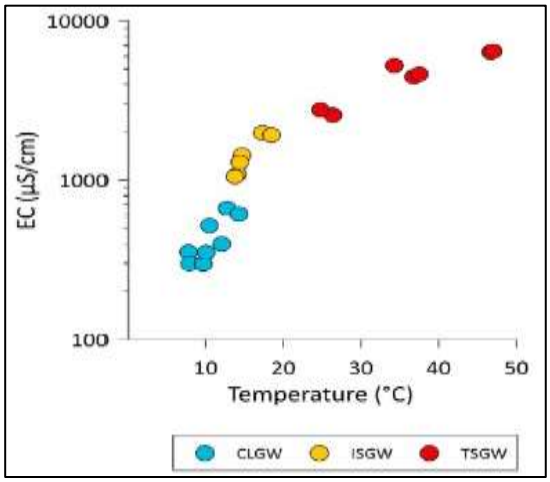

Fig.3.3. *Electrical conductivity (µS/cm) vs Temperature (°C). Three groups of groundwaters (i.e. CLGW, ISGW and TSGW) are identified and displayed with different colors (Gori et al., 2023).*

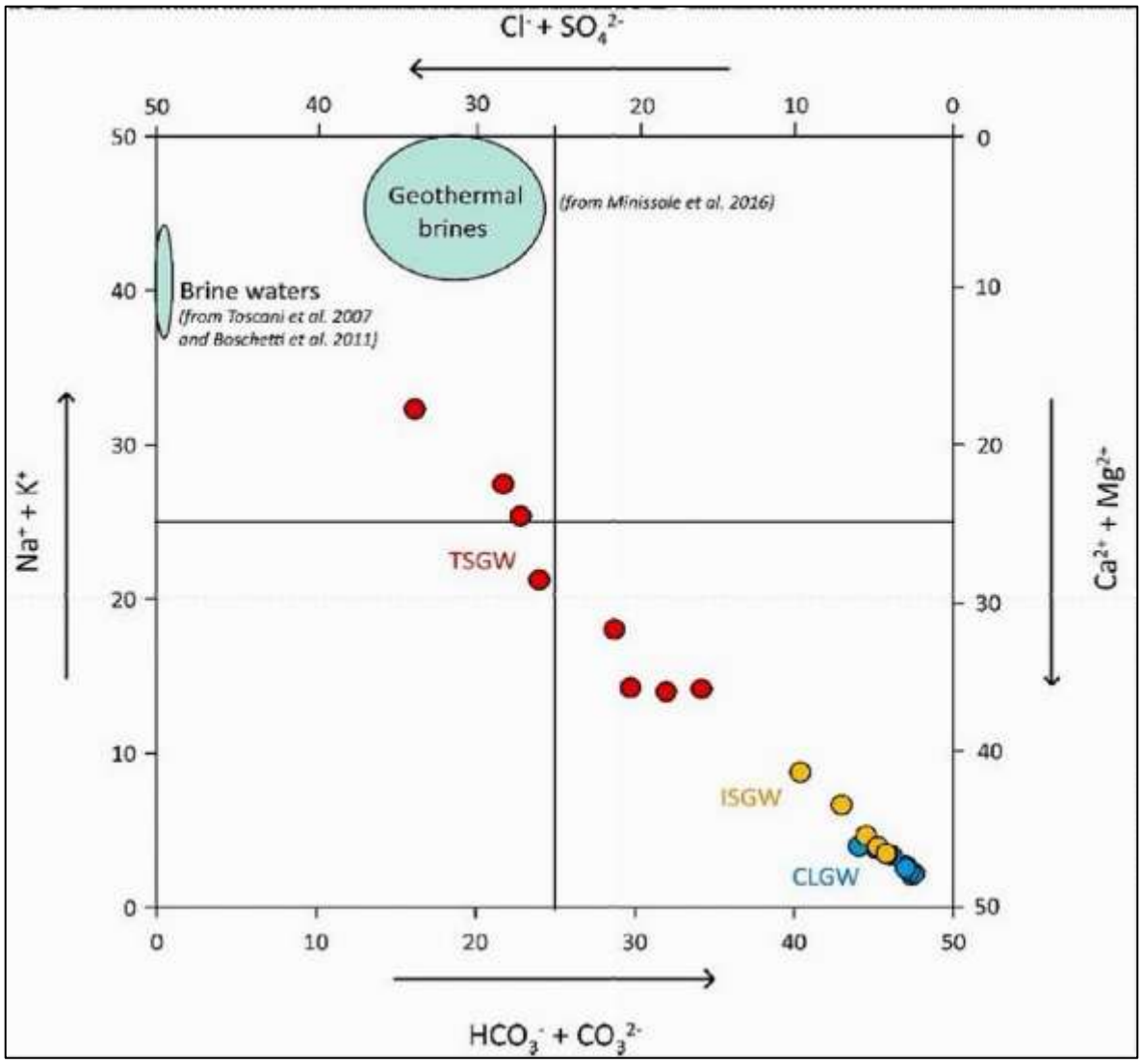

Fig.3.4. *Langelier-Ludwig diagram for groundwater samples from the Sele river valley. Most of samples are enriched in bicarbonate and calcium-magnesium ions (Ca-Mg-HCO3 hydrofacies). Only mineralized springs of the Contursi area are included in the sodium-chloride waters domain (Na-Cl hydrofacies). In detail, Cold Low salinity Groundwater (CLGW), Intermediate Salinity Groundwater (ISGW), and Thermal Saline Groundwater (TSGW) are displayed with cyan, yellow, and red circles, respectively; Literature data of brine waters and geothermal brines are also displayed (Toscani et al., 2007; Boschetti et al., 2011; Minissale et al., 2016); by Gori et al. (2023).*

The mixing processes between cold end-member and thermal one is also well represented by Na-Cl diagrams (Fig.3.5, Gori et al., 2023). All investigated waters along the Na/Cl ratio ~ 1, with TSGW having higher values than ISGW and CLGW. For the latter ones, the Na/Cl ratio is linked to seawater spray while for thermal waters (TSGW), can be linked to deep fluids uprising produced by halite dissolution from evaporitic layers.

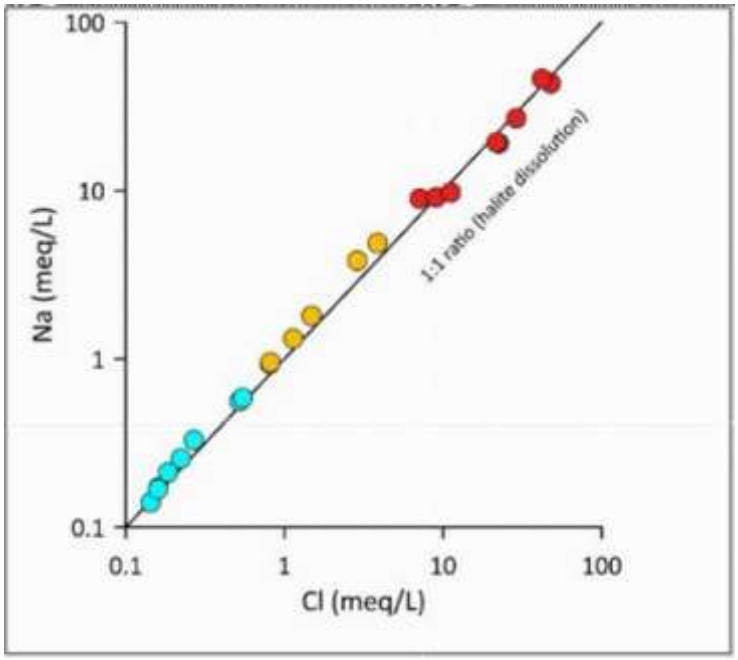

Fig. 3.5. *Na-Cl diagram. All investigated waters align along the Na/Cl ratio ~1 with TSGW having higher values than ISGW and CLGW (Gori et al.,2023).*

Finally, from hydrogeochemical and isotopic data (Gori et al., 2023), indicate the existence of more complex and regional groundwater hydrodynamics for ISGW and TSGW, which are characterized by longer and deeper flow paths emerging in the inner zone of Sele rive valley. A local flow system with a shorter residence time of water is supposed for the CLGW shallow carbonate groundwater mostly emerging at the boundary of carbonate aquifers. Tectonic discontinuities (e.g. deep-seated faults) play a crucial role in the circulation, acting as pathways for the upward migration of deep contributions to reach the shallow regional aquifers that are totally recharges by meteoric infiltration. These results are in line with a recent geophysical study carried out in this sector of Apennine that detected deep-seated fluid accumulation (brine and or CO_2).

3.3 PROCESSES OF GAS-WATER-ROCK INTERACTION OF CRUSTAL FLUIDS

A recent study conducted by Buttitta et al. (2023) in Contursi hydrothermal basin have investigated the processes of gas-water-rock interaction of crustal fluids. The authors confirm a regional degassing of mantle-derived He, using isotopic geochemistry and the carbon-helium system in free and dissolved volatiles in water and the interplay between mantle/magmatic and crustal fluids (Fig. 3.6).

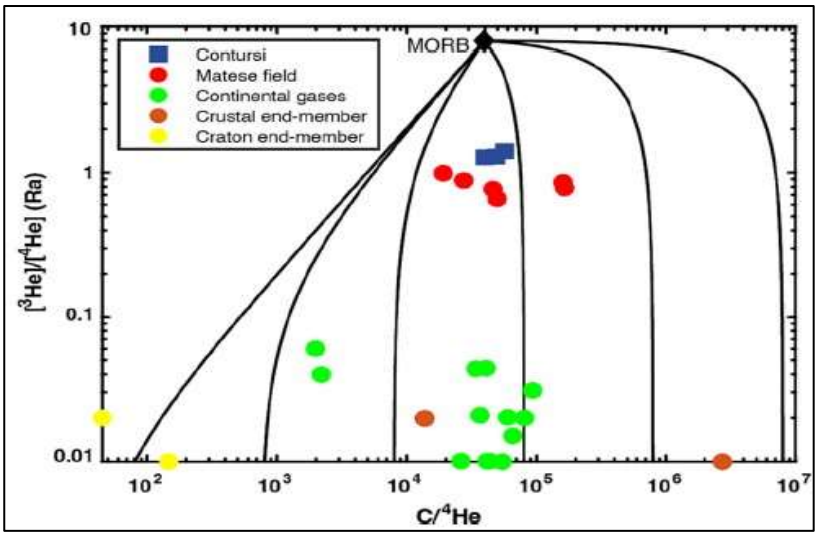

Fig. 3.6. *Binary mixing plot between Mantle ($^3He/^4He$=8 Ra, $CO_2/^4He$=3.94·104, Marty et al., 2020) and various crustal end-members ($CO_2/^4He$ = 80–8·10^6). The additional data are from INGV internal database. By Buttitta et al. (2023).*

Furthermore, the authors establish as the variability of the C/^{4}He elemental ratio, despite the overall steady ^{3}He/^{4}He ratio in the fluids, can be attributed to the different geochemical behavior of He and CO_2, suggesting the occurrence of secondary processes such as CO_2 loss (degassing/ calcite precipitation) and the addition of crustal CO_2 and ^{4}He. Gas-water interaction occurring in the dry reservoirs at depths between 7 and 8.6 km can modify the isotopic signature of CO_2 stored into the deep dolomitic reservoirs, potentially hindering its original carbon isotopic signature, Figure 3.7. In fact, the final isotopic signature of the fluids typical of the studied area (e. g CO_2) is due with mixing of cold waters and secondary gas-water interaction processes, such as precipitation and degassing.

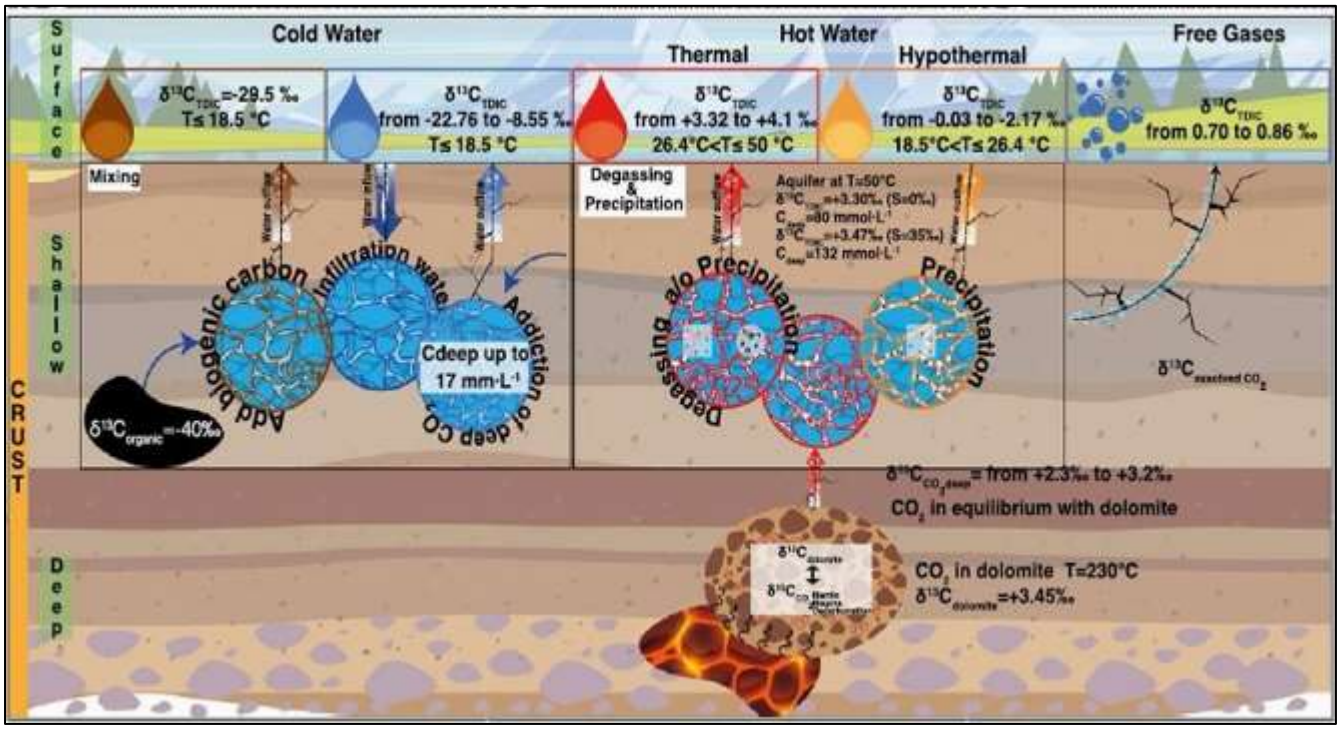

Fig. 3.7. *A general model for processes of gas-water-rock interaction of actually crustal fluids present in the Contursi hydrothermal basin by Buttitta et al. (2023).*

Chapter 4 – Results

This chapter shows (i) the main structural and microstructural results of the mineralization veins along seismogenic fault systems (fig. 2.2b, 2.3 and table 2.1); (ii) geochemical and isotopic results of faults-related mineralization veins (iii) Fluid inclusions (FIs) with petrographic, noble gases and micro-thermometric data.

4.1. STRUCTURAL AND MICROSTRUCTURAL ANALYSIS OF CALCITE VEINS

This sub-chapter show the main structural results of the field structural analysis and sampling of faults-related calcite veins. In addition, the texture and cross-cutting relationships of the mineralization veins, by optical microscope analysis of the four micro-areas identified (Fig. 2.2).

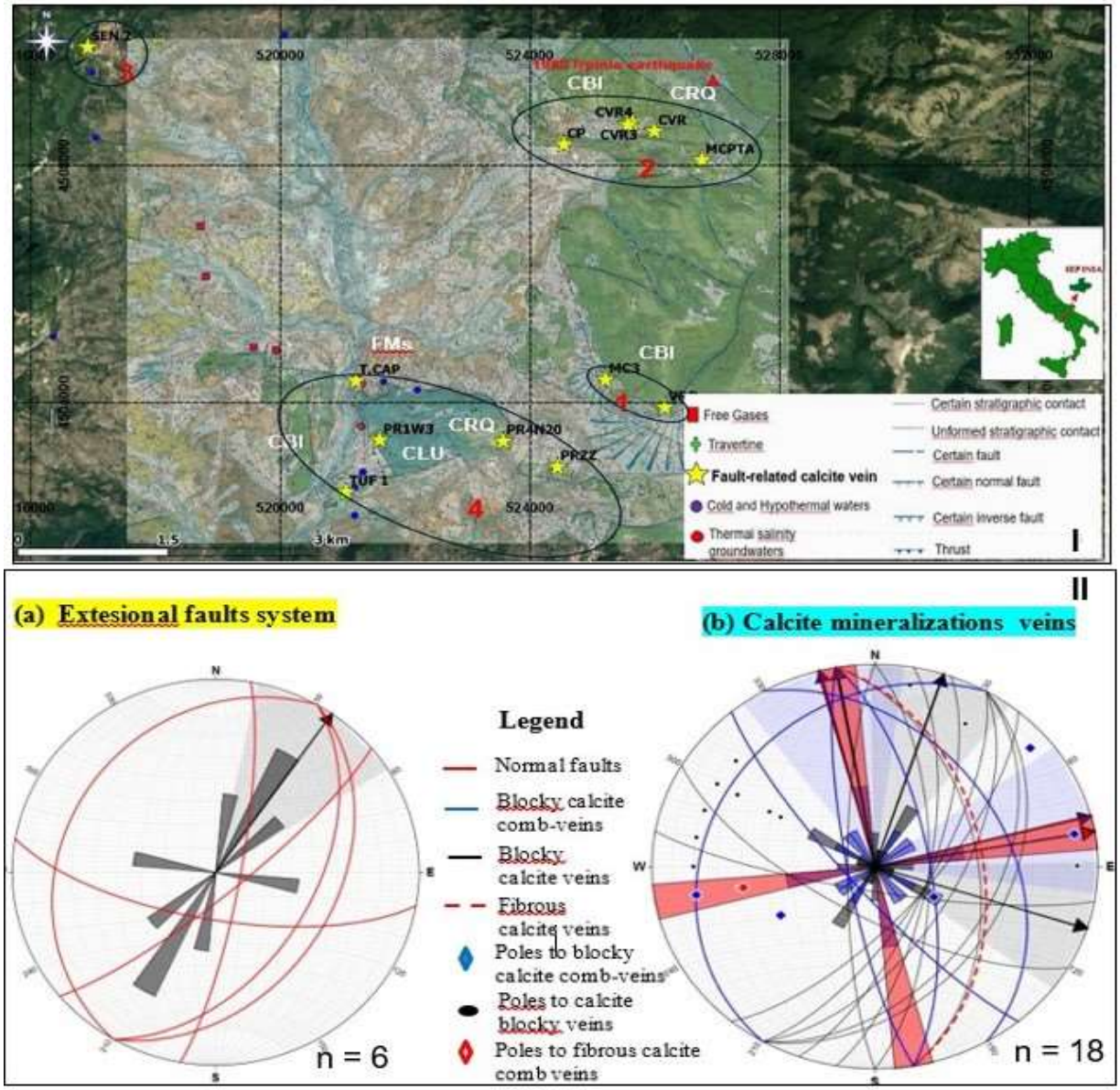

Fig.4.1. ***(I)*** *Localization of studied fault-related calcite veins samples.* ***(II)*** *Stereo-plot of structural analyses in the Irpinia area field.* ***(a)*** *Stereo plot of main extensional fault systems presents of the study area;* ***(b)*** *Stereo-plot of the structural analyses of calcite mineralization veins sampled in the Irpinia area. With arrow symbolism the main strike direction of fault and calcite veins.*

The 18 samples (Table 2.1 and Fig. 2.2) of calcite veins employed for this study crosscut the outcropping Apennine platform carbonates were collected from an area that was approximately 40 km^2-wide. Samples derive from 12 medium-high angle faults roughly striking either NE-SW or WNW-ESE and exposed within the hydrothermal system of Contursi Terme (Fig. 4.1 IIa). The sampled calcite veins roughly strike either NNW-SSE or ENE-WSW (Fig. 4.1 IIb). Independently of host-rock lithology and fault-strike directions, most of the studied calcite veins included blocky crystals. This texture is commonly associated with precipitation in phreatic conditions, and it can occur due to sealing of co-seismic fractures associated with transient of fluid overpressure. In two cases, as will be seen later, the calcite vein shows fibrous texture.

4.1.1 Structural Analysis of calcite veins

In this section the main structural aspects of most of the sites and fault zones studied are described.

Along the ***Monte Castello fault*** (area 1, Fig. 4.2), at a sub-vertical outcrop trending along the W-E direction and exposing Upper Cretaceous a bio-lithoclastic limestone with rudists with a bedding attitude of N240°/20°N. The limestone rock was displaced by a small-scale fault with an attitude N30E/40°NW, and crosscut by a cleavage N270E/30°S. Furthermore, high-angle veins with an attitude of N170E/70°ENE (MC3 sample) crosscut the hanging wall fault block (Fig. 4.2).

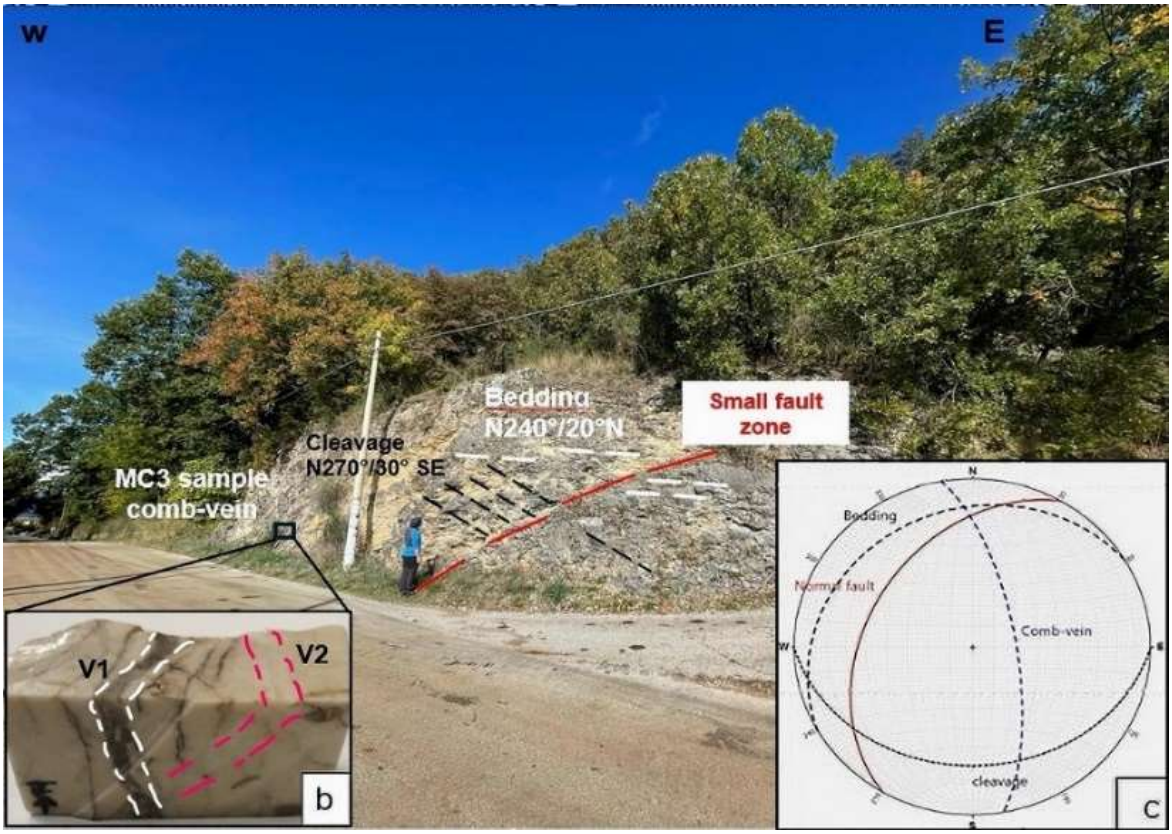

Fig 4.2 *Mt. Castello outcrop-oriented W-E with the presence of a small normal fault, low angle bedding and cleavage.* ***(b)*** *MC3 sample blocky calcite comb-veins a high angle (V1) with a strike N170°/70° ENE and V2 fibrous calcite vein.* ***(c)*** *stereo-plot with normal fault (in red), comb-vein (long blue dashes) in black solid line the bedding and cleavage presence.*

Along the ***Vallone Raio fault*** (V.ne Raio, area 1; Fig. 4.3a), the is outcrop oriented approx. SW-NE, and show a bedding attitude of the carbonates ca. N270°/40°N. Additionally, the outcrop displays joints oriented approximately N270°/30°SE. These aforementioned elements are displaced by a fault zone with an attitude N210°/50°E. The fault zone contains protocataclasite, which is 1-5 cm thick and hosts a fragmented rock of about one meter. There, low angle veins (comb-veins) show mutual crosscutting relations with the high-angle veins N210°/80° (VRD1 and VRD2 samples in Fig. 4.3b, c).

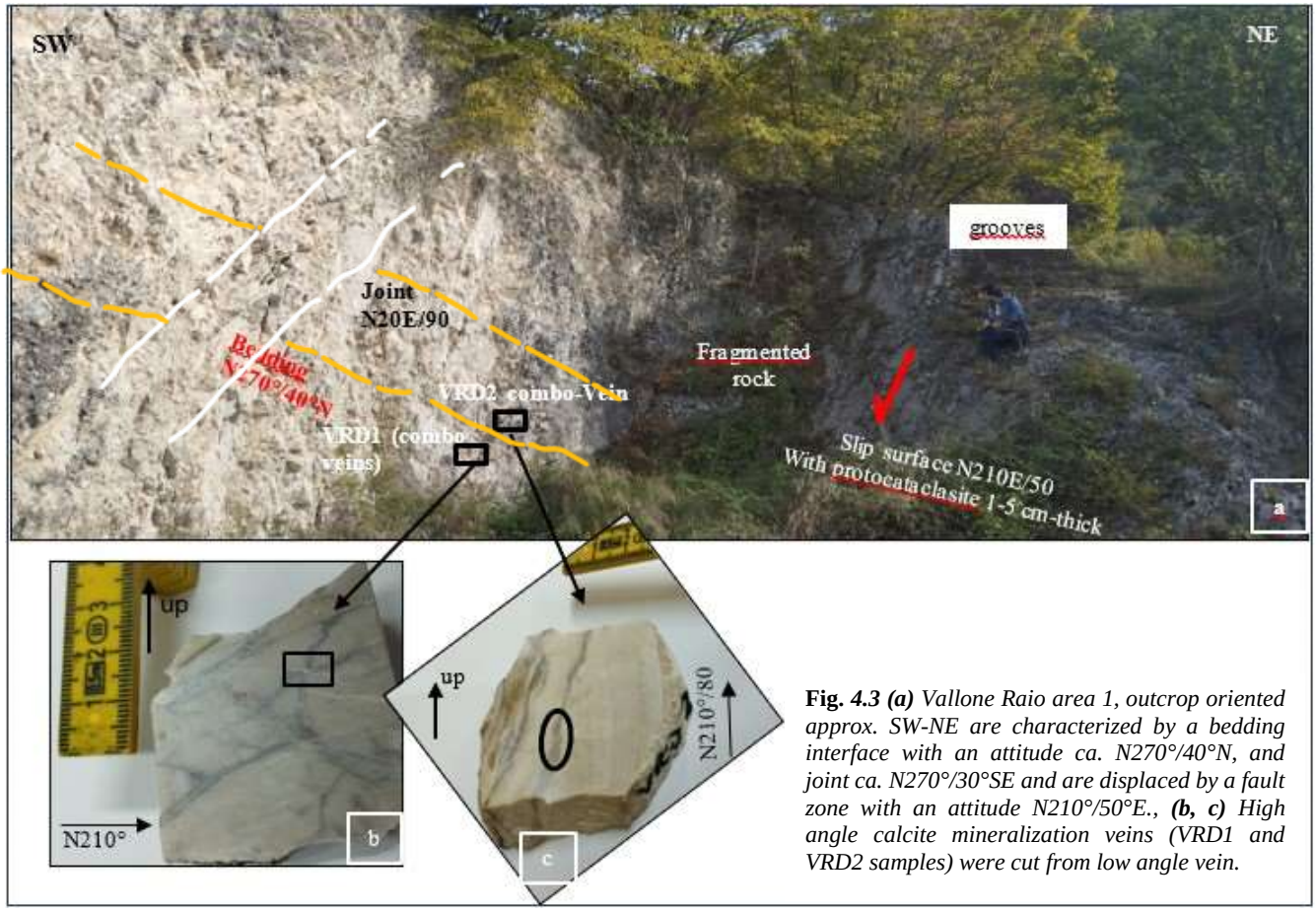

Fig. *4.3 (a)* *Vallone Raio area 1, outcrop oriented approx. SW-NE are characterized by a bedding interface with an attitude ca. N270°/40°N, and joint ca. N270°/30°SE and are displaced by a fault zone with an attitude N210°/50°E.,* ***(b, c)*** *High angle calcite mineralization veins (VRD1 and VRD2 samples) were cut from low angle vein.*

In Vallone Raio, area 1, (Fig. 4.4a), moreover the carbonate outcrop ends with a downward angular unconformity. Bedding is observed with an attitude N275°/20°N. Alongside two sets joints respectively oriented N110°/70 and N350°/90° are documented. Furthermore, high-angle calcite veins with attitude N320°/90° and N350°/90 (VRD0_1 and VRD0_2 samples shown in Fig. 4.4 b, c) are present. These latter veins are intersecting an oblique stylolite.

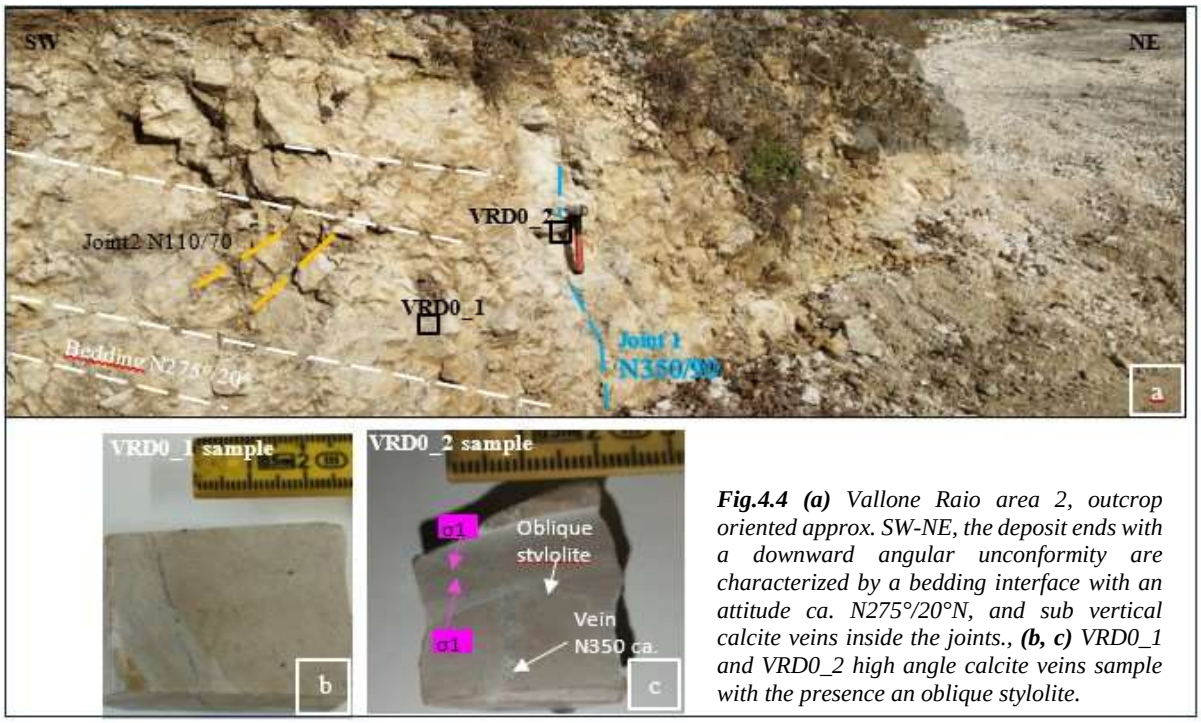

Fig.4.4 (a) *Vallone Raio area 2, outcrop oriented approx. SW-NE, the deposit ends with a downward angular unconformity are characterized by a bedding interface with an attitude ca. N275°/20°N, and sub vertical calcite veins inside the joints.,* ***(b, c)*** *VRD0_1 and VRD0_2 high angle calcite veins sample with the presence an oblique stylolite.*

At the colliano area, area 2, three calcite veins are studied: CVR, CVR3 and CP2 samples. The CVR3 sample (Fig.4.5), was collected along the sub vertical outcrop was oriented approximately W-E direction located along the road near Villa Rosa house. There, the Upper Cretaceous bio-lithoclastic limestones with a bedding attitude N30°/15° are crosscut by joints and bed-parallel veins. Furthermore, a swarm of stockwork calcite veins N120°/60°, is exposed at surface, which is consistent with past episodes of fluid overpressures possibly related to co-seismic faulting. The sample includes a swarm of stockwork veins and presents a massive blocky calcite texture.

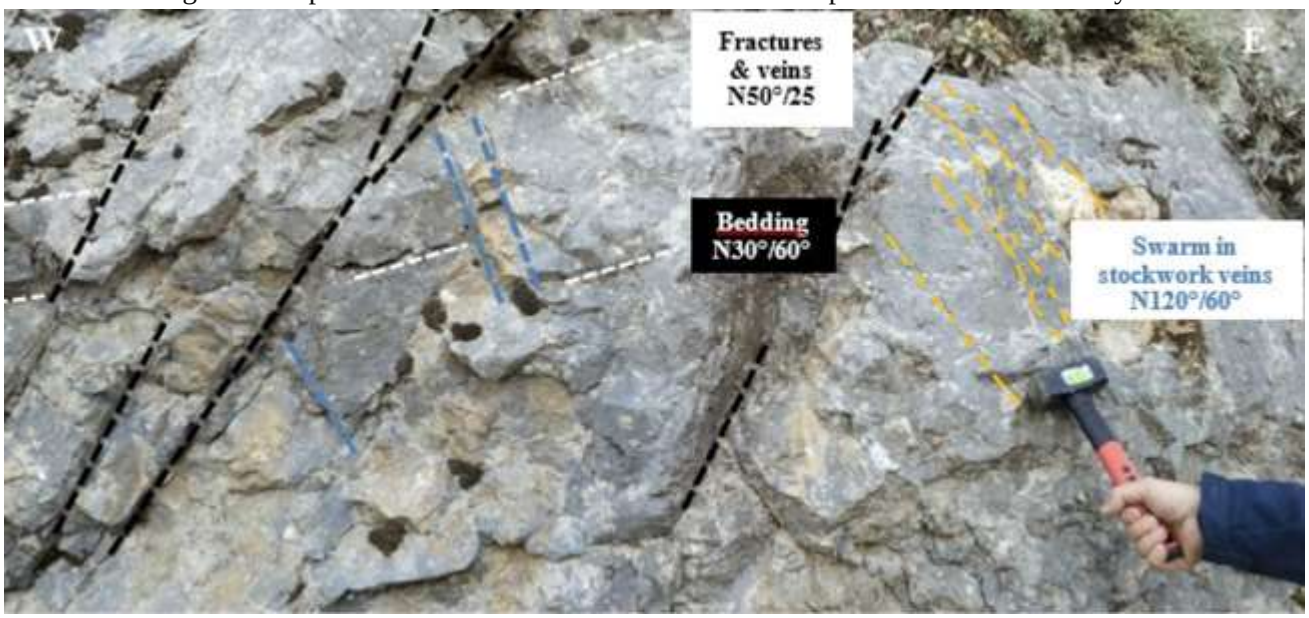

Fig.4.5. *CVR3 outcrop oriented ca. W-E associated a fractures and swarm stockwork mineralization veins.*

The CP2 sample (Fig. 4.6), was collected at the Colliano village along a W-E striking sub-vertical outcrop. There, a normal fault N230°/88°E with pitch N120°crosscut the limestone host rock. These kinematic markers consist of abrasive striae and calcite fibers, which all show dip-slip extensional kinematics (minor dx components of slip). The fault rocks consist of cemented cataclasites. There, the presence of a swarm of comb-veins are documented.

Fig.4.6. *Outcrop oriented W-E in Colliano village with the presence of a normal fault (showing striae and slickenfibers of calcite) and a comb-calcite veins a low angle.*

*At **Monte Carpineta site,*** area 2, the sub-vertical outcrop striking ca E-W exposes bio-lithoclastic limestones with rudists formation (upper slope environment- Upper Cretaceous). The MCPTA sample includes a vein with an attitude N150°/80°NE. The veins is 0.5 cm-thick along a ca. N150°/60° fault characterized by left-lateral transtension (pitch of 45°, Fig.4.7).

Fig.4.7 Outcrop at Monte Carpineta oriented W-E. **(b, c)** Detailes of high angle calcite vein ca. 0.5 cm with attitude N150°/80° NE.

At the ***Senerchia site***, area 3, which lies about 6 km from the Contursi thermal area and about 3 km from the free gaseous emissions (San Sisto, Oliveto Citra sites, see Fig. 2.2), the sub-vertical outcrop trending SW-NE exposes the Lower Jurassic dolomitic limestones and limestones (CLU) of the Carbonate Tectonic Units. The carbonate rock are displaced by a normal fault an attitude N10°/80°ESE with kinematic markers such as striae and calcite steps showing minor dextral components of slip along this trastensional fault (Fig. 4.8). There, calcite comb-veins (CP-vein) with an N210°/25°NW and slip-parallel (SP-vein) are documented (Fig. 4.8).

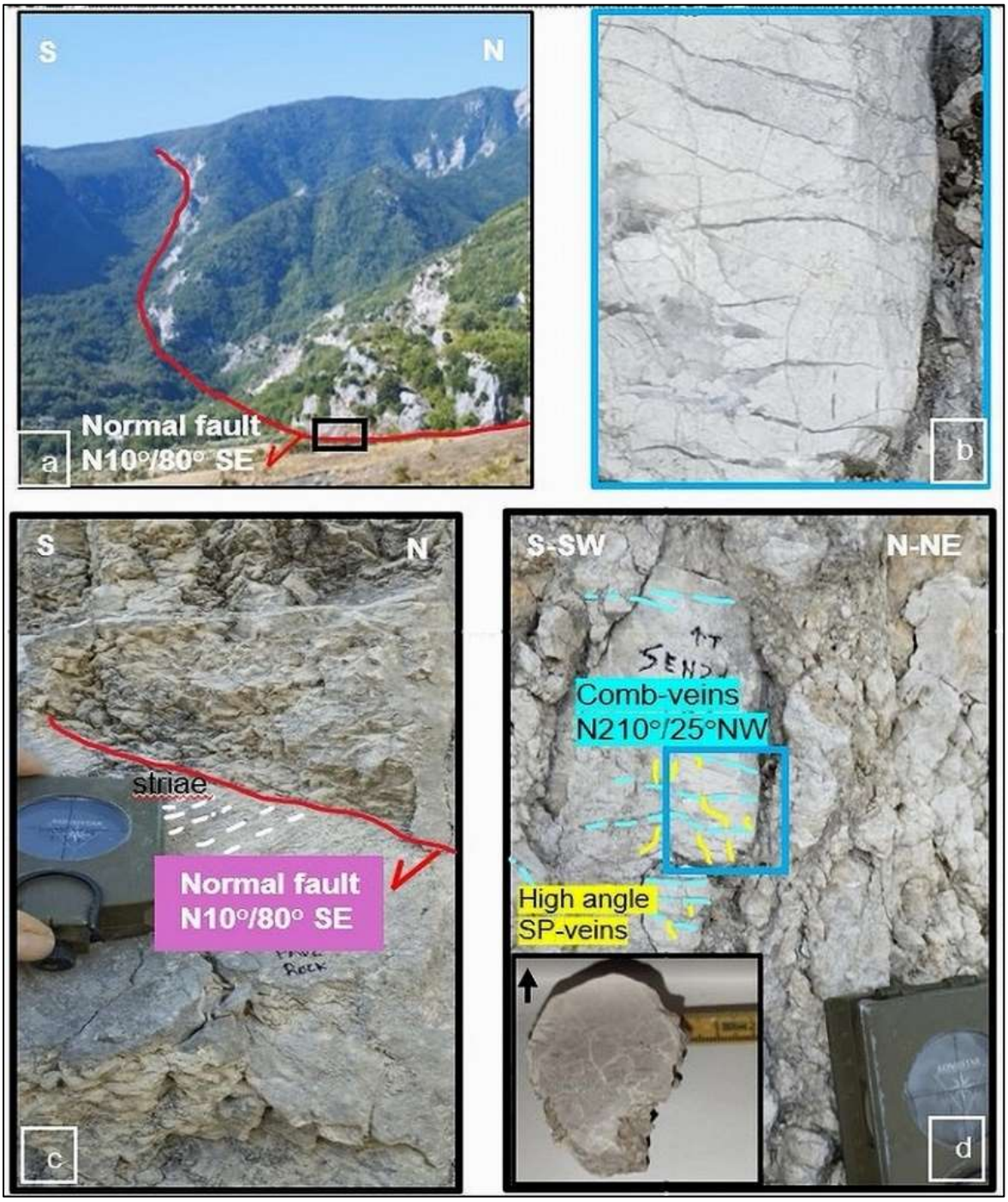

Fig. 4.8 ***(a)*** *Senerchia normal fault site;* ***(b)*** *Detail of photo d, where comb and parallel veins are recognized and sampled;* ***(c)*** *Outcrop oriented ca. N-S with and a presence a normal fault with strike N10°/80°SE and recognized a kinematic indicator (e.g. striae);* ***(d)*** *In a fault rock recognized and sampled a calcite comb-veins with attitude N210°/25°NW (SEN 2.1 sample), and a high angle parallel vein (SP-veins).*

The **Tufaro thermal site,** area 4, (Fig. 4.9) which consists of a sinkhole trending ca. N-S along which a gas vent and travertine rocks localize, exposes Upper Paleogene gray marly limestone, silt clay marl of the Monte Sant Arcangelo formation (Sele Valley tectonic unit). Close to the vent, high angle veins (Fig. 4.9 b, c), crusscut the marly limestone (TUF 1 sample). There, three main sets trending ca N10°, N40° and N100° are documented. The N10° veins are the thickest among the surveyed ones, with a thickness up to 1.5 cm.

Fig.4.9. ***(a)*** *Panoramic view of Tufaro sinkhole, groundwaters with bubble gas and travertine depositions;* ***(b)*** *Set of calcite veins (strike N10°- N40°-N100°) in marly limestone of Tufaro sinkhole;* ***(c)*** *TUF 1 sample details, with a large calcite vein ca. 1-1.5 cm with attitude N10°.*

4.1.2 Micro-structural and textural analyses of calcite veins

In this sub-chapter are describes the main of micro and textural aspects of calcite veins samples analyzed.

The results of microstructural analysis revealed three different calcite veins within MC3 sample, which are respectively labelled as V1, V2, and V3 (Fig. 4.10). Vein V1 (Fig. 4.10a, a', b) consists of a fractured blocky

texture resulting of potentially post-kinematic calcite minerals showing twinning at low angle with respect to the vein walls. In according with literature data by Ferrell. (2004) and Burkhard. (1993), the twins are of type 2, with thick ca. 20µm straight and slightly lense. Vein V2 (Fig.4.10c c') is sub-parallels to vein V1 and includes a potentially syn-kinematics fibrous calcite crystals oblique to the transverse vein walls. The tiny V3 vein is sub-parallel to the previous ones, includes blocky calcites crystals, and crosscut the V2 vein.

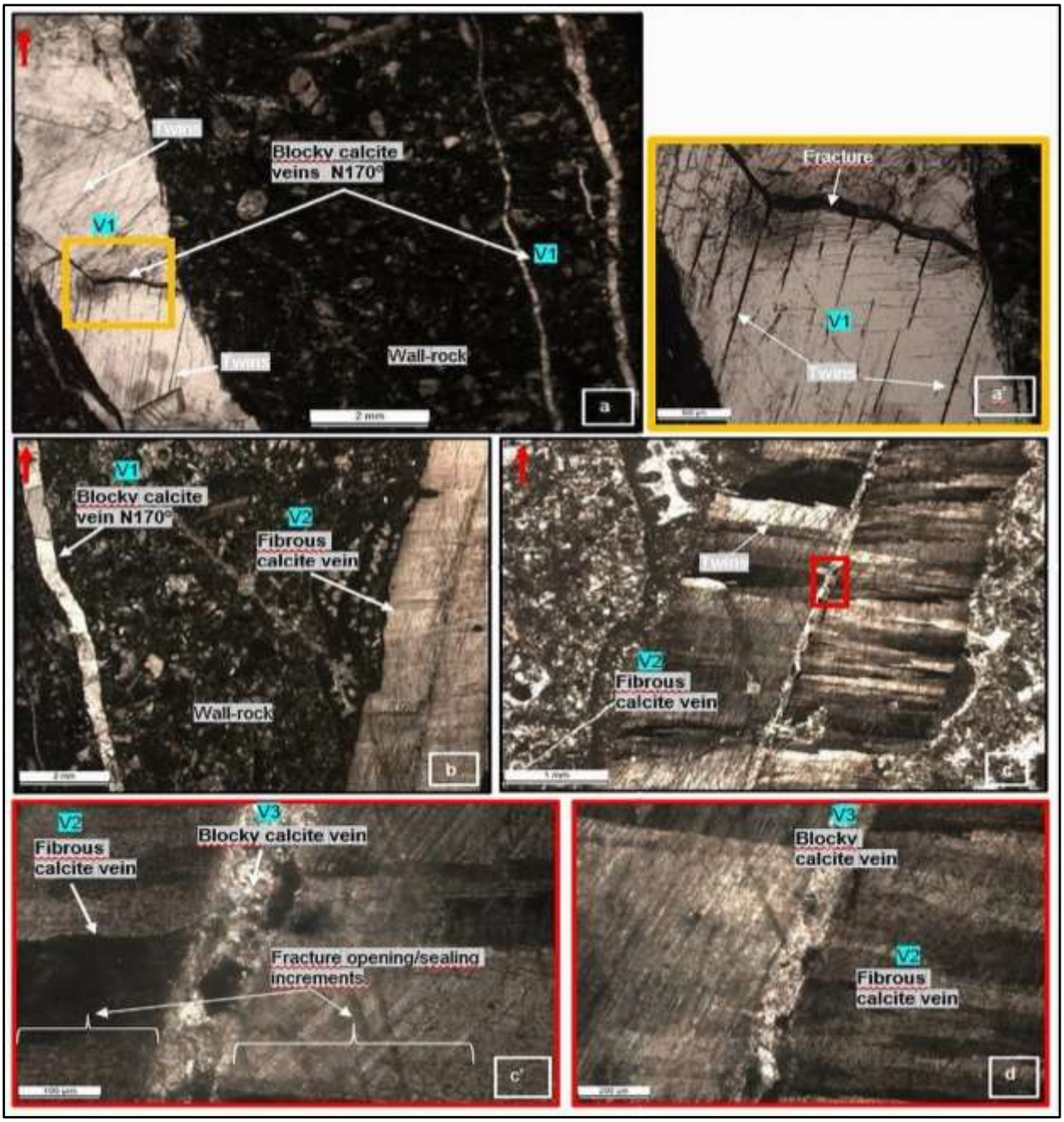

Fig. *4.10.* *Microstructural analysis from MC3 sample fault-related mineralization taken from thigh in sections under an optical microscope cross-polarized light.* ***(a, a')*** *Blocky calcite crystal a high angle in comb-vein mineralization;* ***(b)*** *Blocky calcite crystals (V1), post-kinematic, associated a V2 fibrous calcite vein, syn-kinematic;* ***(c, c', d)*** *Fibrous calcite vein, syn-kinematic (V2) associated a small blocky calcite crystals vein post-kinematic (V3), where fracture opening/sealing increment.*

The results of microstructural analysis of the VRD2 sample (Fig.4.11) are consistent with three different generations of calcite mineralization veins, which are respectively labelled as: V1, V2, V3.

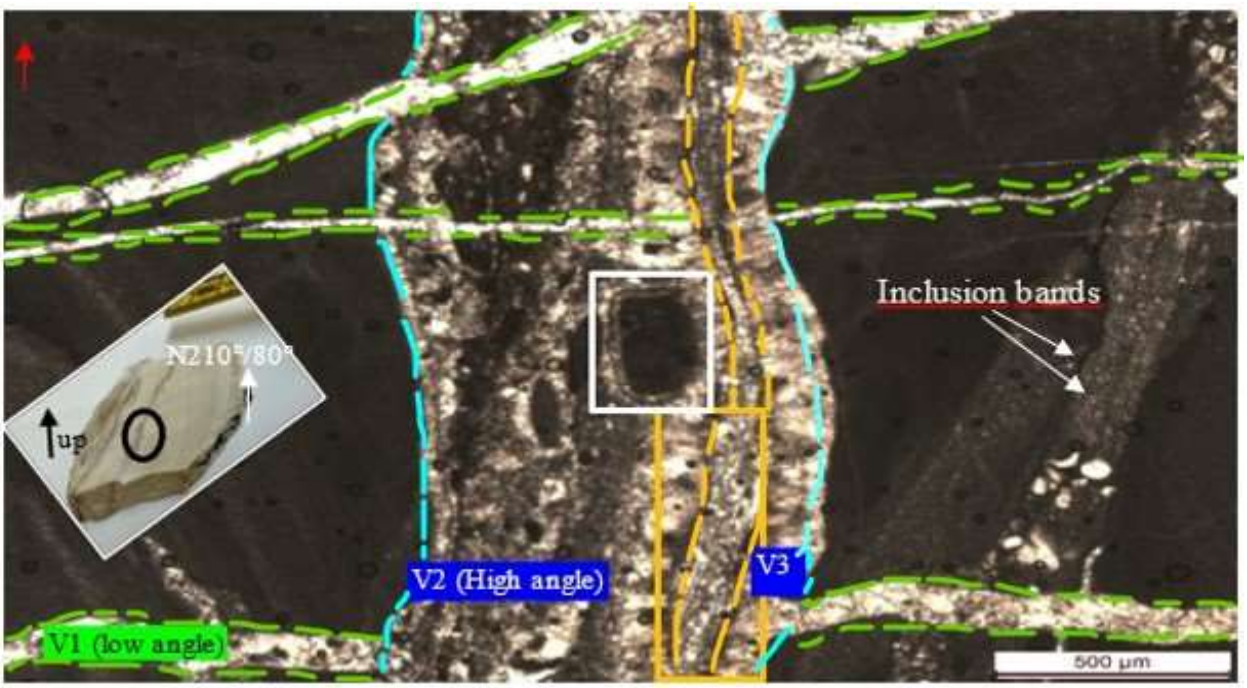

Fig. 4.11 *VRD2 calcite veins sample from thigh in sections under an optical microscope cross-polarized light. Three different veins were recognized: V1 at low angle, V2 and V3 a high angle with strike N210°/80° and ca. perpendicular to V1. A crack and seal mechanism and inclusions band are recognized.*

The high-angle V2 vein, shows an attitude N210°/80°, and it is approximately parallel to the fault plane (N210°/50°). This vein either intersects the low-angle veins (V1) or is crosscut by them. The V1 vein exhibits a calcite blocky crystal. The V2 veins includes blocky calcite crystals. There, evidence of multiple stages of fracture opening and sealing due to mineral precipitation (crack and seal mechanism) are shows in orange rectangle. The latest V3 veins are not intersected by any other vein and are thus interpreted as the youngest. Additionally, presence of overpressured breccia is observed with a clast (in a white rectangle) that displaying a crown of mineralization. An inclusion bends is also shown in the figure. Based on this analysis, V1 and V2 veins can be considered part of the same generation, whereas V3 post-dates V2 (and V1) due to subsequent reopening of the fracture and fluid overpressure input.

The results by optical microscope analysis of CP2 sample in Colliano Village (Fig. 4.12), reveal that the comb vein are characterized by calcite with a blocky texture and calcite twinning. Twinning of calcite is at a high angle relative to the vein walls (Fig. 4.12b), thus indicating that mineralization occurred during intracrystalline deformation associated to the latest tectonic events. Also, the presence of a crack and seal texture and of inclusion bands are recognized.

Fig.4.12. ***(a)*** *A textural analysis by optical microscope shows a sub-horizontal calcite comb-veins within some cases they are deflected.* ***(b)*** *A crack and seal mechanisms with inclusion bands and thin twinning of calcite crystals, are recognized.*

The microstructural and textural results conducted by optical microscope analysis revealed three different calcite veins within MCPTA sample, (Fig.4.13a): V1 vein, a dominant presence of fractured calcite blocky crystals. In these crystals thin twinning (with a thickness > 1µm) is recognized, testify an intracrystalline deformation late tectonic events., also, a vertical stylolite with horizontal bordering the walls of vein V1.

The V2 vein (Fig.4.13a, b) characterized by blocky calcite crystals, appears to 45° slope the V1 vein and cut the smaller V3 vein. This suggests that the V2 vein post-date the V3. In contrast, the V3 vein contains fibrous calcite and inclusions bands crystals exhibiting a potentially syn-cinematic texture. Based on the crosscutting relationships between the various veins, the first vein to form is V3, which is cut by V2 vein with fibrous calcite crystals and finally cut by V1, the last to form with blocky calcite crystals. Furthermore, an isolated calcite elongate blocky are recognized with these veins (Figs. 4.13b, c, d), with a inclusion bands with crack and seal mechanism, suggests a coeval dilatation and mineralization process, where fractures are filled with mineral precipitates during deformation. The elongate blocky texture forms when nucleation of new grains does not occur during vein growth, and all growth is by crystallographically continuous overgrowths on existing grains and growth occurs at the tips of existing crystals. The “seed grains” can be pre-existing grains in the wall rock of a vein, or grains formed during an initial nucleation stage. Elongate blocky texture show evidence for crystallographically controlled growth competition between grains.

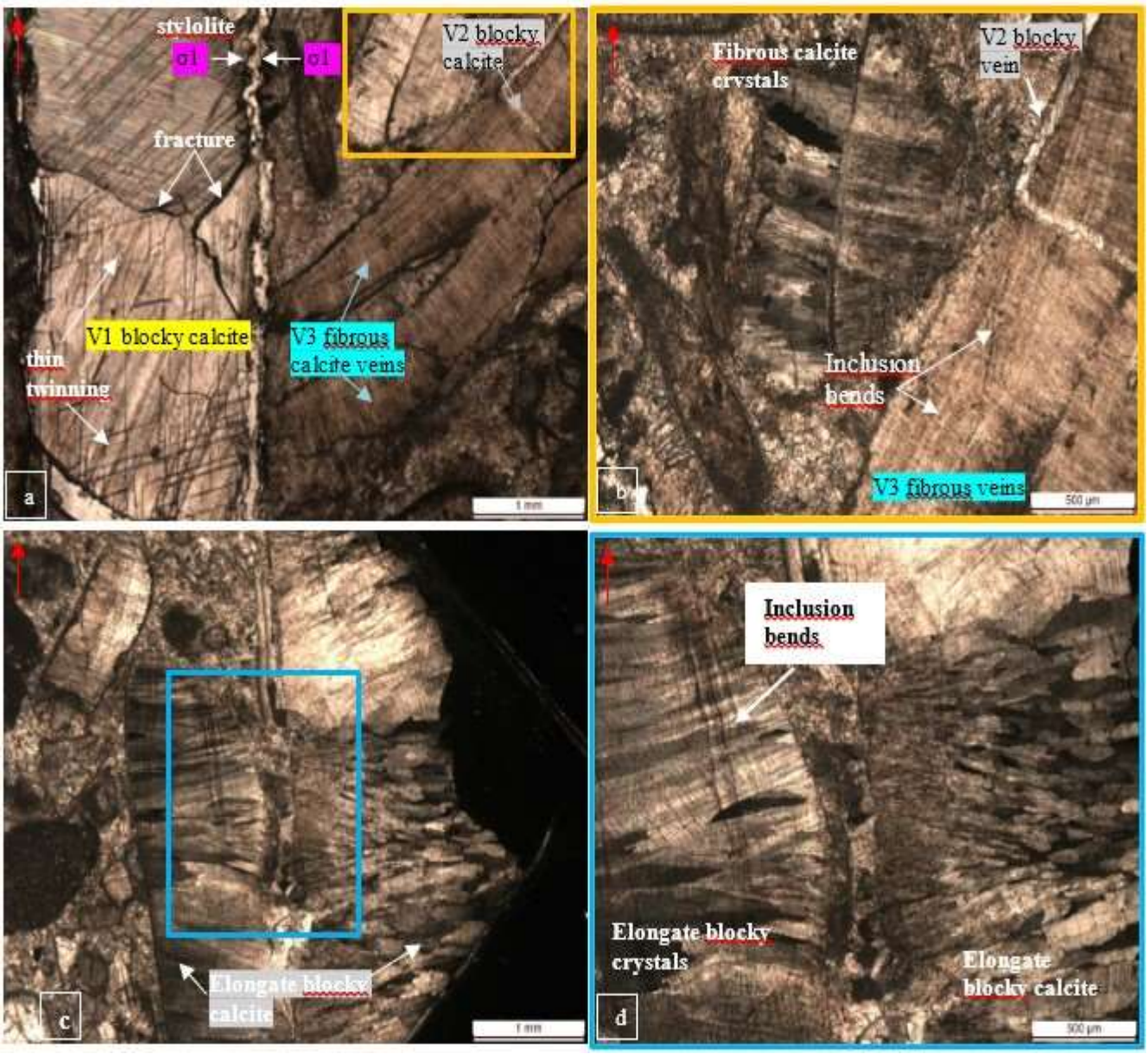

Fig.4.13. *Microstructural and textural results of MCPTA sample from optical microscope.* ***(a)*** *MCPTA sample with three mineralization veins (V1, V2, V3) and stylolite are recognized; also, in V1 the calcite revealed the thin twinning* ***(b)*** *Enlargement of the orange rectangle showing V2 vein and fibrous calcite vein and inclusion bends;* ***(c, d)*** *an elongate blocky calcite crystal with the presence a inclusion bends.*

The microstructural and textural results by mean of optical microscope analyses of the SEN 2.1 sample (Fig. 4.14) confirms the presence of two distinct types of veins associated with the normal fault, which respectively are the low-angle comb veins (CP-veins) and the high-angle slip-parallel veins (SP-veins). The CP veins cut across the SP veins (Fig. 4.14a, c). Both the CP and SP veins exhibit calcite crystals with a blocky texture, suggesting that they were sealed during post-tectonic mineralization. Within the CP veins, the blocky calcite crystals display clear growth structures (Fig. 4.14d), as well as type I and/or II twinning testifying intracrystalline deformation.

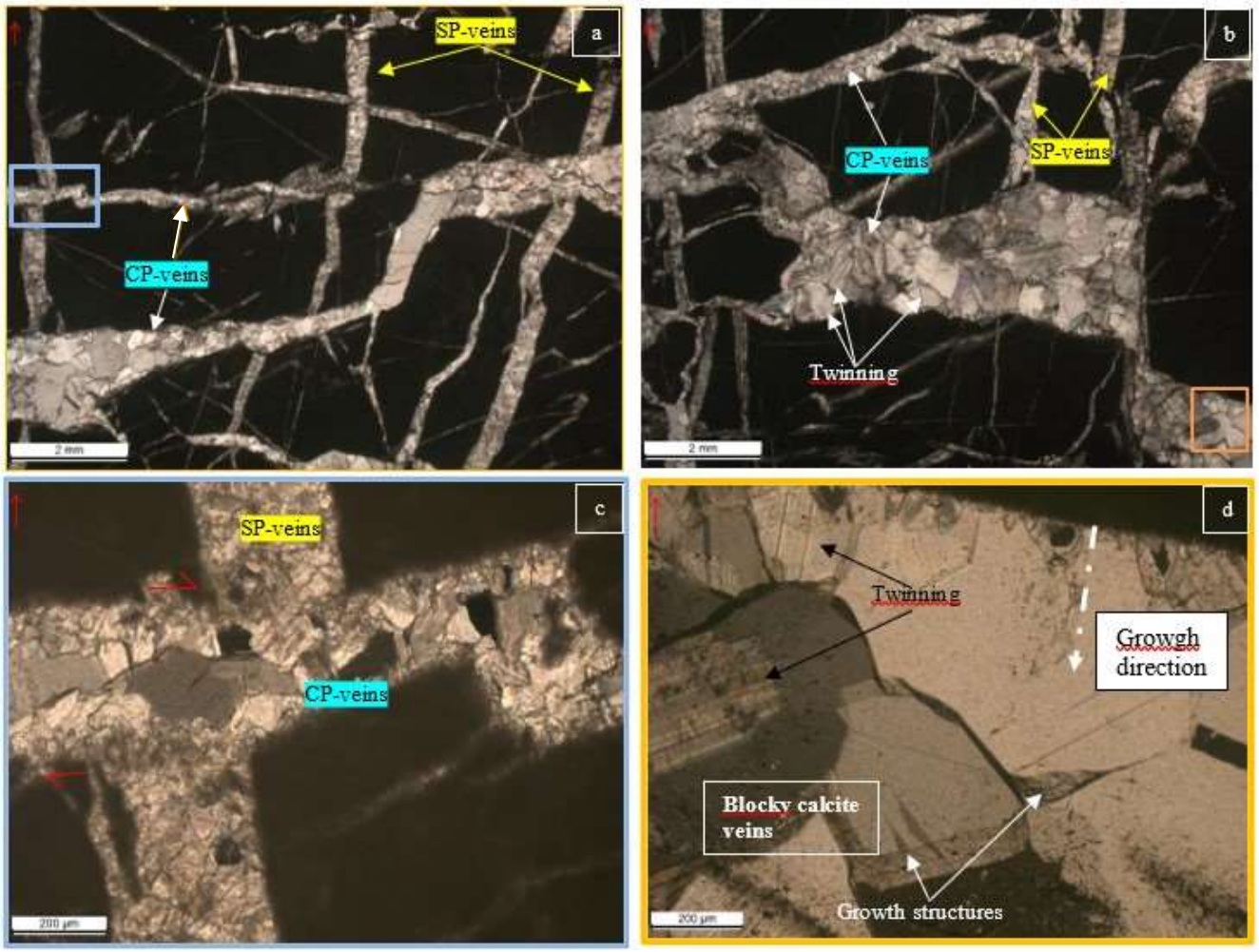

Fig. 4.14 (a, b) *Microstructural results of SEN 2.1 sample form optical microscope of the CP-veins and SP-veins.* ***(c, d)*** *Are the enlargements of the highlighted rectangles in photo a and b respectively, where the deformation mechanism of twinning and the growth structures of calcite crystals with blocky texture are identified.*

The microstructural and textural results by optical microscope analysis of T.CAP sample (Fig. 4.15a), confirmed presence of the two sets of calcite veins. V1 (Fig. 4.15a, b) presents predominant calcite crystals showing a blocky massive texture. The calcite minerals are thin-twinned (type II, which twin >> 1 µm), consistent with intracrystalline deformation (Ferrill, 1991; Ferrill et al., 2004). In some cases, the calcite crystals show inclusion bands with crack-and-seal textures. The V2 vein, thinner that V1, is made up of calcite crystals with a blocky texture, as well as crack-and-seal texture. V2 is displaced by V1.

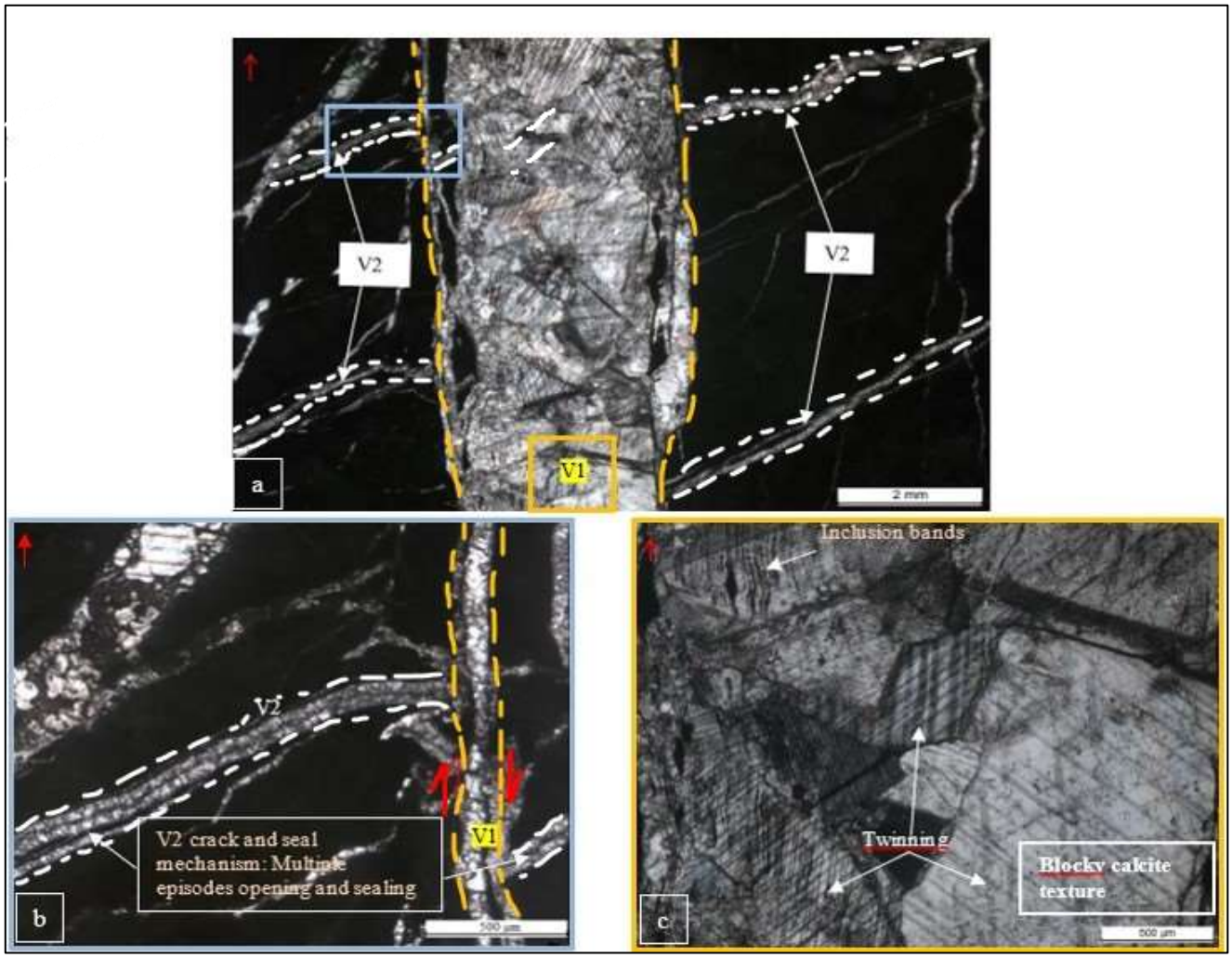

Fig.4.15 (a) *T. CAP sample which recognized two main calcite veins from optical microscope analysis: V1 and V2, with a particolar focused in orange and blue rectangle respectively;* ***(b)*** *Focused in V2 vein: this present a blocky calcite crystals and is cut by V1 high angle vein (red arrows); furthermore has a multiple phases of opening and sealing with inclusion bends (crack and seal mechanism);* ***(c)*** *particular of V1 vein: this present an blocky calcite texture, with inclusion bands and presence of twinning (type II).*

The results of textural and microstructural analysis by optical microscope of the TUF 1 sample, in Tufaro Sinkhole site (Fig. 4.16a) confirm presence of the V1 (strike N10°), V2 (strike N40°) and V3 (strike N100°) veins. The V1 vein is constituted by a large, fractured calcite crystal with a blocky texture. In some cases, this vein presents a completely twinned and curved thick twins (Fig 4.16) due to intracrystalline deformation (Ferrill et al., 2004). The V2 vein exhibits blocky massive calcite crystals. The V3 vein is made up of blocky calcite crystals with a crack-and-seal textures. On the basin of the crosscutting relations, we note that the V1 veins are cut by the V2 veins and that the V3 cut across both the V1 (Fig. 4.16b) and V2 veins. Accordingly, the V1 veins are the oldest, whereas the V3 are the youngest.

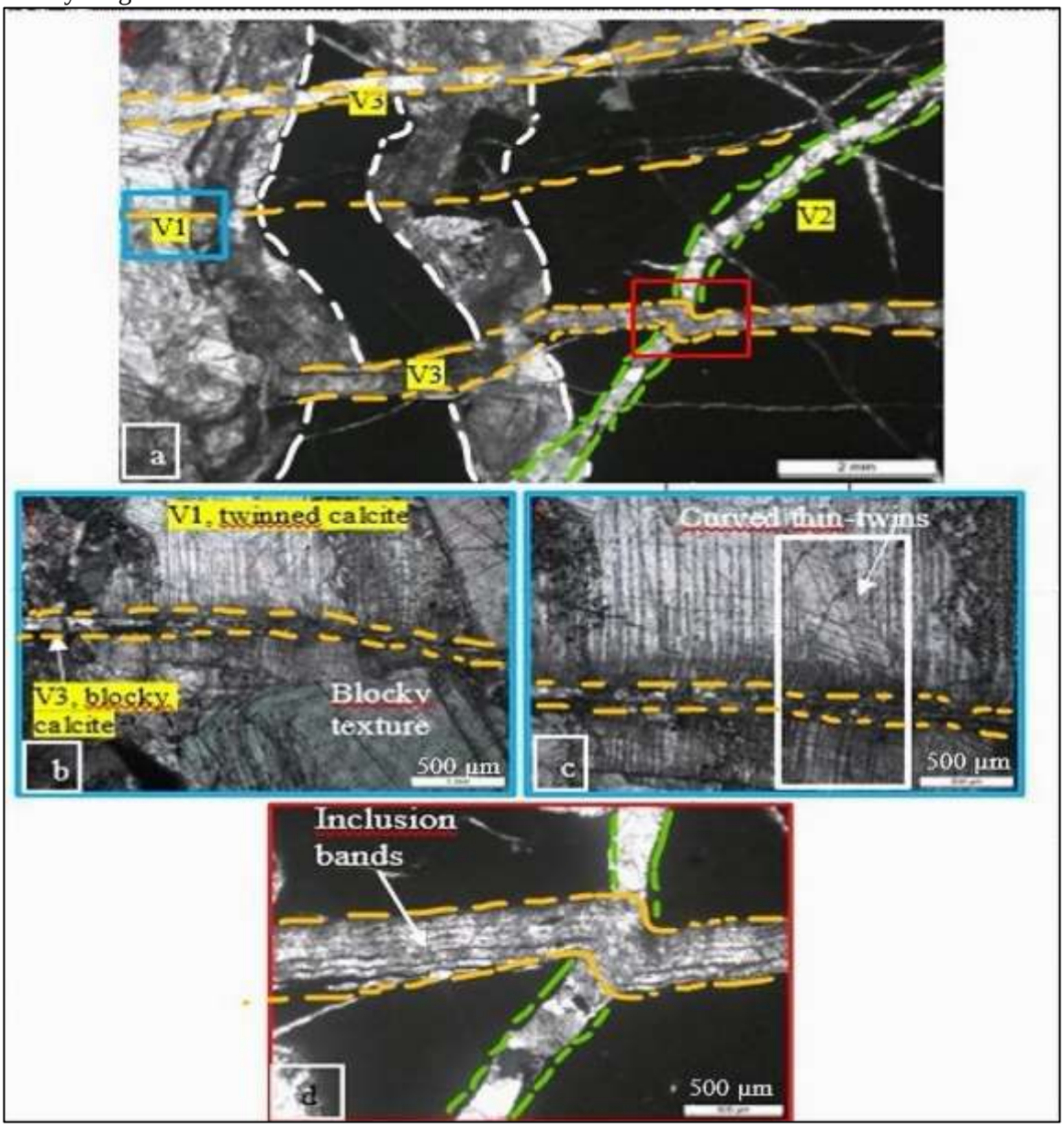

Fig.4.16 (a) *TUF 1 sample from optical microscope analysis: recognized three different high angle calcite veins with attitude N10°(V1)-N40°(V2)-N100°(V3);* ***(b, c)*** *V1 calcite veins with blocky texture and curved thick twins similar a previous study (Ferrill, 1991; Ferrill et al., 2004);* ***(d)*** *A crack and seal mechanism in V3 vein. Also, this vein cuts the N10° and the N40° veins.*

The results of textural and microstructural analysis by optical microscope from PR4N20 sample, (Fig. 4.17) show that the vein N20° veins is made up of calcite crystal with blocky texture. In some cases, these crystals are twinned type I and/or II (twins thick > 1 µm), testifying the intracrystalline deformation. Also, this N20° vein cuts across by microveins approximately perpendicular of this late.

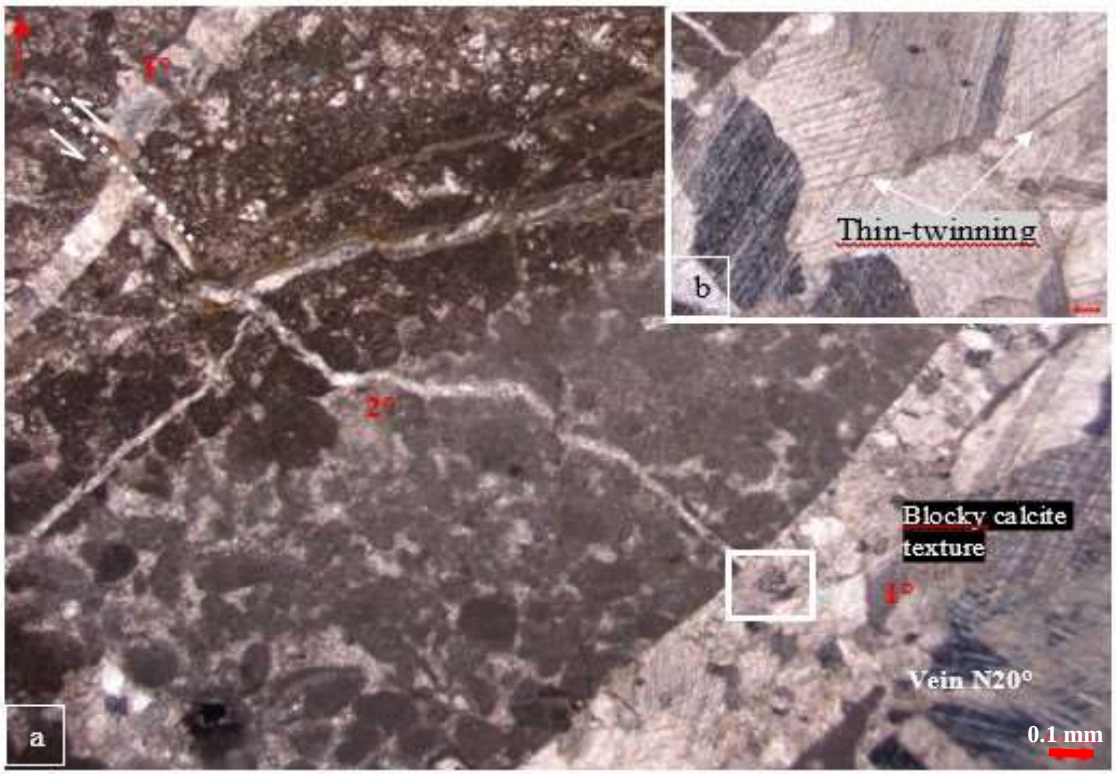

Fig. 4.17 ***(a)*** *textural results by optical microscope of PR4N20 veins which two families of vein are identified: the N20° vein (1°) studied and microveins (2°) ca. perpendicular which cut them and develop later.* ***(b)*** *Detail of the N20 vein where the calcite minerals have a blocky texture, and it is show that they are affected by thin twinning (type I and/or II).*

4.2 CHEMICAL AND ISOTOPIC ANALYSIS

In this sub-chapter, are reported the main results of chemistry (major, trace and REE +Y elements) and stable carbon and oxygen isotopes compositions ($\delta^{13}C$ – $\delta^{18}O$) of fault-related calcite veins and associated host rocks.

4.2.1 Major, Trace elements and REE-Y patters

In table 4.1 are reported the chemical data of major elements (expressed in % weight) in calcite veins and associated carbonate host rocks (T.CAP_H, PR4N20_H, CVR_H, CP1_H samples). In these veins, the major chemical element is CaO, with values between 53.7 and 55 %, the other elements have low values, such as MgO varying between 0.31 and 0.78 %, SiO_2 from 0.26 to 1.50 %, Al_2O_3 from 0.10 to 0.31 %. The analyzed samples of calcite mineralization veins show a partner similar to one of Campania-Lucana and Apulian carbonate platforms (Rosatelli et al., 2023).

Tab. 4.1. Major elements contents in mineralization veins and host rocks associated, expressed in % weight.

ID samples	SiO_2 (%)	Al_2O_3 (%)	Fe_2O_3 (%)	MnO (%)	MgO (%)	CaO (%)	Na_2O (%)	K_2O (%)	TiO_2 (%)	P_2O_5 (%)	S (%)	LOI (%)	Total %
T.CAP	0.40	0.13	0.37	0.06	0.78	53.31	0.05	0.02	0.002	b.d.l	0.04	43.4	98.51
T.CAP_H	0.40	0.15	0.36	0.03	3.07	50.52	0.04	0.02	0.003	0.01	0.02	44.08	98.68
PR4N120	1.50	0.12	0.08	b.d.l	0.37	54.20	0.04	0.02	0.002	0.07	0.01	42.57	98.97
PR4N20	0.37	0.15	0.07	b.d.l	0.38	54.57	0.05	0.03	0.003	0.34	0.01	42.54	98.50
PR4N20_H	0.37	0.17	0.06	b.d.l	0.40	54.53	0.03	0.04	0.006	0.46	0.02	42.52	98.59
CVR	0.34	0.14	0.06	0.01	0.41	54.73	0.03	0.02	0.003	0.01	0.01	42.84	98.60
CVR_H	0.31	0.12	0.07	0.01	0.40	54.43	0.06	0.02	0.003	0.35	0.02	42.94	98.70
PR1W3	0.57	0.29	0.11	b.d.l	0.36	54	0.05	0.04	0.011	0.07	0.01	43.03	98.54
PR1E	0.72	0.31	0.13	b.d.l	0.49	53.65	0.09	0.06	0.007	b.d.l	0.02		55.48
MC3_V1	0.29	0.11	0.06	0.01	0.46	54.37	0.04	0.02	0.002	0.04	0.03	43.21	98.61
VRD02	0.58	0.24	0.08	b.d.l	0.61	53.97	0.06	0.04	0.007	0.03	0.04	42.95	98.57
VRD1.1	0.32	0.12	0.06	b.d.l	0.41	55.07	0.05	0.02	0.001	0.02	0.02	42.87	98.96
VRD2	0.40	0.16	0.15	b.d.l	0.54	53.94	0.07	0.02	0.002	0.05	0.04	43.33	98.67
CVR3	0.43	0.19	0.09	b.d.l	0.51	54.72	0.04	0.04	0.007	0.14	0.02	43.39	99.55
CP1	0.26	0.10	0.04	b.d.l	0.31	54.58	0.04	0.01	0.001	0.36	0.01	42.94	98.64
CP1_H	0.32	0.13	0.05	b.d.l	0.33	54.41	0.06	0.02	0.003	1.55	0.04	41.63	98.49

Note: b. d. l (Below detection limit), MnO =0,005; P_2O_5 = 0,01. LOI (Loss on Ignition) is one of the most widely used methods for measuring organic matter content in soils. With the final H in the samples ID indicated the rock host.

Regarding trace elements (Table 4.2), the most abundant is Sr (median = 193 ppm in mineralization veins, and 300 ppm in carbonate host rocks), while further trace elements such as Ba (median = 4.69 ppm in mineralization veins and 8.65 ppm in host rocks), U (median = 0.42 ppm in veins and 0.74 ppm in host rocks), Zn (median = 6.30 ppm in veins and 5.75 ppm in host rocks), Ni (median = 3 ppm both in veins and host rock), V (median = 12.6 ppm in veins and 33 ppm host rock), Cu (median = 4.43 ppm in veins and 2.6 ppm host rock), Th (median = 0.09 ppm in veins and 2.6 ppm in host rock) show lower abundances. The other trace elements have values lower than detection limits (B. d. l).

Large ion lithophile elements (LILE), high field strength elements (HFSE) and transition metals have been

normalized to UCC (upper continental crust, McLennan, 2001;). The Sr values in our samples analyzed lie between 111 ppm and 386 ppm, with an average of 218 ppm, which is lower than the average Sr content (350 ppm) of the Post-Archean Australian Shales (PAAS, Pourmand et al., 2012), commonly used as the reference reservoir for normalizing limestone values.

In Fig 4.18 Rb/Ba vs Rb/Sr ratios (a), Rb/Sr vs La/Yb ratios (b) in the studied calcite veins and carbonate host rocks are reported. The data are compared with the Campania-Lucania carbonate platforms and Apulian carbonate platforms (Rosatelli et al., 2023), carbonate veins of Monte Morrone fault in central Italy (Coppola et al., 2018), groundwaters in Contursi hydrothermal basin (Gori et al., 2023). As can be seen from Figure 4.18 a, b, all samples fall in between Campania and Apulian carbonate platforms samples and cold and thermal groundwaters of the Contursi hydrothermal basin.

Tab. 4.2 Trace element contents of the calcite veins analyzed and limestone host rock associate such as: T. CAPH, PR4N20H, CVRH, CP1H, expressed in ppm. B. d. l (below detection limit).

Samples	T.CAP	T.CAPH	PR4N120	PR4N20	PR4N20H	CVR	CVRH	PR1W3	PR1E	MC3_V1	VRD0	VRD1.1	VRD2	CVR3	CP1	CP1H	CVRH
Trace elements	vein	host rock	vein	vein	host rock	vein	host rock	vein	vein	vein	vein	vein	vein	vein	vein	host rock	host rock
Sr	161	169	111	167	152	214	386	175	143	272	193	262	239	169	258	261	386
Ba	6	9	4	3	4	4	9	8	5	3	4	5	4	5	6	8	9
U	0.91	2.18	0.36	0.47	0.8	0.03	0.12	0.76	0.28	0.12	1.08	0.14	0.16	0.2	0.18	0.56	0.12
Th	b.d.l	0.06	0.05	0.05	0.1	bdl	0.06	0.18	0.09	b.d.l	0.12	b.d.l	b.d.l	0.09	b.d.l	0.05	0.06
Zn	4	6	6	4	8	3	6	6	8	8	11	4	11	5	4	5	6
Cu	7	3	7	3	2	2	3	3	7	5	3	8	4	2	1	2	3
Ni	8	3	6	2	2	2	3	2	5	3	1	2	3	2	1	b.d.l	3
V	14	33	b.d.l	15	20	b.d.l	b.d.l	8	b.d.l	b.d.l	b.d.l	b.d.l	6	b.d.l	b.d.l	b.d.l	b.d.l
Zr	4	4	4	4	5	3	3	5	4	4	4	3	4	5	3	5	3

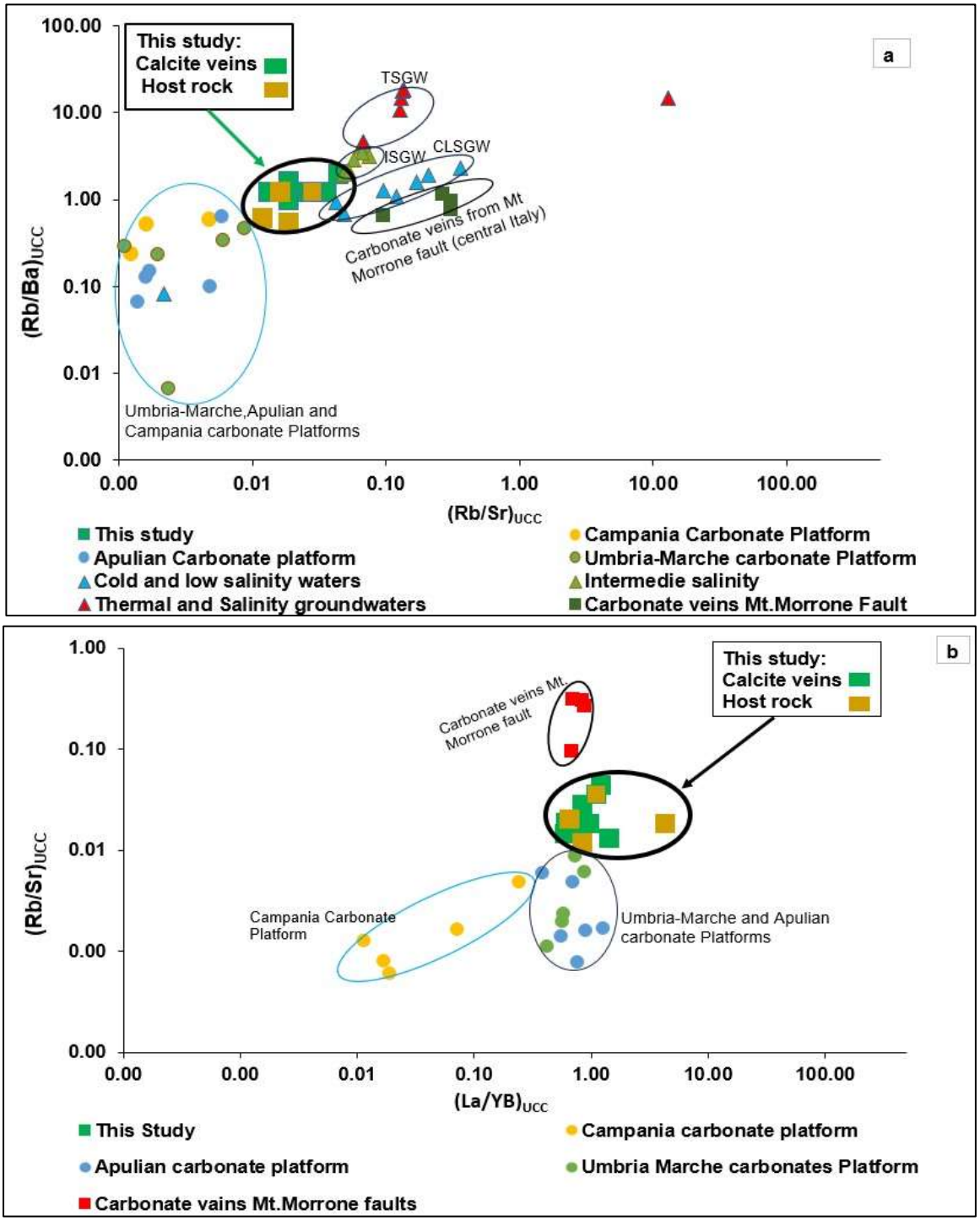

Fig.4.18. *Trace elements plots.* ***(a)*** *Rb/Ba vs Rb/Sr plot;* ***(b)*** *Rb/Sr vs La/Yb plot. Green rectangles depict the samples of mineralization veins and carbonate host rocks analyzed. References: Lucania, Apulian and Campania carbonates Platforms (Rosatelli et al., 2023); carbonate veins from Monte Morrone fault (central Italy, Coppola et al., 2021), groundwaters from Contursi hydrothermal basis (Gori et al., 2023)*

Contents (ppm) of REE+Y in all studied samples (including calcite infills, carbonate and dolomitic limestone host rock) are reported in Table 4.3 along with the average compositions of limestone from the Apulian, Lucania, Campania Platforms (Rosatelli et al., 2023).

Tab. 4.3. *Content of REE+Y of the related fault-veins and host rock associated. Data are in ppm. T. CAPH, PR4NH, CVRH, CP1H = host rock samples. b. d. l = below detection limit. Reference data of Campania-Lucania carbonate platforms, Lagonegro basin, Apulian carbonate platform and Umbria-Marche carbonate platforms from Rosatelli et al. (2023). Ce anomaly (Ce/Ce*) calculated from the normalized values respect to PAAS composition)*

Sample	T.CAP	T.CAPH	PR4N120	PR4N20	PR4N20H	CVR	CVRH	PR1W3	PR1E	MC3_V1	VRD02	VRD1.1	VRD2	CVR3	CP1	CP1H	Reference			
REEY Element	vein	host rock	vein	vein	host rock	vein	host rock	vein	vein	vein	vein	vein	vein	vein	vein	ıost hos	Camp-Lucan Platf.	Lagon. Basin	Apul. Plat.	Jmb-Marc. Platf.
Sc	b. d. l	b. d. l	b. d. l	b. d. l	b. d. l	b. d. l	b. d. l	b. d. l	b. d. l	b. d. l	b. d. l	b. d. l	b. d. l	b. d. l	b. d. l	b. d. l	0.07	0.43	0.29	0.51
La	0.47	0.57	0.5	0.87	1.35	0.52	3.91	1.32	1.48	0.99	0.78	0.39	0.43	1	1.52	5.51	0.23	1.47	2.34	4.6
Ce	0.8	1.05	0.66	0.73	0.89	0.48	1.61	1.15	1.36	0.59	1.32	0.28	0.41	0.72	0.31	0.7	0.25	1.81	1.52	4.22
Pr	0.1	0.09	0.07	0.09	0.11	0.08	0.51	0.18	0.21	0.15	0.13	0.04	0.05	0.12	0.11	0.36	0.04	0.42	0.45	0.92
Nd	0.33	0.33	0.27	0.39	0.48	0.37	2.21	0.71	0.88	0.71	0.51	0.17	0.22	0.46	0.47	1.64	0.18	1.91	1.95	3.88
Sm	0.04	0.07	0.05	0.08	0.07	0.07	0.50	0.1	0.18	0.13	0.08	0.04	0.05	0.07	0.08	0.26	0.03	0.46	0.41	0.82
Eu	b. d. l	0.02	0.01	0.01	0.02	0.02	0.12	0.04	0.04	0.03	0.02	0.01	0.01	0.01	0.02	0.07	0.006	0.11	0.1	0.2
Gd	0.02	0.06	0.04	0.07	0.11	0.08	0.49	0.14	0.14	0.19	0.11	0.05	0.04	0.08	0.14	0.45	0.03	0.56	0.52	0.98
Tb	b. d. l	b. d. l	b. d. l	0.01	0.01	0.01	0.08	0.02	0.02	0.02	0.01	b. d. l	b. d. l	0.01	0.01	0.07	0.003	0.08	0.07	0.14
Dy	0.03	0.01	0.01	0.06	0.09	0.06	0.52	0.11	0.11	0.16	0.08	0.03	0.02	0.08	0.13	0.48	0.2	0.52	0.5	0.9
Y	b. d. l	b. d. l	b. d. l	2	3	1	6	2	3	2	1	b. d. l	b. d. l	2	3	12	0.21	4.72	4.78	0.19
Ho	0.01	b. d. l	b. d. l	0.02	0.04	0.02	0.12	0.03	0.03	0.04	0.02	0.01	0.01	0.02	0.04	0.16	0.004	0.1	0.11	8.19
Er	0.02	0.01	0.02	0.08	0.13	0.06	0.33	0.09	0.09	0.12	0.05	0.03	0.03	0.08	0.13	0.48	0.01	0.29	0.34	0.57
Tm	0.01	b. d. l	b. d. l	0.01	0.02	0.01	0.06	0.02	0.02	0.02	0.01	0.01	< 0.005	0.01	0.02	0.07	Bdl	0.03	0.05	0.07
Yb	0.03	0.01	0.04	0.1	0.14	0.06	0.32	0.08	0.08	0.13	0.07	0.04	0.02	0.07	0.12	0.44	0.01	0.23	0.29	0.48
Lu	0.00	0.00	0.01	0.01	0.02	0.01	0.05	0.01	0.01	0.02	0.01	0.01	0.00	0.01	0.02	0.07	bdl	0.03	0.04	0.13
$(Ce/Ce^*)_{PAAS}$	0.89	1.12	0.85	0.63	0.56	0.57	0.27	0.57	0.59	0.37	1	0.54	0.67	0.5	0.18	0.12				

The REE+Y abundance of calcite veins are variable and generally lower than 3 ppm, except for Y whose concentrations range between 1 ppm and 6 ppm. In respect to the PASS composition, samples studied have low REE+Y values. In comparison with the host rock, the REE+Y vein contents are mostly lower than also confirmed by the normalization patterns shown in Fig. 4.19a. It is worth of note that calcite vein infills are characterized by a relative HREE enrichment in respect to the crustal standard. Such enrichment is comparable to that of seawater sediments which is commonly associated to the REE complexation by CO_3^{2-} and/or other dissolved ligands (Pipar and Bau. 2013). In figure 4.19b the $REE+Y_{PAAS}$ patterns of the mineralization fall between those of the Campania-Lucania carbonate platforms on the botton and the Apulian carbonate and the Lagonegro basin on the top (Rosatelli et al., 2023). Furthermore, all studied samples veins are characterized by LREE depletion (Nd_{PAAS}/Yb_{PAAS} = 0.31 – 0.89), negative Ce anomaly (Ce/Ce* = 0.18 – 1) typically observed in marine carbonates.

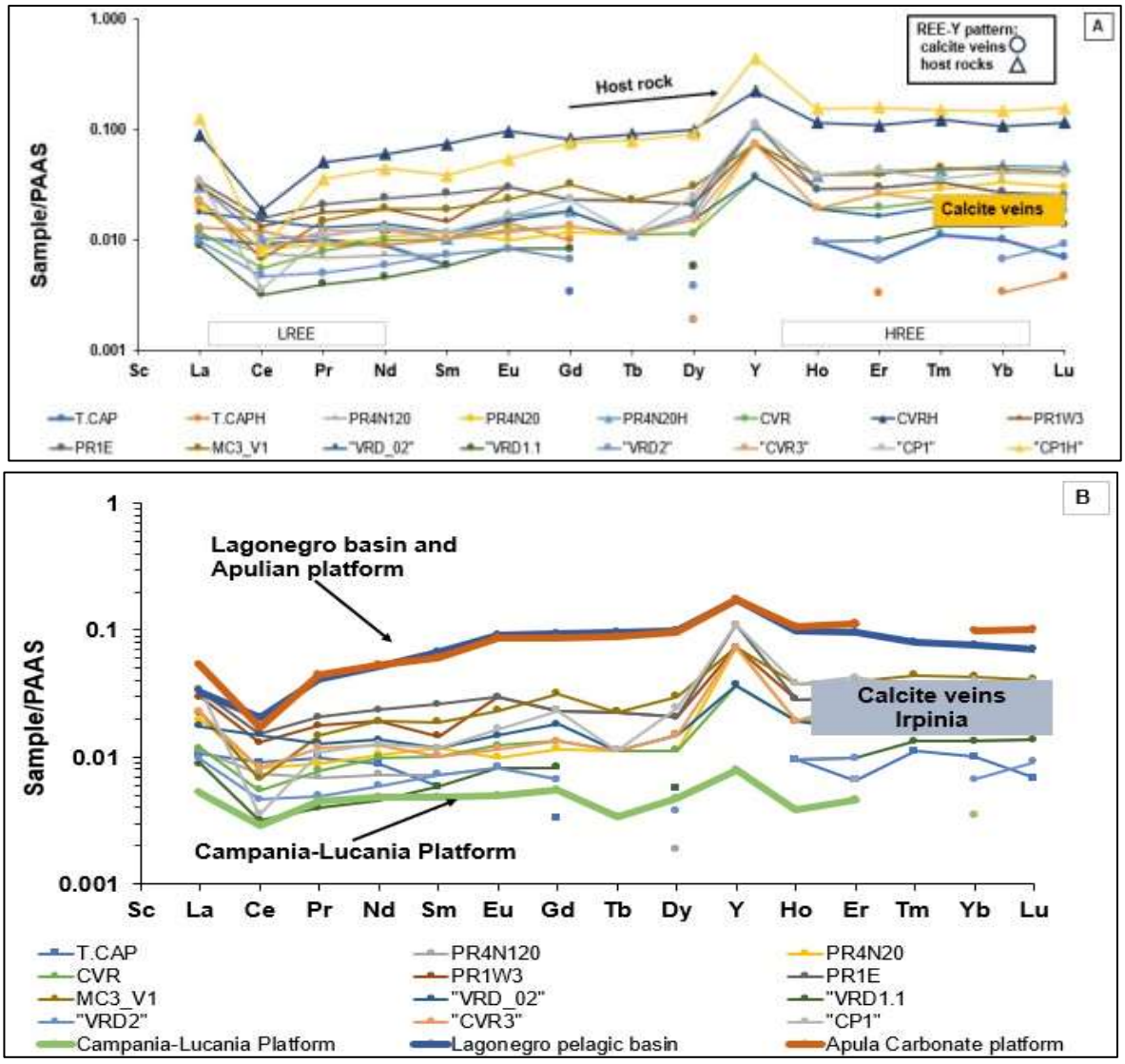

Fig. 4.19. *The distribution patterns of REE+Y normalized to PAAS (Poumand et al.,2012).* ***(a)*** *Plot of veins and associated host rock used for this study;* ***(b)*** *Plot of calcite mineralization veins used for this study; the results are compared with: Campania-Lucania, Apulian carbonate platforms and Lagonegro basin by Rosatelli et al. (2023).*

4.2.2 Mineralogical association of fault-related veins

In Table 4.4, are reported the results of the mineralogical analysis conducted at the XRD (X-Ray Diffractometry) laboratory of University of Basilicata.

Based on a semi-quantitative analysis, most of the veins samples consist of prevailing calcite (95 – 100%) and scarce dolomite (0 – 5%). The host rock associated consists of a prevailing calcite mineral (95 -100%) and dolomite minerals (0-5%). Only the T. CAPH host rock has a high content of dolomite (18%) and a lower amount of calcite (82%). This is probably because of the presence in such rock of a ligh brown and gray marly limestones which have a higher Mg content (e.g. $MgCa(CO_3)_2$).

Table 4.4 Mineralogical results by XRD analysis of veins infills and host rock, expressed in % wight.

Samples	Tipology	Calcite	Dolomite
T.CAP	Vein	100	0
T.CAP_H	Host rock	82	18
CVR	vein	98	2
CVR_H	host rock	97	3
PR4N20	vein	99	1
MC3_V1	vein	96	4
PR1W3	vein	95	5
PR1E	vein	95	5
VRD02	vein	97	3

In Figure 4.20, are reported the diffractograms of samples studied where the main diffraction peaks of the calcite (CaCO3, 29° 2θ), and dolomite ($MgCa(CO_3)_2$, 31°2θ) minerals are well distinguishable.

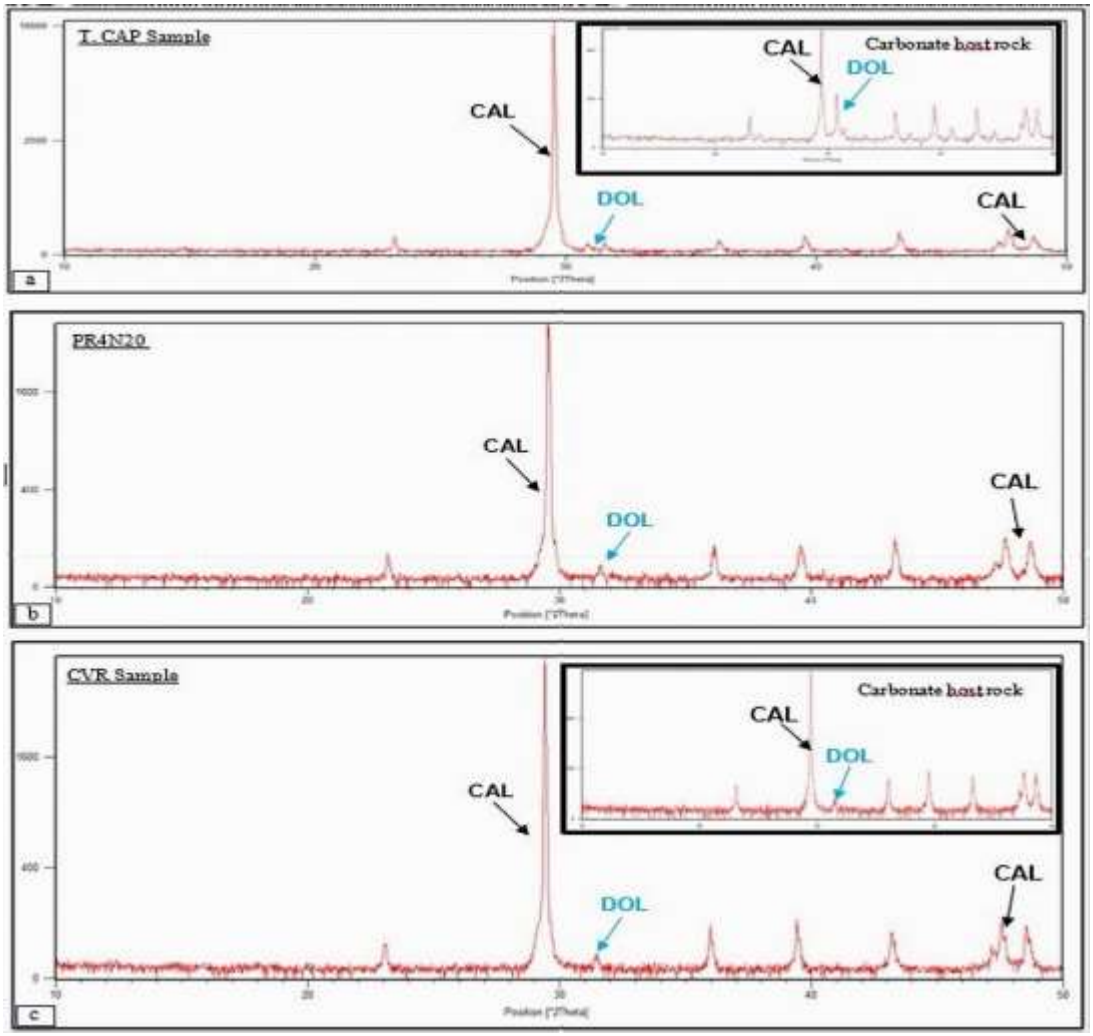

Fig.4.20. *XRD patterns of the selected studied veins and associated carbonate host rock. CAL = Calcite; DOL = Dolomite; (**a**) T.CAP sample: (**b**) PR4N20 sample; (c) CVR sample.*

4.2.3 Carbon and Oxygen stable isotopes of calcite veins and carbonate host rock

The stable isotope composition ($\delta^{13}C$ and $\delta^{18}O$) of studied calcite veins-fault related and associated host rocks are reported in Table 4.5. The analytical error both $\delta^{13}C$ and $\delta^{18}O$ are ± 0.2‰. The isotopic data was reported in the conventional δ notations with respect to the Vienna Pee Dee Belemnite (VPDB) for carbon isotopes and in the conventional δ notations in Vienna Standard Mean Ocean Water (VSMOW) for $\delta^{18}O$. Considering that the dolomite in the mineralization veins studied samples varies from 0 to 5 %, we will only consider carbon and oxygen isotope values in calcite.

Table 4.5. Carbon and Oxygen stable isotope ($\delta^{13}C_{calcite}$ $\delta^{18}O_{calcite}$) results in calcite veins and host rocks associated, expressed in ‰VPDB and ‰VSMOW respectively.

N°	ID samples	Tipology	$\delta^{13}C_{calcit}$ VPDB ‰	$\delta^{18}O_{calcit}$ VSMOW ‰
1	TUF 1.1	Blocky calcite Vein	0.59	23.12
2	TUF 1	Blocky calcite veins	0.62	22.93
3	SEN 2.1	Blocky calcite comb and parallel Veins	1.46	16.38
4	PZZ1	Blocky calcite Comb and Paralell veins	2.36	26.16
5	MCPTA	Blocky calcite comb vein	3.17	35.42
6	T.CAP	Blocky calcite Vein	1.18	24.28
7	PR4N20	Blocky calcite veins	1.85	26.73
8	PR1W3	Blocky calcite veins	1.29	18.08
9	MC3_V1	Blocky Calcite comb veins	2.43	32.50
10	MC3_V2	Fibrous comb calcite veins	2.38	26.58
11	VRD02	Blocky calcite parallel vein	1	27.40
12	VRD1.1	Blocky calcite parallel vein	1.31	27.40
13	VRD2	Blocky calcite parallel vein	2.52	27.66
14	CVR	Blocky calcite Vein	1.42	10.61
15	CVRN30	Blocky calcite vein	1.77	26.35
16	CVR3	Blocky calcite vein	1.87	25.99
17	CP1	Blocky calcite comb and parallel veins	1.15	10.02
18	SEN 2.1.1	Blocky calcite comb and parallel vein	1.46	23.40
1	**TUF_H**	Host rock	0.82	25.97
2	**PZZ3_H**	Host rock	1.91	27.94
3	**T.CAPH**	Host rock	1.29	28.06
4	**PR4N20H**	host rock	1.8	29.24
5	**MC3_H**	host rock	2.78	28.26
6	**CVRH**	host rock	2.25	29.90
7	**CP1H**	host rock	2.06	20.19

The $\delta^{13}C$ values of the studied calcite veins ranges between 0.59 ‰ and 3.17 ‰ and overlap the range of 0.82 – 2.78 measured in the associated host rocks formed by limestone and dolomitic limestone. These isotopic values are comparable with $\delta^{13}C$ values of 2.21 ‰ assumed in the Apennine aquifer from carbonate mineral dissolution (Chiodini et al., 2004).

The stable oxygen isotope composition ($\delta^{18}O$) of calcite depends on the $\delta^{18}O$ values and the temperature of the fluid from which they precipitate (Sharp, 2017). The $\delta^{18}O$ values of the calcite veins vary between 10.02 ‰ and 35.42 ‰. The host rocks show a range of $\delta^{18}O$ values between 20.19 ‰ and 29.90‰. In Figure 4.21 the stable isotope composition ($\delta^{13}C$ and $\delta^{18}O$) of calcite veins along with those of the corresponding host rocks, data from Mesozoic marine carbonates (Sharp, 2007).

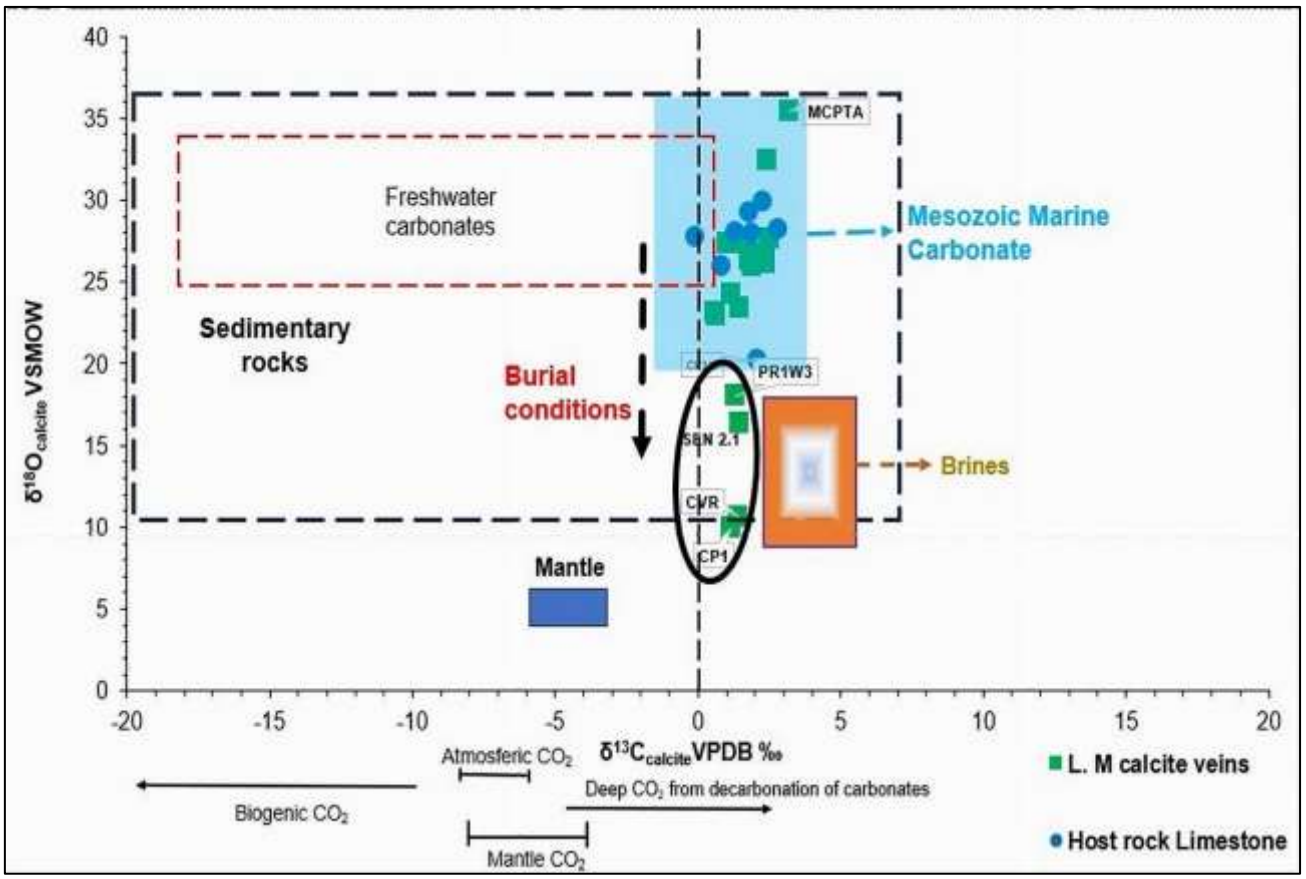

Fig.4.21 *$\delta^{13}C_{calcite}$ and $\delta^{18}O_{calcite}$ calcite veins and carbonate host rock plot. Reference $\delta^{18}O$ (V-SMOW) vs. $\delta^{13}C$ (V-PDB) diagram showing the main isotopic field for representative fluids and rock types. Reference data from: Kirkwood et al. (2001), Sharp (2007), Smeraglia et al. (2018); Curzi et al. (2024).*

The most calcite veins samples show $\delta^{13}C$ and $\delta^{18}O$ values like those of the corresponding host rock which in turn fall in Mesozoic marine carbonate field (Sharp, 2007). Instead, some calcite veins samples showing $\delta^{13}C$ values like other previous calcite veins, are characterized by a marked depletion in $\delta^{18}O$ compared with other samples and Apennine Carbonate Platform. This depletion can be simply explained by a shift from a shallow marine diagenesis (host rock, other samples) towards a deeper one, characterized by burial environment of marine-derived fluids, such as connate fluid trapped within the marine sedimentary succession (carbonate platform deposit).

4.3 FLUID INCLUSION (FIs) WITHIN CALCITE MINERALIZATION VEINS

4.3.1 Petrographic and Micro-thermometry of fluid inclusions

Fluid inclusions (FIs, i.e. small volumes, μm, of paleo-fluids entrapped within host minerals), provide indispensable information about geological processes, such as: temperature, composition and time of fluid entrapment and providing direct information about the conditions at which given minerals and rocks are formed.

Based on the classification (i. e. primary, secondary, pseudosecondary), their characterization reported in *Appendices Ch. 3.1*), the study of their chemical composition with trapping temperature, provides insights into the P-T history of the mineralization veins-related fault systems.

FIs are present in most calcite veins samples studied (e.g. CVR, TUF1.1, MCPTA and MC3_V1 samples). Furthermore, the small size (< 1 μm) of other inclusions in calcites minerals, prevented microthermometric phase analysis and textural study. From the few samples analyzed, FIs were arranged as isolated, small clusters and/or small trails within calcite grains. Some inclusions are arranged in Fluid Inclusion assemblage (FIA), i.e., on petrographically discriminated, cogenic groups of fluid inclusions (Bodnar et al., 2003) and arranged as small cluster and/or isolated inclusions in calcite crystals, suggesting their primary origin (Goldstein, 2003).

In CVR calcite vein sample, the FIs (Fig. 4.22) are organized as isolated inclusions or as small clusters made of 2-10 FIs and have a maximum size between 18 and 25 μm and a volume fraction, ϕ, ranging between 5% and 80%. The FIs are arranged as fluid inclusion assemblage (FIA). Based on petrographic observation we recognized 2 different types of FIs (Fig.4.22):

1) Type I (Fig. 4.22a): primary fluid inclusions arranged along the growth structures. These inclusions are potentially solid inclusions or even biphase (L+V).

2) Type II (Fig.4.22b): bi-phase FI (L+V) arranged as small trails. These inclusions are filling secondary fractures, cutting through the host crystal.

Type I are in Fluid Inclusion Assemblage (FIA), primary FIs, occurs in isolated clusters with 18-20 μm size biphasic, liquid and vapor with a volume fraction, ϕ ~ 30%. Type II are in FIA secondary FIs, occurs in small intragranular trail with 25 μm size biphasic, liquid and vapor with a volume fraction, ϕ 5-10%. Some FIs show textural characteristics of partial decrepitation, and a clearly re-equilibration features such as (i) the presence of outer dark halos around the main cavity, and (ii) the presence of stretched FIs in calcite crystals (Figs. 4.22b).

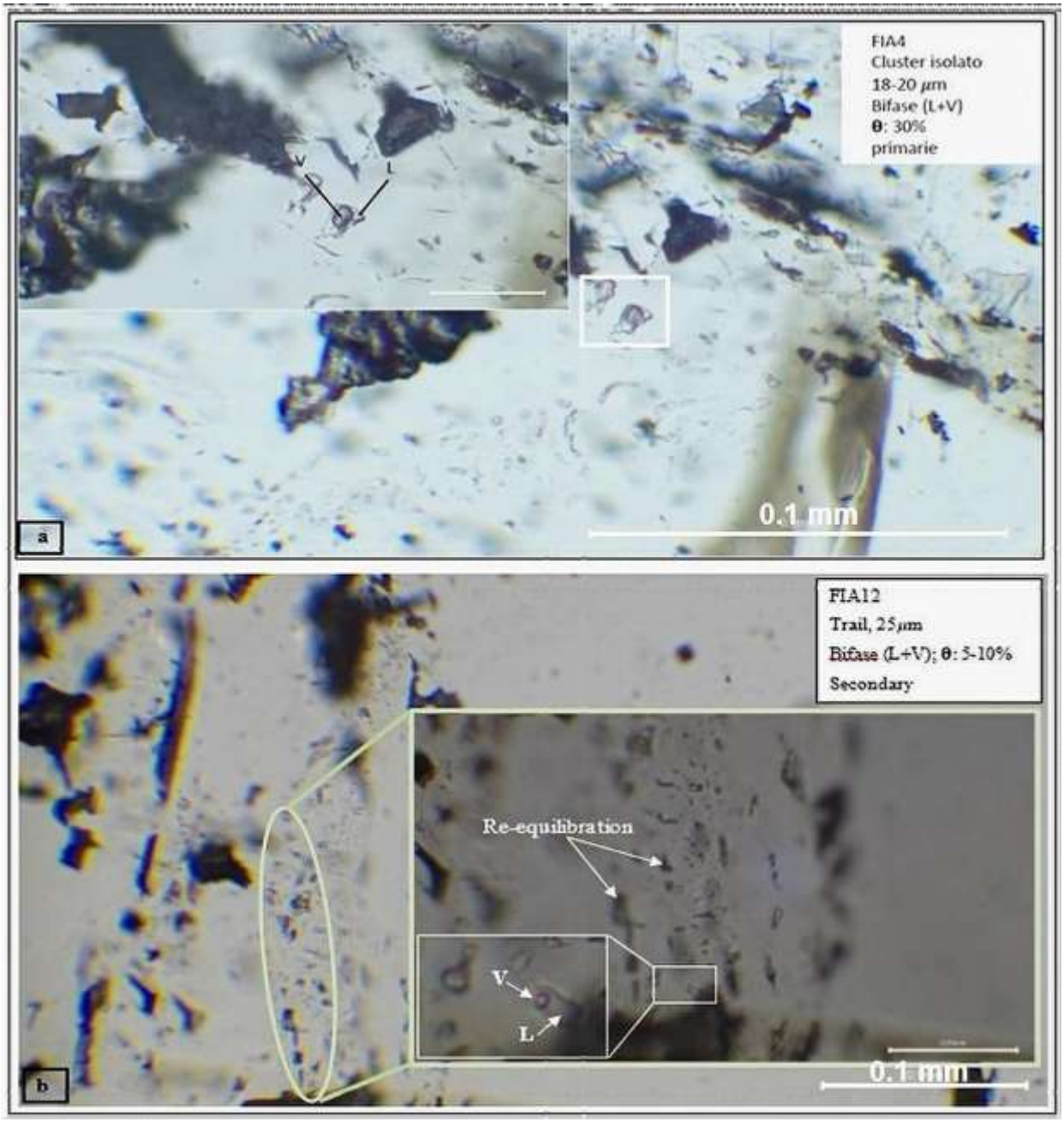

Fig.4.22. *Photomicrographs of petrographic results FIA in CVR sample.* ***(a)*** *Isolated cluster primary FIA;* ***(b)*** *Intergranule Trail in secondary FIA;* ***(c)*** *primary intragranular isolated inclusions in FIA. In b re-equilibration features with the presence of outer dark halos around the main cavity, and (ii) the presence of stretched FIs in calcite crystals*.

In MC3_V1 calcite vein sample (Figs. 4.3, 4.4), the FIs were arranged as small clusters within calcite grains and in small intragranular trails (Fig.4.23).

The FIs (Fig.4.23a) contained a two-phase fluid (liquid and vapour) had a maximum size of 1 - 5 μm with a volume fraction (φ) ranging between 10% and 20%. Figure 4.23 shows a representative Fluid Inclusion assemblage, that is, on petrographically discriminated, cogenic groups of FIs (Bodnar, 2003) found in vein V1 of MC3 sample.

Also, these fluid inclusions are arranged as small cluster and/or isolated inclusions in calcite crystals, suggesting their primary origin (Goldstein, 2003). The partial re-equilibration process of FIs can be show in secondary trail FIA (Figure 4.23b), with the presence of stretched FIs in calcite crystals.

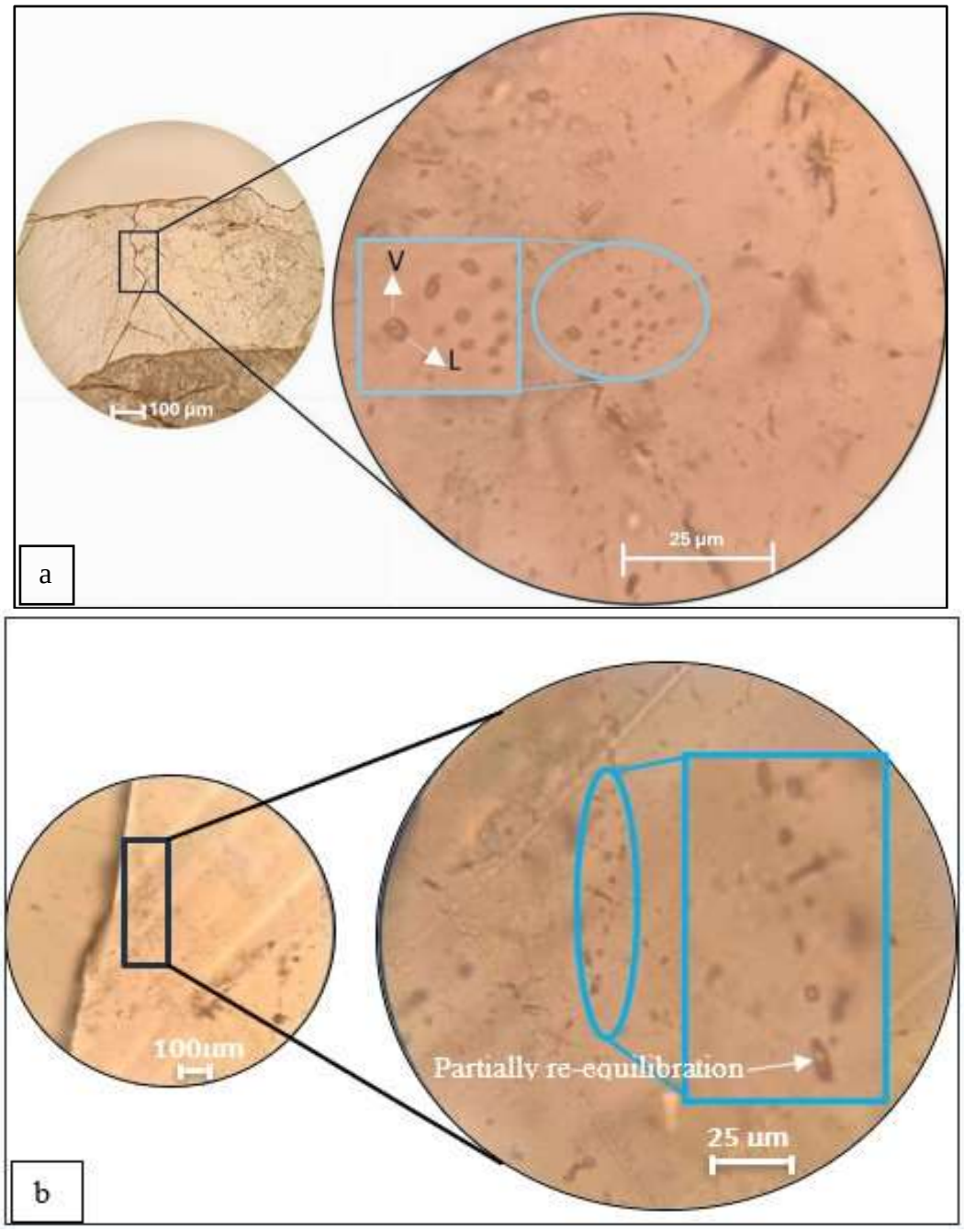

Fig.4.23. *Photomicrographs of petrographic results FIs in MC3_V1 sample.* ***(a)*** *Representative textural distribution (parallel polars) of Fluid Inclusions Assemblage (FIA) trapped in calcite veins (sample MC3_V1) from optical microscopy analyses. L= liquid; V= vapor;* ***(b)*** *Intragranular trail in secondary FIs which can be show a partial re-equilibration process of FIs.*

In TUF 1.1 sample (Figs. 4.24) the FIs were arranged as secondary intragranular trails of FIA (Fig 4.24a) and in primary small cluster (Fig 4.24b). The intragranular trail content ca. 20 FIs, instead the isolated cluster content 5 ca. FIs. All occur with a size ranging from 1 to 5 μm. Their shape is generally irregular, with negative-crystal forms and circle shapes, according to the host mineral. Some FIs show textural characteristics of partial decrepitation, such as haloes of tiny fluid inclusions (diameter < 0.1 μm) surrounding the inclusions cavity, revealing that some events of partial density re-equilibration have occurred (Fig. 4.24a). The FIA arranged as small cluster and/or isolated inclusions in calcite crystals, suggesting their primary origin, instead intragranular trail suggest a secondary origin, as reported by Bodnar (2003), Goldstein, (2003) and Randive et al. (2014).

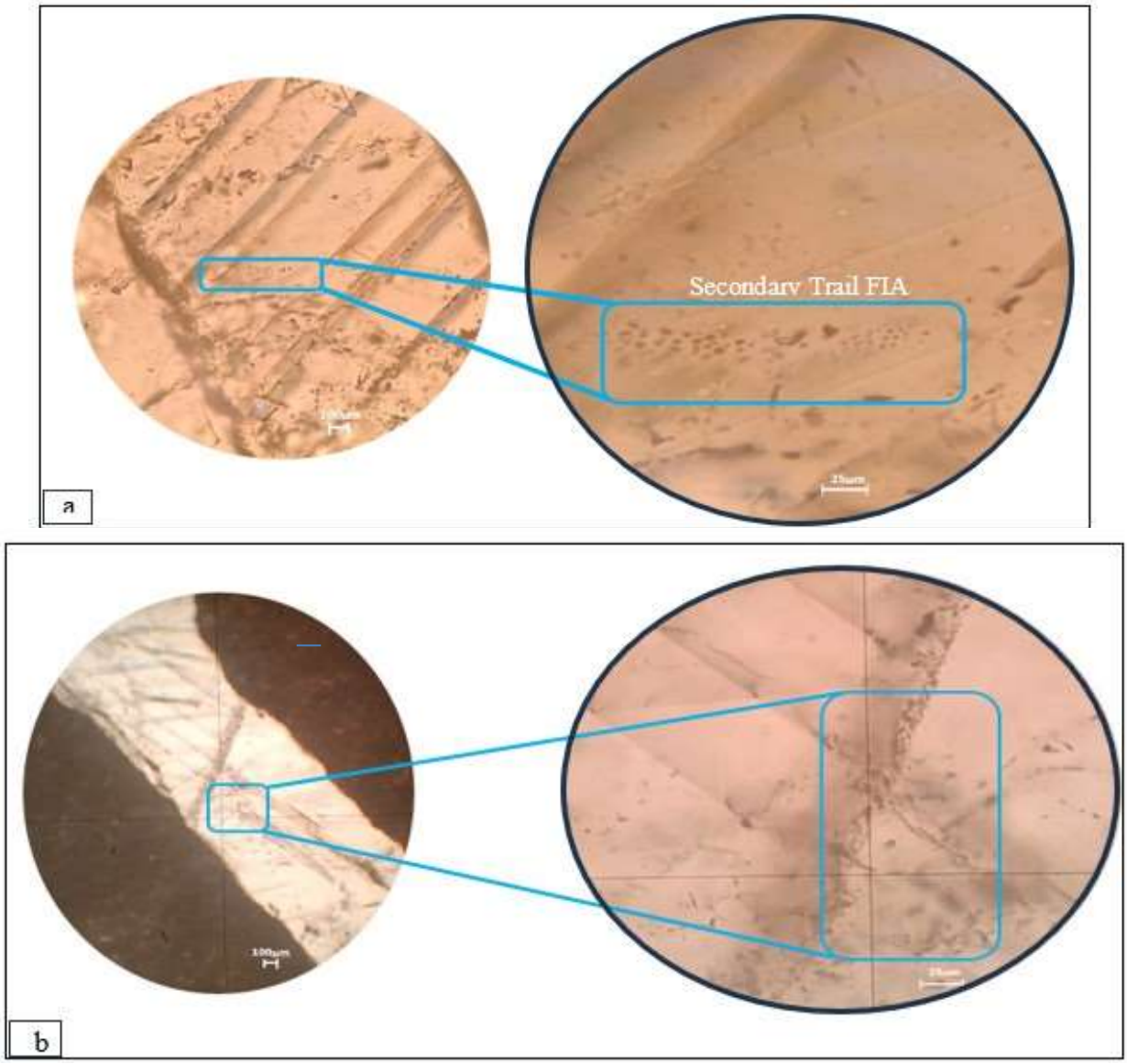

Fig.4.24. *Photomicrographs of petrographic results FIs in TUF 1.1 sample.* ***(a)*** *Intragranular trail in secondary FIA with a probably re-equilibration.;* ***(b)*** *Intragranular cluster in primary FIs.*

In MCPTA calcite vein sample, the FIs were arranged as secondary intragranular trail of FIA (Fig 4.25) contents ca. 15 fluid inclusion with a size ranging from 5 to 15 μm. Their shape is generally irregular, elongated, with negative-crystal forms and rectangle shapes. All show a textural characteristic of total decrepitation, with the presence of stretched FIs in calcite crystals which it is possible evidence of volumetric density re-equilibration at high strain rates associated with a short-time scale event (Bodnar, 2003).

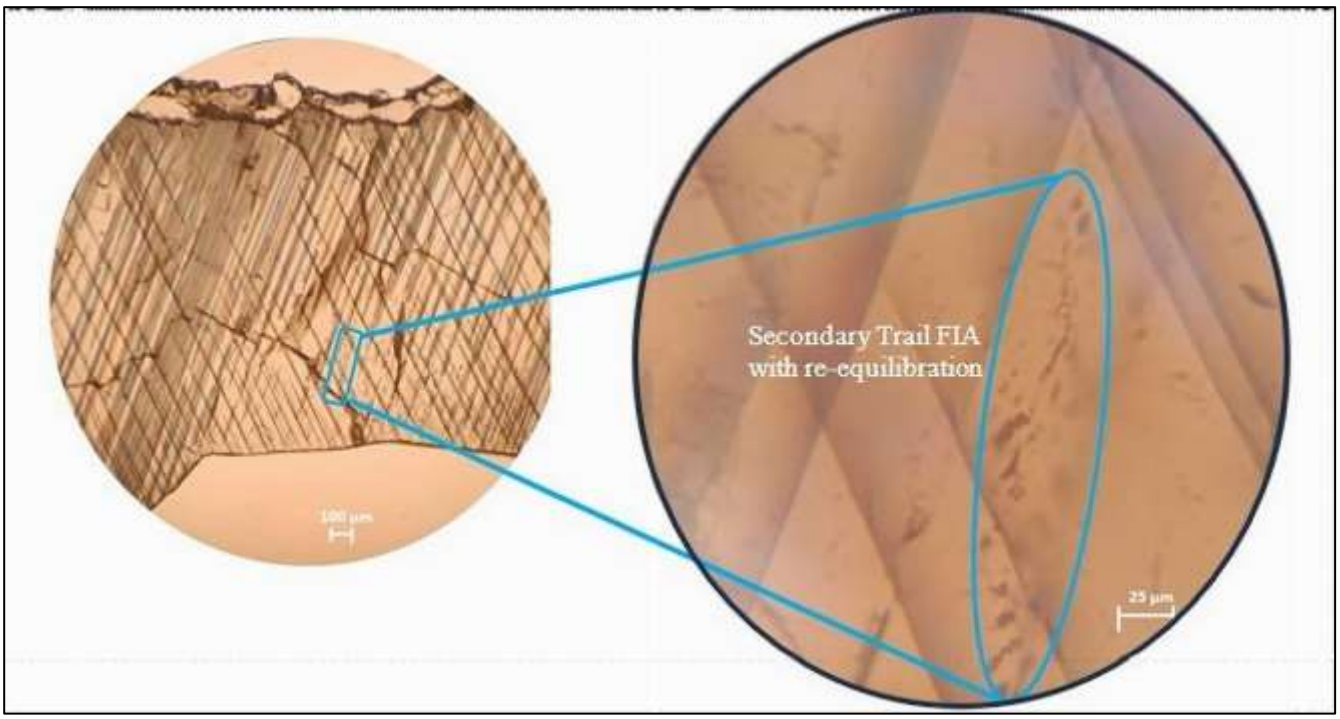

Fig.4.25. Photomicrographs of petrographic results FIs in MCPTA sample. Intragranular trail in secondary FIs with some FIs show textural characteristics of total decrepitation.

In PZZ1 calcite vein sample, the FIs were arranged as isolated within calcite grains (Fig.4.26) suggesting their primary origin (Goldstein, 2003). The isolated FIs, contained a two-phase fluid (liquid and vapour) had a maximum size of 1 - 5 μm with a volume fraction (φ) ranging between 30% and 40%.

4Also, in PZZ1 sample, some FIs show textural characteristics of partial decrepitation, such as haloes of tiny fluid inclusions (diameter < 0.1 μm) surrounding the inclusion cavity, revealing that some events of partial density re-equilibration have occurred. The partial decrepitation process (Figure 4.26), which is evidence of volumetric re-equilibration at high strain rates associated with a short-time scale event (e.g., Bodnar, 2003).

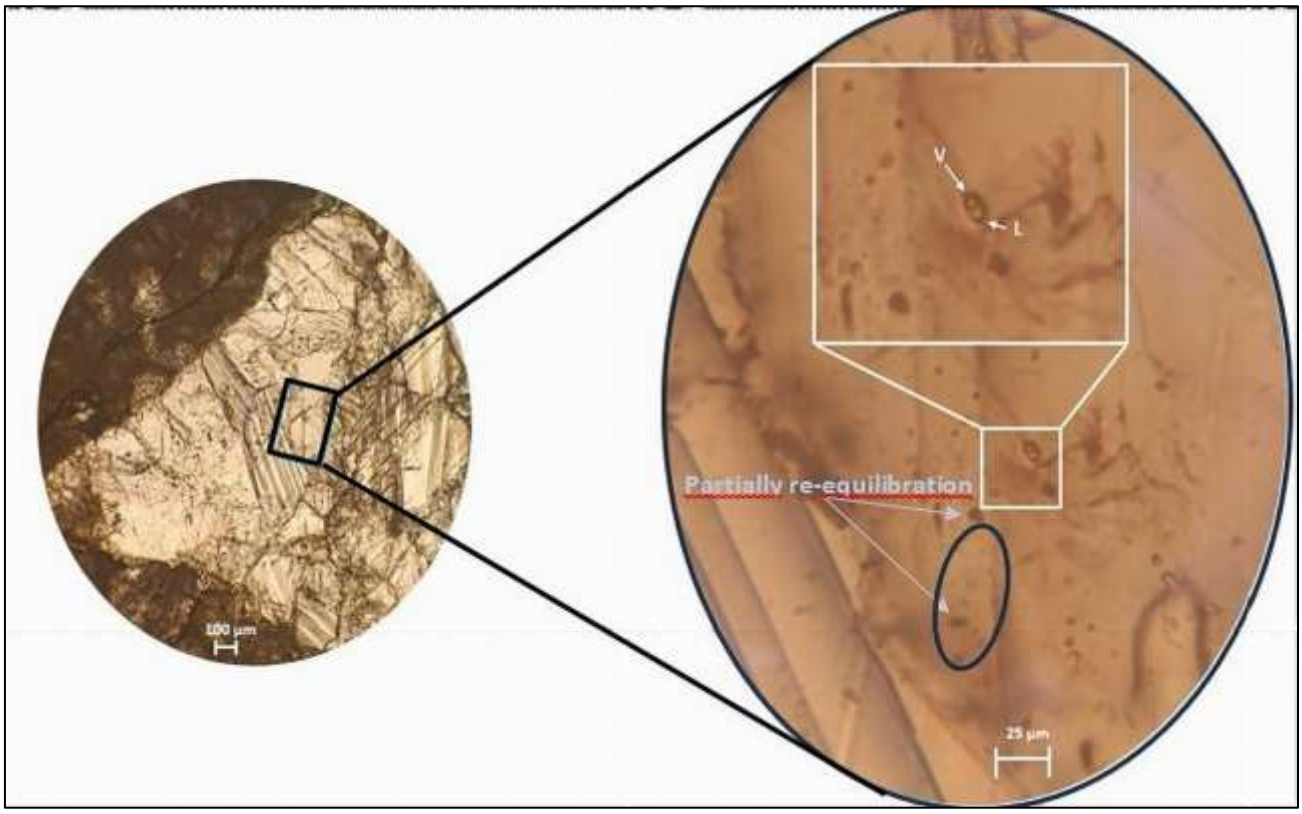

Fig.4.26. *Photomicrographs of petrographic results FIs in PZZ1 sample. Intragranular isolated primary FIs from optical microscopy analyses. L= liquid; V= vapor. In the blue circle you can noted the re-equilibration of some FIs.*

In Table 4.6 the microthermometric results of the best-preserved FIs (CVR, MC3_V1, TUF1.1, MCPTA, PZZ1 samples) are reported. The eutectic behavior and the narrow range of measured Te* suggest the well know binary NaCl-H_2O system (Te = -21.2 °C) as a characterizing chemical system in studied FIs and the slightly lower range may be due to the presence of very low amounts of other volatile species. No CO_2 was detected (the eutectic temperature of pure CO_2 is -56.6 °C). At room temperature the studied fluid inclusions were essentially two phases, liquid and vapour (L + V), commonly liquid rich, or rarely multiphase with the presence of daughter phases (probably hydrohalite, $NaCl \cdot 2H_2O$). With the Te* range and the chemical system in order to calculate the salinity (expressed as wt. % $NaCl_{eq}$) using the NaCl-H_2O phase diagram of the empirical expression given by Bodnar

(1993). Results, show apparent eutectic temperatures ranging from -19.9 to -20.5 °C, although the small dimension of FIs did not allow the correct determination of Te* for almost all inclusions. Considering the very small size of the inclusions, and the numerous fractures in the minerals, it was only possible to calculate the salinity in two samples: CVR and TUF1.1 respectively, that are generally < 5% $NaCl_{eq}$ and in CVR sample varies from 0.44 to 0.62 % $NaCl_{eq}$. In the calcite crystals, FIs are characterized by melting temperatures (Tm, only observed in two samples), with variable homogenization temperatures of the vapour phase to the liquid phase (Th_L). In calcite crystals, Th_L varies from -19.9 to -20.5 °C corresponding to density ranges (ρ) of 0.95- 0.97 g/cm^3 (TUF 1.1 and MC3_V1 sample respectively). In the CVR, the density of FIs sample varies (ρ) = from 0.64 to 0.87 g/cm^3. In Table 4.7 show all studied fluid inclusions homogenize to liquid phase (ThL; L + V = L), with homogenization temperature (t_{hom})ranging from 100 to 324 °C (corresponding to densities of 0.005 and 0.11 g/cm3, respectively) and homogenization pressures (P_{hom}) ranging from 4.5 to 114.8 bar, calculated according to Bodnar (1993), while isochore curves were calculated using the software "FLUIDS" (Bakker, 2003).

Table 4.6 Petrographic-textural results of FIs by Roedder (1984), Bodnar (2003) Goldstein, (2003) and Randive et al. (2014). P=primary; S=secondary; PS= pseudosecondary; FIA= Fluid inclusion assemblage; C=cluster; trail. Salinities (wt. %) and Pressure $_{hom}$ (bar) were calculated according to Bodnar (1993), while isochore curves were calculated using the software "FLUIDS" (Bakker, 2003).

ID Sample	N° FIA	N° inclusion	Type	T_{hom} (°C)	Salinity (wt. % $NaCl_{eq}$)	Dominant phase	Ph (bar)	d (g/cm^3)	isobars (kbar)
CVR	FIA 1	1	P	305.5	0.61	L	88.3	0.68	0,088
	FIA 1	2	P	/	0.61	L	88.3	0.68	0.088
	FIA 1	3	P	312.5	0.61	L	97.5	0.67	0.097
	FIA 2	1	P	298.5	0.52		79.9	0.70	0,079
	FIA 2	2	P	315.5	/	L	101.6	0.66	0.101
	FIA 3	1	P	310.5	0.52	L	94.8	0.67	0.094
	FIA 3	2	P		0.52	/			
	FIA 4	1	P	315.5	/	L			
	FIA 8	1	P	298.5	/	L			
	FIA 9	1	intergranule trail (S)	250.3	0.61	L	35.9	0.80	0.035
	FIA 9	2	intergranule trail (S)	312.5	0.61	L	97.5	0.67	0.097
	FIA 9	3	intergranule trail (S)		0.61				
	FIA 9	4	intergranule trail (S)		0.61				
	FIA 9	5	intergranule trail (S)	199	0.61	L	12.3	0.87	0.012
	FIA 10	1	intergranule trail (S)	307.5	0.52	L	90.9	0.68	0.090
	FIA 10	2	intergranule trail (S)	307.5	0.52	L	90.9	0.68	0.090
	FIA 10	3	intergranule trail (S)	307.5	0.52	L	90.9	0.68	0.090
	FIA 10	4	intergranule trail (S)	307.5	0.52	L	90.9	0.68	0.090
	FIA 10	5	intergranule trail (S)	307.5	0.52	L	90.9	0.68	0.090
	FIA 10	6	intergranule trail (S)	307.5	0.52	L	90.9	0.68	0.090
	FIA 10	7	intergranule trail (S)	307.5	0.52	L	90.9	0.68	0.090
	FIA 10	8	intergranule trail (S)	307.5	0.52	L	90.9	0.68	0.090
	FIA 10	9	intergranule trail (S)	307.5	0.52	L	90.9	0.68	0.090
	FIA 11	1	isolata P	201.4	/	V			
	FIA 12	1	intergranule trail (S)	218.9	0.44	L	19.1	0.84	0.019
	FIA 12	2	intergranule trail (S)	324.6	0.44	L	114.8	0.64	0.114
	FIA 12	3	intergranule trail (S)	228.8	0.44	V	23.6	0.83	0.023
	FIA 12	4	intergranule trail (S)	234.1	0.44	L	26.2	0.82	0.026
	FIA 12	5	intergranule trail (S)	273.8	0.44	L	54.2	0.75	0.054
	FIA 12	6	intergranule trail (S)	273.8	0.44	L	54.2	0.75	0.054
	FIA 12	7	intergranule trail (S)		0.44				
	FIA 12	8	intergranule trail (S)	282.6	0.44	L	62.6	0.73	0.062
	FIA 12	9	intergranule trail (S)	282.6	0.44	L	62.6	0.73	0.062
	FIA 12	10	intergranule trail (S)	278.7	0.44	L	58.8	0.74	0.058
TUF1.1	Cluster 1	1	Cluster (P)	110	<5%	L	4.8	0.95	0.005
		2		110		L			
		3		110		L			
		4		110		L			
	Trail1	1	intergranule trail (S)	120	< 5%	L	4.6	0.96	0.005
		2				L			
		3				L			
		4				L			
		5				L			
		6				L			
		7				L			
MCPTA	Trail 1	1	intergranule trail (S)	100	Not determinate	L	5	0.97	0.005
		2		105		L			
		3				L			
		4				L			
		5				L			
		6				L			
MC3_V1	Trail 1	1	intergranule trail (S)	115	Not determinate	L	4.5	0.95	0.005
		2		125		L			
		3		103		L			
		4		114		L			
		5				L			
	FIA 1	1	P	120		L	4.5	0.95	0.005
		2							
		3							
		4							
		5							
		6							
PZZ1		1	P	130	Not determinate	L	4.6	0.94	0.005
		2	P	140		L			

A sketch showing the complete procedure of cooling and heating analyses of studied fluid inclusions in order to measure apparent eutectic temperature (Te*), and homogenization temperature (Th), is presented (Fig. 4.27).

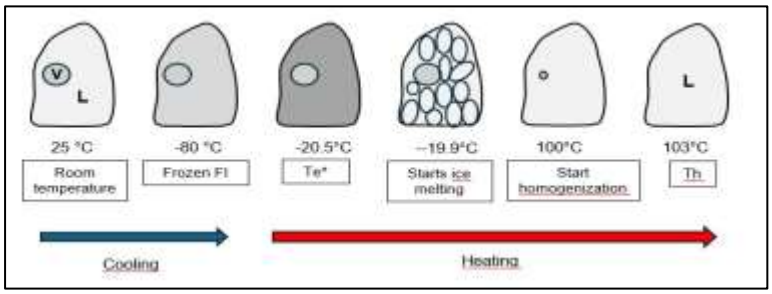

Fig. 4.27. *Sketch showing the phase behaviour of an H2O-NaCl fluid inclusion during a complete procedure of a micro-thermometric analysis. The fluid inclusion is first cooled and then heated in order to observe the phase changes. The sketch shows the example of a studied fluid inclusion.*

Normally, the homogenization temperature is less than the real trapping temperature, although if there is no evidence that fluid inclusions have re-equilibrated and they were trapped in an immiscible fluid system, then the homogenization temperature is equal to the real trapping temperature (Bodnar, 2003). In this case a pressure correction (the difference between homogenization temperature and estimated trapping temperature of the fluid inclusions) must be added to the measured homogenization temperatures to obtain the trapping temperatures. Indeed, our study shows no evidence of immiscible fluid system with the presence of some fluid inclusions with partial decrepitation and re-equilibration processes. In order to estimate a pressure correction, it is necessary to determine the slope of the isochores along which the fluid inclusions were trapped.

In Figure 4.28 the results of the equation described in the fluid inclusion technique of Bodnar and Vityk (1994), with the relationship between trapping temperature and pressure, salinity (about 0.5 wt % NaCleq in our case) and homogenization temperatures are reported. The slope of the iso-Th lines (≅ isochores) for NaCl-H_2O solutions with salinity of 0 wt. % and homogenization temperatures ranging from 50 to 800 °C, with an upper limit of 6 kbar are shown. To resume, micro-thermometric studies on Irpinian calcite veins (Fig.4.28) shows the presence of a very low salinity (≅ 0.5 wt. % NaCleq) and a two families of fluid temperatures: one in green with temperatures between 100 and 140 °C and one in orange 200 and 324 °C.

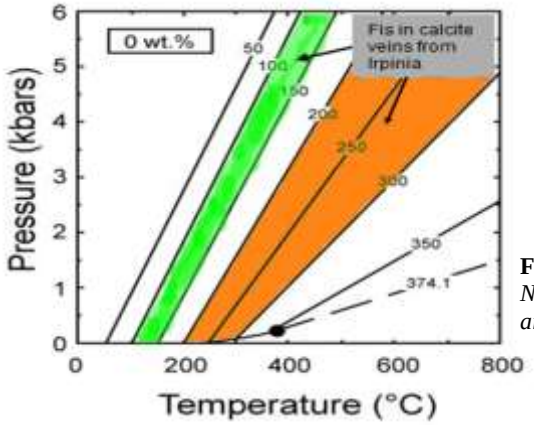

Fig.4.28 *Iso-Th curves for NaCl-H2O inclusions having salinity of 0 wt.% NaCl. Th-Ph ranges of studied fluid inclusions depicted in green and orange area.*

4.3.2 Noble gases in FIs

The primary sources of fluids are in the mantle, crust and atmosphere. Since noble gases are not reactive, the origin of He in natural fluids can be traced by using their isotopic signature (e.g. Ozima and Podosek, 2002).

The calcite vein samples were analyzed also to determine the concentrations and isotopic compositions of the light noble gases He, Ne, Ar in FIs and also their isotope ratios ($^3He/^4He$, $^4He/^{20}Ne$ and $^{40}Ar/^{36}Ar$) (Table 4.7).

The ^4He, ^{20}Ne and ^{40}Ar concentrations were 8.80×10^{-14}–1.31×10^{-11}, 1.39×10^{-14}–1.61×10^{-13} and 8.11×10^{-12}–9.84×10^{-11} mol g^{-1}, respectively. The He isotope ratios ($^3He/^4He$) were normalized to the value in air (where Ra is the atmospheric ratio of 1.38×10^{-6}; Mabry et al., 2013), yielding values ranging from 0.08 Ra (TUF 1.1b sample) to 1.38 Ra (vein V2 in MC3 sample). The $^4He/^{20}Ne$ ratios ranged from 1 (PR1W3a sample) to 81.7 (TUF 1.1 sample). These values were higher than those found in both atmosphere and air-saturated water (ASW), at 0.319 and 0.285, respectively, at 25°C (Ozima and Podosek, 2002). The $^{40}Ar/^{36}Ar$ ratio varied from 302.2 (CVR3 sample) to 404.6 (vein V2 in MC3 sample), and hence was slightly higher than that in the atmosphere (298.6; Lee et al., 2006), which is consistent with an excess of no atmosphere-derived ^{40}Ar. We computed the concentration of deep-sourced ^{40}Ar (due to ^{40}K decay in the mantle and/or in the crust) using the following equation 15 reported by Graham (2002). The computed $^{40}Ar^*$ concentration ranged from 2.76×10^{-13} to 6.04×10^{-12} mol g^{-1}, while the $^{40}Ar^*/^4He$ ratio varied from 0.19 to 36.74.

Considering that ^3He was 1.17×10^{-18} to 1.49×10^{-18} mol g^{-1}, ^4He was 7.81×10^{-13} to 7.77×10^{-13} mol g^{-1}, $^{40}Ar/^{36}Ar$ was 316.3 to 404.6 and $^{40}Ar^*$ was 1.91×10^{-12} to 7.38×10^{-12} mol g^{-1} at the Monte Castello fault site, a marked difference was found between potentially post-kinematic blocky calcite (vein V1 in MC3 sample) and potentially syn-kinematic fibrous calcite (vein V2 in MC3 sample) in terms of both R/Ra (where R is the He isotopic signature of the sample) and $^{40}Ar/^{36}Ar$ (Table 4.8). Vein V2 (1.38 Ra, $^{40}Ar/^{36}Ar$ = 404.6 and $^{40}Ar^*$ = 1.91×10^{-12} mol g^{-1}) exhibited higher values than vein V1 (1.07 Ra, $^{40}Ar/^{36}Ar$ = 316.3 and $^{40}Ar^*$ = 7.38×10^{-12} mol g^{-1}), indicating a mantle He component.

Table 4.7 Chemical compositions of noble gases (He, Ne and Ar) and their isotopic ratios in fluid inclusions trapped in calcite veins associated with seismogenic faults. Note: unit of error is in %

ID Sample	^4He mol/g	^4He err (%)	^3He mol/g	^3He err (%)	^{20}Ne mol/g	^{20}Ne err (%)	^{40}Ar mol/g	^{40}Ar err (%)	He/Ne	R/Ra	Rc/Ra	Err tot +/-	$^{40}Ar/^{36}Ar$	$^{38}Ar/^{36}Ar$
PR1w3(a)	8.80E-14	0.10	7.84E-20	20.02	8.44E-14	0.90	4.13E-11	0.09	1.0	0.64	0.61	0.13	321.8	0.18657
PR1w3(a)	1.72E-13	0.09	1.91E-19	19.09	8.99E-14	0.59	4.29E-11	0.11	1.9	0.80	0.82	0.15	318.3	0.18625
VRD02	7.16E-13	0.12	7.06E-19	5.42	5.61E-14	1.00	3.43E-11	0.10	12.8	0.71	0.71	0.04	315.8	0.18489
MC3_V1	7.81E-13	0.03	1.17E-18	4.20	7.00E-14	0.60	3.07E-11	0.13	11.2	1.07	1.09	0.05	316.3	0.18611
CVR3	2.73E-13	0.03	4.13E-19	5.90	1.39E-14	0.66	8.11E-12	0.07	19.6	1.09	1.09	0.06	307.0	0.18662
CVR4	1.96E-12	0.02	2.92E-18	2.45	4.34E-14	0.94	1.74E-11	0.07	45.3	1.07	1.07	0.03	303.1	0.18622
MC3_V2	7.77E-13	0.02	1.49E-18	2.97	5.52E-14	0.51	2.77E-11	0.06	14.1	1.38	1.40	0.04	404.6	0.18618
MCPTA	8.18E-13	0.03	8.41E-19	3.60	2.34E-14	0.52	2.06E-11	0.06	34.9	0.74	0.74	0.03	383.3	0.18713
T.CAP	2.84E-12	0.02	2.09E-18	2.86	4.27E-14	0.46	3.03E-11	0.11	66.5	0.53	0.53	0.02	315.6	0.18721
TUF 1.1	1.31E-11	0.02	2.05E-18	3.02	1.61E-13	0.63	9.43E-11	0.06	81.7	0.11	0.11	0.00	320.6	0.18740
TUF 1.1b	1.28E-11	0.02	1.56E-18	3.02	1.72E-13	0.67	9.84E-11	0.07	74.4	0.09	0.08	0.00	316.0	0.18641
SEN 2.1	1.09E-12	0.02	8.48E-19	3.91	2.48E-14	0.50	1.62E-11	0.06	44.0	0.56	0.56	0.02	303.2	0.18726

4.3.3 Deuterium isotopic composition and water content (H_2O wt.%) in FIs

The FIs within calcite veins samples, were analyzed also to determine the H_2O concentration trapped in the inclusions and deuterium isotopic composition. The H_2O concentration within the inclusions expressed in % and δD-H_2O was reported in the conventional δ notations in VSMOW with an analytical error of ± 2‰. The concentration of H_2O, δD-H_2O in fluid inclusions and $\delta^{18}O_{parentalfluids}$ values were reported in Table 4.8.

The measured D/H ratios in FI show a wide range of values with δD spanning from -106.2 (MC3_V2 sample) to -2 ‰ (CP1 sample), the percentage of H_2O trapped in the inclusions is in the range 0.2– 1.4%.

The stable isotopic compositions (δD and $\delta^{18}O_{parentalfluids}$) in FI of the studied samples was compared with those of waters (groundwater and thermal water) of Contursi Hydrothermal basin (Gori et al., 2023), Figure 4.29. The studied FIs show a positive isotopic $\delta^{18}O$ shift compared with Contursi groundwater values, up +25‰. This ^{18}O enrichment is due to possible greater oxygen exchange between fluid and carbonate host rocks occurred for long time and/or in a burial environment.

Table 4.8. The concentration of H_2O (%), δD-H_2O (VSMOW ‰) of fluid inclusion and $\delta^{18}O_{parental\ fluids}$ (VSMOW ‰). The parental fluids $\delta^{18}O_{fluids}$ calculated by $\delta^{18}O$calcite through the relationships by O'Neil et al. (1969) and Kim and O'Neil (1997).

Sample	δD_{H2O} VSmow ‰	H_2O %	$\delta^{18}O_{parental\ fluids}$ VSmow ‰
TUF 1.1	-85.5	0.3	9.09
TUF 1	-75.8	0.3	9.49
SEN 2.1	-33.8	0.4	2.35
PZZ1	-34.1	0.6	13.86
MC3_V1	-41.7	1	19.06
MC3_V2	-2	1.1	
MCPTA	-69.7	0.6	19.52
VRD1.1	-76.2	0.5	
CVR	-26.8	1.4	4.92
CVR3	-26.9	1.2	
CP1	-106.2	0.2	

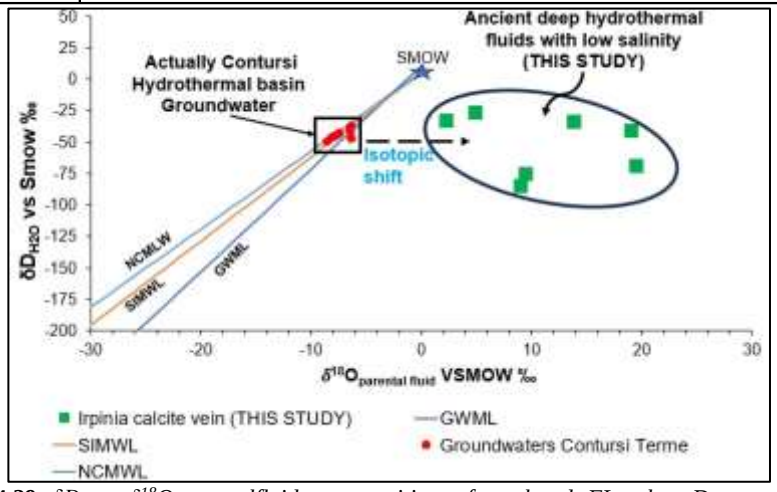

Fig.4.29 *δD vs $\delta^{18}O$parentalfluids composition of analyzed FIs plot. Data reference of groundwaters, NCMLW, SIMWL and GWML by. Gori et al. (2023 and reference therein).*

Chapter 5 – Discussion

5.1 VEINING PROCESSES

The study area lies in the axial zone of the southern Apennines (Fig.3.1), whose uplift and exhumation started during Middle-Upper Pleistocene due to extensional faulting rooted at depths down to ca. 15 km (Figs. 3.1, 5.1a). The greatest amount of crustal stretching associated to normal faulting occurs along the NE-SW direction, with a computed slip-rate of 3-5 mm/y (Ascione et al., 2013). According to this well-documented tectonic setting of the Irpinia region of southern Italy, we now discuss the modalities of formation of the studied fault-related vein systems on the basis of the existing literature (Hancock and Barka, 1987; Stewart and Hancock, 1990; Smeraglia et al., 2018; Curzi et al., 2024).The two main fault-related, calcite vein sets documented it in the studied area are comb fractures (C-veins) and slip-parallel fractures (SP-veins) shown in Figure 5.1b.

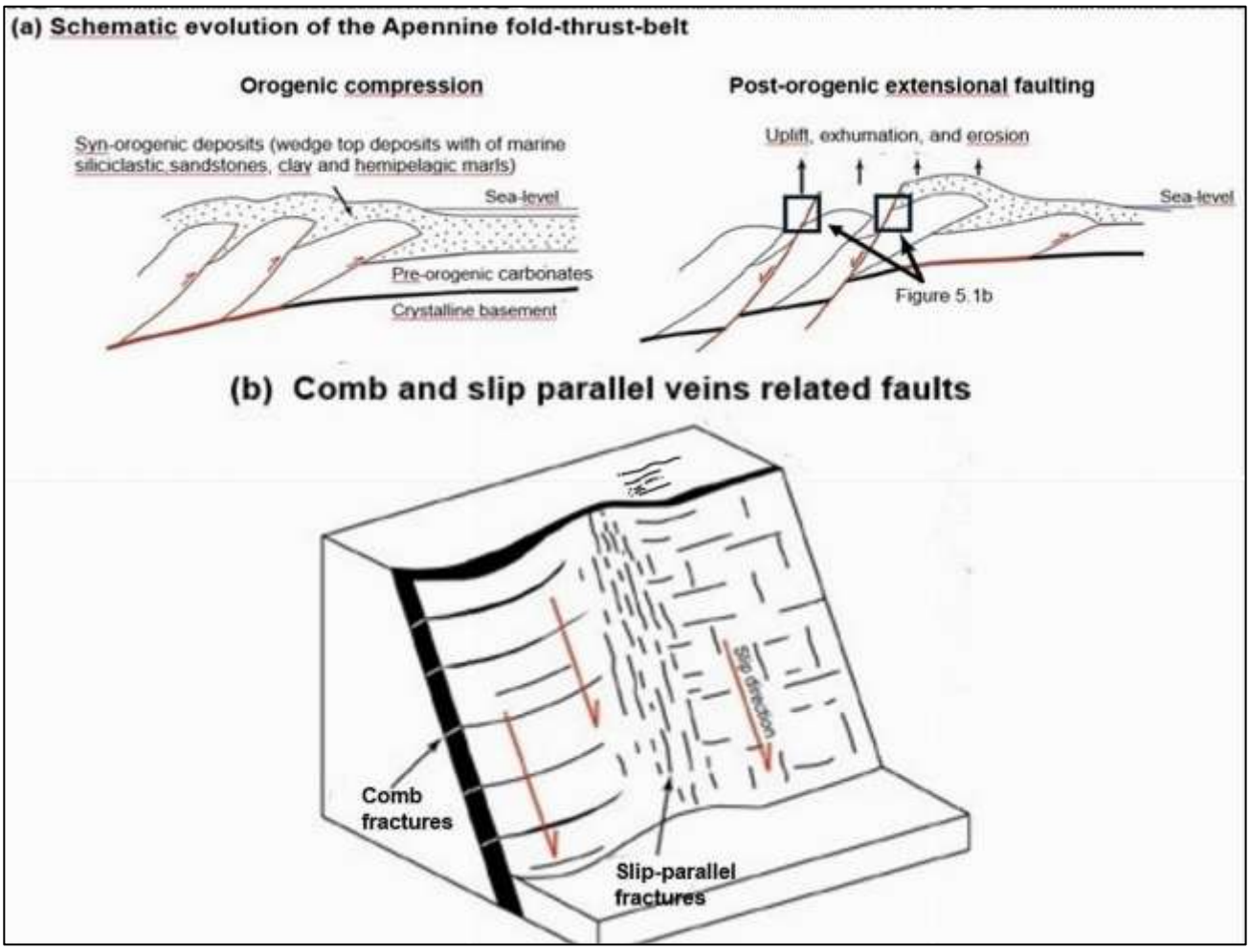

Fig.5.1 ***(a)*** *Cartoon showing the conceptual model for the evolution of a Burial-exhumation history of the Apennines belt involving compression and post-collisional extension with normal faults (with extensional stress regime), modified after Smeraglia et al., 2018.* ***(b)*** *Conceptual cartoon showing comb and slip-parallel fractures/veins commonly developed along active extensional faults due to co-seismic stress release (modified after Stewart and Hancock, 1990). Schmidt net, for attitude and slip vectors of the Contursi hydrothermal basin and surrounding area of Irpinia for principal surface and poles to comb and slip-parallel veins.*

The intersection of C-veins and SP-veins with the individual fault planes forms lineations respectively at high angles (45-90°) and low angles (0-45°) with respect to the slip direction. Such a structural configuration is somehow similar to those reported from the active extensional faults of central-southern Apennines (e.g., Smeraglia et al., 2018; Curzi et al., 2024; Schirrippa Spagnolo et al., 2024). In places, C-and SP veins are up to a few cm-thick and show apparent components of either normal or reverse offset. In this context, C-and SP veins are interpreted as structural elements linked to stick-slip displacement episodes and/or multiple displacement increments during slip along extensional fault planes (Hancock and Barka, 1987; Stewart and Hancock, 1990), or as due to tear affects related to the gravitational collapse of the hanging wall block along the fault planes and consequent pull of the footwall block (Doglioni et al., 2013). A recent work proposed that both comb and slip-parallel veins might also form during co-seismic displacement of the footwall block, and coeval stress release associated to the ingress and flow of fluids (Smeraglia et al., 2018).

The slight discrepancy with theoretical angles documented for both C-and SP-veins and the slip vector (Fig. 5.1b) can be interpreted as due to variation of the fault slip direction over time. We note that the attitude of C-veins, and their relations with the slip vector, is somehow compatible with the present-day extensional stress regime (Mariucci and Montone, 2020). Furthermore, these veins are not cur or displaced by structure associated with orogenic compressional phases, reinforcing their association with the post-orogenic extensional phase.

Independently of the sampling sites, host rock lithology and fault-strike directions, most of the studied calcite veins included ***blocky*** texture of crystals (e.g. Figs. 4.3, 4.16a, 4.18). Despite the crosscutting relations and vein dip angles, the mineral precipitation post-dated the occurrence of brittle fracturing. This texture is commonly associated with precipitation in phreatic conditions, as recently documented by Manniello et al. (2023) and Todaro et al. (2024) for the Lower Jurassic carbonates exposed in the nearby area of Monte di Viggiano (southern Italy).

The rapid fracture opening, possibly mediated by fluid overpressure, and later precipitation in a fluid-saturated open space likely occurred in the study rock (Curzi et al., 2024). In fact, irregular branching of blocky vein networks enclosing host rock fragments pointed to a mineralization from overpressured fluids (Bons et al., 2012). Crosscutting relationships and the incorporation of antitaxial vein fragments, into blocky veins indicate repeated fracturing. In only two cases MC3_V2 and MCPTA_V3 samples (Figs. 4.3 and 4.16a, b) we found a ***fibrous*** texture of calcite crystals that were formed by progressive small increments of opening shearing and mineral precipitation in a potentially co-seismic phase (Passchier and Trouw, 2005). Most calcite blocky crystals are affected by the twinning process (thin and thick twinning), can be used an indicator of strain direction, intensity and temperature of deformation (Ferrill et al., 2024).

This “dynamic” method has been modified and refined in order to determine the principal directions and/or magnitudes of either (palaeo) stress or strain. The appearance of calcite twin lamellae changes systematically as a function of deformation temperature (Burkhard, 1993). Ferrill et al. (2004) correlated, mean width of twin lamellae

with the temperature of deformation (Fig. 2.4 in Appendices 1.1). Based on the textural calcite veins by microstructural results obtained and shown for example in figure 4.3a, b; 4.14b and 4.16a, it is probable a weak to moderate intracrystalline deformation of calcite is assumed to have occurred late tectonic events, with a temperature range of 150 to 250°C.

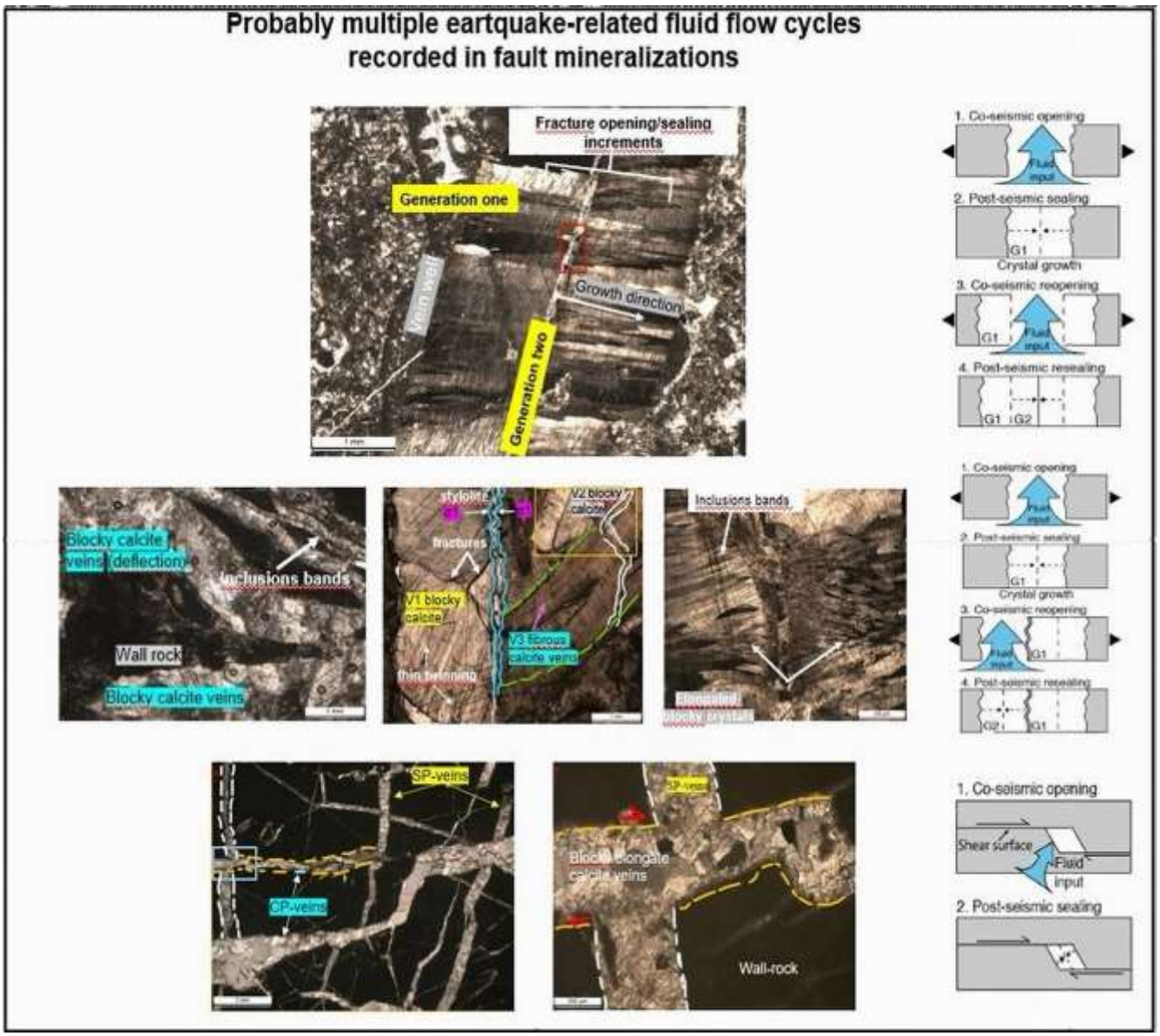

Fig.5.2 *Schematic illustration of possible multiple earthquake-related fluid flow cycles preserved within fault-related mineralization microstructures (veins). In particular, the illustration shows temporal relationships between multiple episodes of fracture opening and sealing. G1 and G2 denote the earliest cements precipitated following consecutive fracture opening, and therefore record the approximate timing of co-seismic fracture opening (modified after Williams et al., 2017; Smeraglia et al., 2018).*

Pre-existing extensional fractures/veins can be reactivated potentially by further co-seismic stress release episodes as shear veins that offset the fault surface (Stewart and Hancock, 1990). Episodic displacements and/or multiple stick-slip episodes are consistent with the crack-and-seal textures observed within fault-related mineralizations along the Contursi basin and surrounding area (Figs. 4.10, 4.13). In particular, each crack-and-seal event implies the crack opening, blocky to elongated-blocky crystals precipitation from advective flow in a fluid-filled open crack (Hilgers et al., 2004), and consequential crack sealing (Fig.5.2). In this studied cases, new cracking events occurred only after the complete sealing of fractures, as shown by well-developed wall rock inclusions bands (Fig. 5.2; e.g., Williams et al., 2017 and Smeraglia et al., 2018). The studied C- and SP-Veins, are characterized by variable sizes of the incremental crack and seal growth (up to 5-6 mm for a single crack event; Figs. 4.10, 4.13) within the same vein. Smeraglia et al., 2018 proposed that these variable sizes are consistent with different slip increment magnitudes or different fault slip styles, including slow, fast and intermediate slip rates. It is speculated that, in the case of the southern Apennines, the different sizes of incremental crack and seal growth in C-, SP-veins may account for small-to-large slip events recorded along extensional faults by crack episodes of different magnitudes. This incremental growth may, in particular, be consistent with the recent extensional seismic sequence that lasted for months-to years with tens of thousands of earthquakes of various magnitudes of 1694 and 1980 Irpinia-Lucania seismic sequence (Bello et al., 2021). This hypothesis was also considered in the recent earthquakes occurred in central Italy (Colfiorito 1997, L'Aquila 2009, and Amatrice-Norcia 2016 sequences) by Smeraglia et al. (2018). In this regard, considering the impermeable horizon (Irpinia Melange, Fig. 3.1b) that lies in between the deep Apulian carbonates and the shallower Apennine Platform might be overpressurized (Hager et al., 2021), the fault zone that eventually dissect can cat as fluid conduit (Caine et al., 1996; Faulkner et al., 2010) causing possible fault-valve actions (Sibson, 2000; Doglioni et al., 2013) and causing earthquakes in tectonically active regions (Miller et al., 2004). Furthermore, a previous study by Amoroso et al. (2017 and reference therein) supports the evidence for a fluid-saturated fracture system in the carbonate rock volumes underneath the 1980 Irpinia earthquake epicentral area, about 1 to 5 km from the study area. A recent work by Schirripa Spagnolo (2024) indicates that the sealing properties of this Irpinia melange were likely enhanced locally by increased thickness but were also compromised by fault activity and associated seismic events.

5.2 FLUID SOURCES

To characterize the fluid source, responsible for the $CaCO_3$ precipitation (veins), it is necessary to define the exact temperature and the O isotope composition of the parental fluids. As above reported, micro-thermometric results on studied FIs within calcite veins show the presence of a very low salinity (≅ 0.5 wt. % NaCleq) and a two fluid types with different temperatures values: the first with temperatures between 100 and 130 °C and the second one in the range of 200 and 324 °C.

In this context, from the $\delta^{18}O$ values in the calcite veins (Table 4.5), it's possible determine the oxygen isotopic

compositions of the vein-forming fluids ($\delta^{18}O_{Parentalfluids}$) using the empirical equation (O'Neil et al., 1969; Kim and O'Neil, 1997) for water temperatures between 0 to 500 °C, under the assumption of isotopic equilibrium:

$$\delta^{18}O_{fluid} = \delta^{18}O_{CaCo3} - 1000\ln \alpha$$

$$1000\ln\alpha \text{ (calcite-}H_2O) = 18.03\ (10^3\ T^{-1}) - 32.42$$

Where T is expressed in K, calculated by microtermometric analysis of FIs, reported in Table 5.1.

Table 5.1 Parental oxygen stable isotope ($\delta^{18}O_{Parentalfluid}$) results from the $\delta^{18}O_{calcite}$ expressed in ‰ VSMOW, calculate by isotopic equilibrium (O'Neil et al., 1969; Kim and O'Neil, 1997).

ID samples	$\delta^{18}O_{calcit}$ VSMOW ‰	$\delta^{13}C_{calcit}$ VPDB ‰	T_{hom}(°C) FIs	T_{hom} (°k) FIs	1000lnα	$\delta^{18}O_{fluids}$ SMOW ‰
TUF 1.1	23.12	0.59	115	388.15	14.03	9.09
TUF 1	22.93	0.62	120	393.15	13.44	9.49
MCPTA	35.42	3.17	100	373.15	15.90	19.52
MC3_V1	32.5	2.43	120	393.15	13.44	19.06
SEN 2.1	16.38	1.46	115	388.15	14.03	2.35
PZZ1	26.16	2.36	130	403.15	12.30	13.86
CVR	10.61	1.42	320	593.15	-2.02	12.63
CVR	10.61	1.42	200	473.15	5.69	4.92

The calculated $\delta^{18}O_{parentalfluids}$ together to data of homogenization temperatures of paleofluids, allow to define two different groups of paleofluids circulating in studied fault zones (Fig 5.3):

Group 1: It is characterized by $\delta^{18}O_{parentalfluids}$ values between 9.09 to 19.52 ‰ with temperature values in the range 100 – 130 °C and low salinity (< 5 wt. % NaCl). For these fluids a wide range of oxygen isotope values is observed, demonstrating a low fluid/rock ratio, or a long-term fluid-host rock interaction with higher fluid/rock ratio (Sharp, 2017). The homogenization temperatures of 100 – 130°C of this group are similar to the maximum burial temperature experienced by the Apennine Carbonate Platform host rock (100 – 120 °C; Aldega et al., 2003; Corrado et al., 2005), except for PZZ1 sample having value of temperature (130°C) probably due a mixing of different fluid endmember.

The only SEN 2.1 sample has a $\delta^{18}O_{parentalfluid}$ value of 2.35 ‰ and a temperature value of 115 °C (Fig. 5.3), that is lower than other samples. Since these high temperatures are apparently at odds with the relatively low $\delta^{18}O$ values, this can be interpreted as due to the mixing of warm fluids (T > 100 °C) with colder one (i.e. infiltrated meteoric and/or shallow water). Similar considerations are proposed by Schirippa Spagnolo et al. (2024) in the Val D'Agri basin and by Smeraglia et al. (2018), Curzi et al. (2024) in central Italy.

Group 2: It is characterized by $\delta^{18}O_{parentalfluids}$ values between 4.92 to 12.63 ‰ with temperature values from 200 °C to 324 °C and low salinity (0.4 – 0.6 wt. % NaCl).

The precipitate temperatures are significantly higher than maximum burial temperature experienced by the

Apennine Carbonate Platform and Lagonegro basin host rock (100-120° and 140-160°, respectively, estimated by the thermal modelling of Aldega et al., 2003 and Corrado et al., 2005). As above reported for the sample group 1 samples the difference in $\delta^{18}O$ is linked to a wide variability in water-rock interaction.

Summarizing, parental fluids of group 1 which allows the precipitation of calcite, are in thermal equilibrium with respect to the maximum burial temperatures of the Apennine Carbonate Platform. The source of this group 1 includes deep crustal fluid mixed with meteoric and/or shallow water component in thermal equilibrium with the host rock (Apennine Carbonate Platform) uprising in surface. In contrast, the high temperatures of fluid group 2 require a source deeper than Apennine Carbonate Platform. By assuming a geothermal gradient ~ 30 °C/km (Boncio et al 2007) and a surface temperature of groundwaters ranging between 7 ° and 47 °C (Gori et al., 2023), the homogenization temperatures from group 1 are consist with an origin of parental fluids from reservoir with depths of 3 ~ 4 km. This corresponds to the burial depths of the Mesozoic carbonate tectonic unit both during orogenic and post-orogenic phases. In contrast, the high homogenization temperatures of paleofluid of group 2, in disequilibrium with Apennine Carbonate Platform, require a deeper source at depths of about 8~10 km, where the Apulian Carbonate Platform is located (Amoroso et al., 2017 and reference therein). These crustal deep fluids probably uprising in surface, after crossing the impermeable horizon (Irpinia Tectonic mélange) caused by probable strong earthquakes as noted in High Agri Valley (southern Italy) by Schirippa Spagnolo et al. (2024).

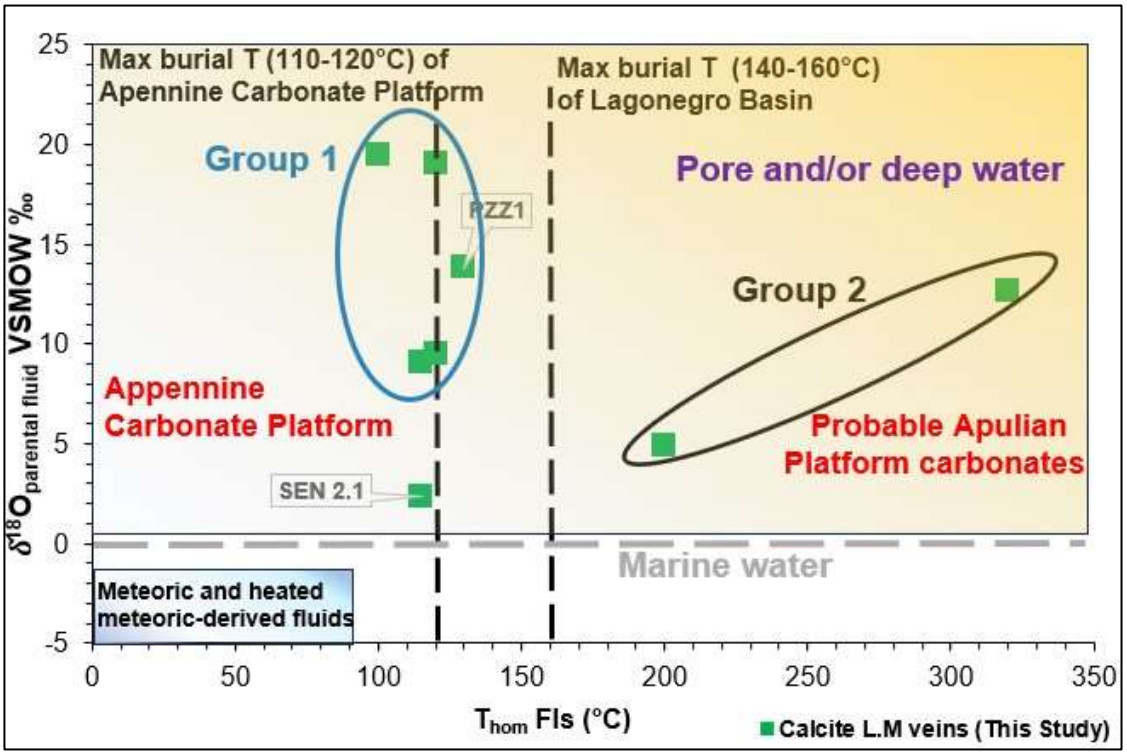

Fig. 5.3 *$\delta^{18}O_{parentalfluid}$ VSMOW (‰) vs T_{hom} (°C) of FIs plot. Only SEN 2.1 and PZZ1 samples are in thermal and isotopic disequilibrium with Apennine carbonate platform host rock. Reference: different types of waters by Curzi et al. (2024 and reference therein); in dashed black line the maximum burial temperatures (°C) of Apennine carbonate platform and Lagonegro basin unit by Aldega et al. (2003), Corrado et al. (2005), Schirripa Spagnolo et al. (2024).*

These interpretations are also supported by REE-Y concentration pattern that is between Apennine carbonate and Apulian carbonate platforms (Rosatelli et al., 2023). All samples of calcite veins show a relative HREE enrichment respect to the crustal standard. Such enrichment is comparable to that of seawater sediments which is commonly associated to the REE complexation by CO_3^{2-} and/or other dissolved ligands (Pipar and Bau. 2013). Furthermore, all studied samples are characterized by LREE depletion (La_{PAAS}/Yb_{PAAS} = 0.27 – 0.48; Nd_{PAAS}/Yb_{PAAS} = 0.3 – 0.89), negative Ce anomaly (Ce/Ce* = 0.18 – 1) typically observed in marine carbonates. The high Sr concentrations (up 272 ppm in calcite veins and 386 ppm in carbonate host rock, Table 4.2), indicate a probable fluid-rock interaction (shallow and depth levels) and a local marine carbonate imprinting preserved by the paleofluids. This fluid-rock interaction is also consistent with the REE+Y concentrations of the studied samples, which are in the range of those of marine carbonates in southern Apennines (Rosatelli et al., 2023).

5.2.2 – Noble gas in FIs

In the analysis of the fault rocks and fault-related fractures exhumed from greater depths, the dilution of deep-seated fluids with the local groundwaters might mask the original isotopic signature of formed fluids. In fact, the reactive volatilies (e.g. CO_2), dissolved in water are speciated (e.g. carbonate equilibrium), and their concentration and isotopic composition are modified by water-gas-rock interaction processes and solute precipitation (Gilfillan et al., 2009; Buttitta et al., 2023). In this regard, noble gases, chemically inert elements, are excellent tracers of both fluid sources and physical processes within the crust (Caracausi and Paternoster, 2015; Curzi et al., 2022; Kendrick and Burnard, 2013; Pik and Marty, 2009).

The primary sources of fluids are in the mantle, crust and atmosphere. Since noble gases are not reactive, the origin of He in natural fluids can be traced by using their isotopic signature (e.g. Ozima and Podosek, 2022). A useful approach for discriminating the He origin is to obtain the values for three possible endmembers by using binary mixing equations (Fig. 5.5) combining the He isotopic ratio (R/Ra) and the $^4He/^{20}Ne$ ratio of three endmembers (Sano et al., 1987). Specifically, here we assume a mantle endmember as the Sub Continental Lithospheric Mantle (SCLM) whose R/Ra is 6.1 ± 0.9 (mean ± 0.9) and $^4He/^{20}He \geq 1000$ (Gautheron et al., 2005; Sano and Marty, 1995; Gibson et al., 2024). The crustal endmember has a R/Ra of 0.02 and $^4He/^{20}Ne \geq 1000$ (Sano and Marty, 1995), for atmosphere (air) R/Ra is 1, and $^4He/^{20}Ne$ is 0.319 (Ozima and Podosek, 2002) and ASW has an R/Ra of 1 and $^4He/^{20}Ne$ 0.285 at 25 °C (Ozima and Podosek, 2022).

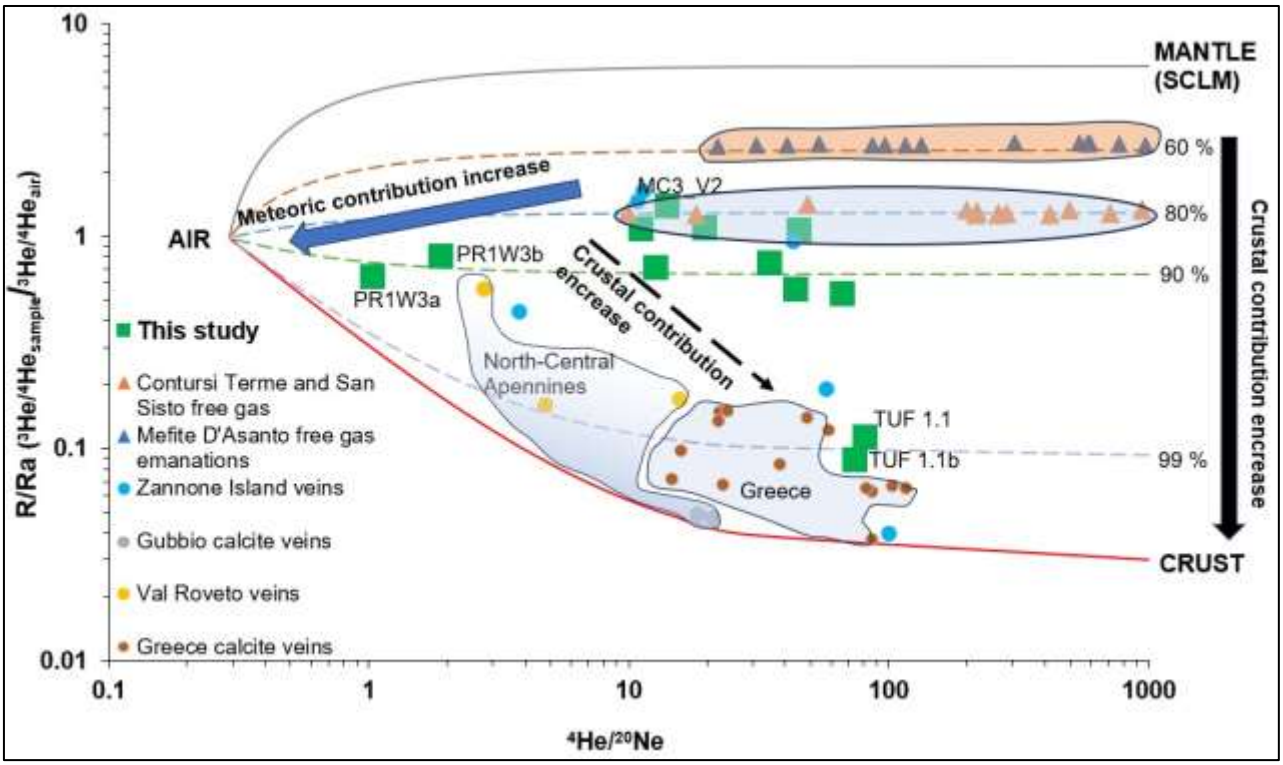

Fig. 5.4. *Diagram of the correlation between the $^{3}He/^{4}He$ and $^{4}He/^{20}Ne$ ratios for the FIs in calcite veins. Solid lines depict binary mixing between air ($^{3}He/^{4}He$=1 Ra, $^{4}He/^{20}Ne$=0.319; Ozima and Podosek, 2002), the Sub Continental Lithospheric Mantle ($^{3}He/^{4}He$=6.1 ± 0.9 Ra, Gibson et al., 2024; $^{4}He/^{20}Ne$ > 1000, Sano and Marty, 1995), crustal endmember ($^{3}He/^{4}He$=0.01–0.05 Ra, $^{4}He/^{20}Ne$ > 1000; Sano and Marty, 1995). Reference data: Contursi free gas data (Buttitta et al., 2023; Caracausi and Paternoster, 2015), Zannone island veins (Curzi et al., 2022), Gubbio calcite veins (Marchesini et al., 2022), Val Roveto veins (Smeraglia et al., 2018), Mefite D'Ansanto free gas (Caracausi and Paternoster, 2015), and calcite fault zone in Greece (Pink and Marty, 2009).*

Most of the investigated FIs trapped calcite vein, from shallow depth fluids-derived (group 1), show $^{4}He/^{20}Ne$ value two-three orders magnitude higher than in atmosphere, which is consistent with a local and negligible amount of atmospheric He (Fig. 5.4). Both samples PR1W3a and PR1W3b are characterized by the low $^{4}He/^{20}Ne$ ratios of 1.0 and 1.9 respectively, and a He isotopic signature ranging from 0.64 to 0.80 Ra, and hence the atmospheric He component could mask the original paleofluids signature. Figure 5.4 shows that most of the investigated samples has R/Ra values between 0.53 and 1.38 Ra, and consistent with a 10-20 % of the mantle-derived He (considering SCLM) and 80-90 % of crust-derived He. Only the TUF1.1a and TUF1.1b samples, collected from the Tufaro thermal area, show relatively pure crustal-derived He, with negligible amounts of atmospheric and mantle He. The highest He isotopic signature in FIs (1.38 Ra of MC3_V2 sample) fits well with data pertaining to the presence of high-flux CO_2 gas emission in the area (Buttitta et al., 2023; Caracausi and Paternoster, 2015; Fig 5.4). This similarity indicates that the ratio of crust-to-mantle He in FIs remained approximately constant over time along the studied faults. The age of the calcite veins is still unknown, and it could provide new constrains on the timing of mantle He degassing in this area of southern Italy.

The large variability of He isotopic signature documented for the studied FIs (R/Ra = 0.09 – 1.38) is not consistent with that documented for the current outgassing that characterizes the study area (Fig.5.4), which show a narrower range of values (R/Ra = 1.27 – 1.41, $^{4}He/^{20}Ne > 3$; Buttitta et al., 2023 and reference therein). In fact, it is noted that to 20 years of low-frequency geochemical monitoring of the Contursi hydrothermal basin has revealed a 0.2 Ra variability of the He isotopic signature of the currently outgassing fluids (Buttitta et al., 2023 and reference therein). During this time span, the background seismicity of the area has recorded seismic events with magnitudes Mw < 4 (http://isnet-bulletin.fisica.unina.it/cgi-bin/isnet-events/isnet.cgi). This means that the background seismicity has not induced any short-term variation in the He isotopic signature (Caracausi et al., 2022 and reference therein).

The large variability of He isotopic signature in FIs can be explained by "early trapping processes" (Zummo et al., 2024), in which the rock fracturing potentially during earthquakes, increased the amount of crustal 4He within the circulating palaeofluids (Caracausi et al., 2022). The "early-trapping" hypothesis suggests that the mineralizing fault fluids captured the ^{4}He released by the fractured and fragmented host rocks due to localized dilatancy of these rocks (Caracausi et al., 2022). However, a "post-trapping processes" due to addition of radiogenic He produced within veins over time (vein ageing) can be invoked. The "post-trapping" hypothesis is based on the production of ^{4}He by the decay of U and Th within the calcite minerals, and on its successive migration towards the FIs (Ballantine and Burnard, 2022). Considering that all studied veins are made up of calcite minerals, and that concentration of both U and Th are ≤ 1ppm, (Table 4.2), it is possible to calculate the production of ^{4}He over time. Further details on the applied equation and the related calculations are given in Appendices 2.5. The amount of He produced from 1 gram of calcite, which is approximately 6.66×10^{-18} moles/yr, allows to define ^{4}He produced from calcite at 0.1 Ma has been totally transferred to the FIs (Table 5.2).

Table 5.2: ^{4}He production over different times assumed that the U and Th concentrations were close to 1 ppm in calcite (Ballantine and Burnard, 2002).

^{4}He atoms g^{-1} yr^{-1}	Years	^{4}He mol/gr y^{-1}
4.01E+06	1E+00	6.66E-18
	1E+01	6.66E-17
	1E+02	6.66E-16
	1E+03	6.66E-15
	1E+04	6.66E-14
	1E+05	6.66E-13
	1E+06	6.66E-12
	1E+07	6.66E-11

We note that the Tufaro Terme samples (TUF 1.1 and TUF 1.1b) exhibited a dominant ^{4}He component (R/Ra = 0.09 – 0.11), similar to those measured in calcite veins of the northern-central Apennines of Italy (Marchesini et al., 2022; Smeraglia et al., 2018), and Greece (Pik and Marty, 2009). The latter data could hence result from the occurrence of both post and early trapping processes over different time periods (Fig.5.4).

Furthermore, the signature of atmospheric fluids was assessed for the studied calcite veins by also considering the Ar isotopes (Table 4.7). Since both ^{3}He and ^{36}Ar are not radiogenic, and their ratio in pure ASW is 5×10^{-8} (Kendrick and Burnard, 2013 and references therein), the $^{3}He/^{36}Ar$ and $^{40}Ar/^{36}Ar$ ratios documented for the Contursi FIs can help in identifying possible atmospheric inputs. Although the $^{40}Ar/^{36}Ar$ ratios (up to 404, Table 4.7) were close to the atmosphere signature (298.6; Lee et al., 2006), their $^{3}He/^{36}Ar$ ratios were up to three orders of magnitude higher than in the atmosphere (Kendrick and Burnard, 2013). Combining the two aforementioned ratios, $^{3}He/^{36}Ar$ vs $^{40}Ar/^{36}Ar$ (Fig. 5.5), we assess that an atmosphere-derived component was mixed with deeper sourced components.

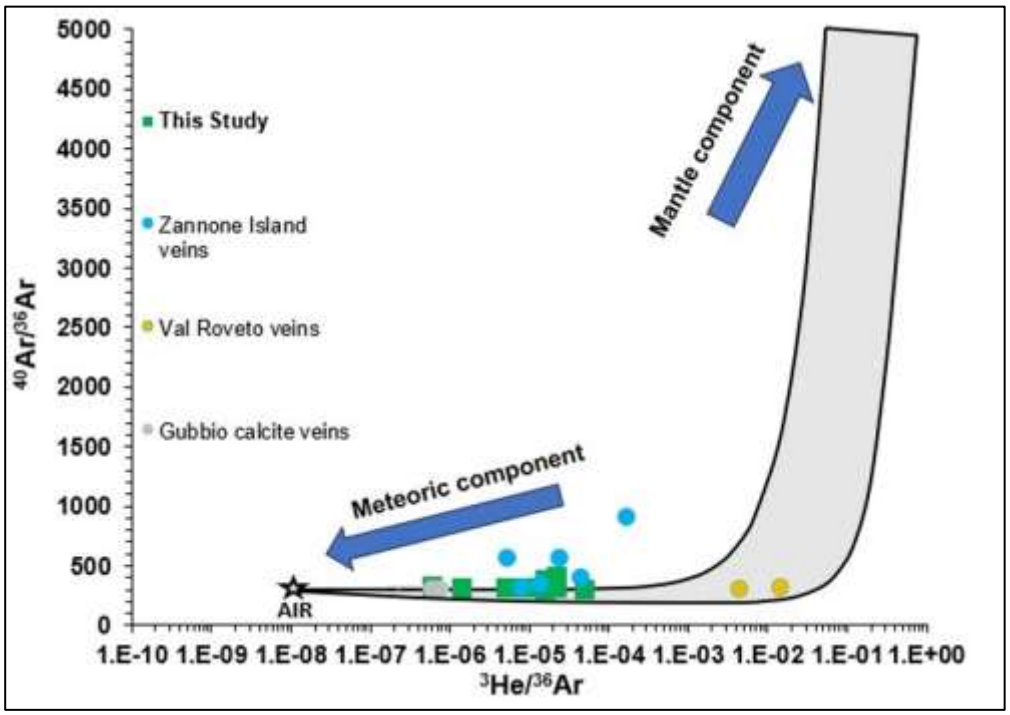

Figure 5.5 *Plot of $^{3}He/^{36}Ar$ versus $^{40}Ar/^{36}Ar$. The grey region is consistent with mixing between mantle-magmatic fluids that are enriched in ^{40}Ar and ^{3}He and a fluid with air or air saturated water (ASW) black star: $^{3}He/^{36}Ar = 1 \times 10^{-8}$ and $^{40}Ar/^{36}Ar = 296.6$; Kendrick and Burnard, 2013). The grey shading indicates literature data that are representative of mixing (Kendrick and Burnard, 2013 and references therein; Tang et al., 2017; Goodwin et al., 2017; Wu et al., 2018)*

This interpretation is supported by the relation between R/Ra and $^{40}Ar/^{36}Ar$ (Fig. 5.6), which shows that the fluids trapped in FIs included an atmospheric component mixed with fluids characterized by a dominant crustal component. Such an interpretation agrees with the data produced by Curzi et al. (2022) for the high-angle fault zones of the Zannone island, along the Tyrrhenian coastline of Italy.

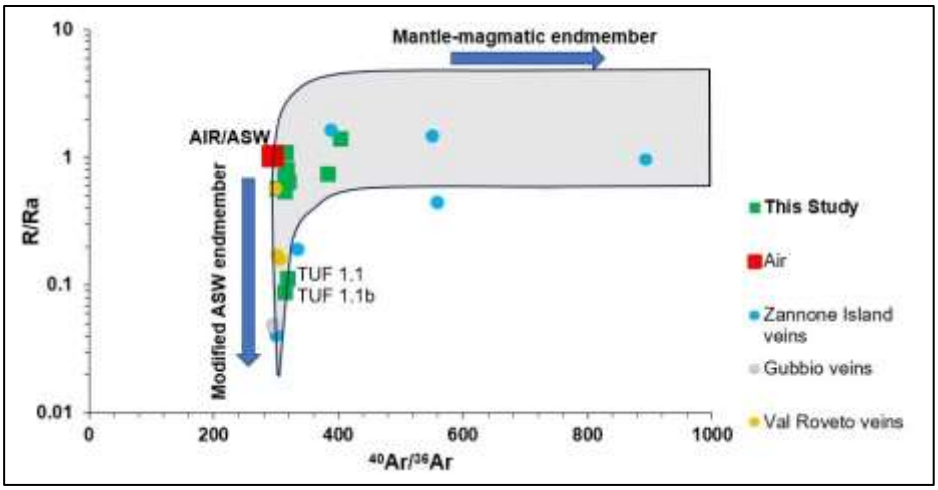

Fig. 5.6. *Schematic of He and Ar isotopes of FIs in calcite. The grey shading indicates data from previous investigations of FIs with both magmatic and crustal origins in various worldwide ore deposits (literature data in Fig.5.5). The red rectangle represents the air and ASW end member. The modified air endmember is ASW that is simply enriched by the addition of radiogenic ^{4}He (Kendrick and Burnard, 2013 and reference therein).*

In contrast, the TUF samples showed a dominant crustal component with modified ASW end-members, referring to fluids that partially preserved the ASW signature but were modified during crustal residence (Kendrick and Burnard, 2013 and references therein). In fact, the He isotope system is more likely modifiable than heavier noble gases due to the very low abundance of He isotopes in ASW. Finally, in absence of a preferential He leakage by diffusion and advection, the ratio between radiogenic crustal ^{4}He and $^{40}Ar^{*}$ is expected to be like the crustal production ($^{40}Ar^{*}/^{4}He \sim 0.1 – 0.2$; Kendrick and Burnard, 2013). Alternatively, the $^{40}Ar^{*}/^{4}He$ can derive from mantle production ($^{40}Ar^{*}/^{4}He \sim 0.1 – 1$; Curzi et al., 2022 and references therein). Considering the original data obtained for the study area (Fig. 5.7), with the calcite veins showing higher values of the $^{4}He/^{40}Ar$ ratio with respect to the crustal production, it can be assumed that a significant mantle contribution is present in the study FIs. It is therefore possible to hypothesize that significant crustal-derived He loss does not affect the isotopic composition of the same elements (e.g. $^{3}He/^{4}He$ and $^{40}Ar/^{36}Ar$).

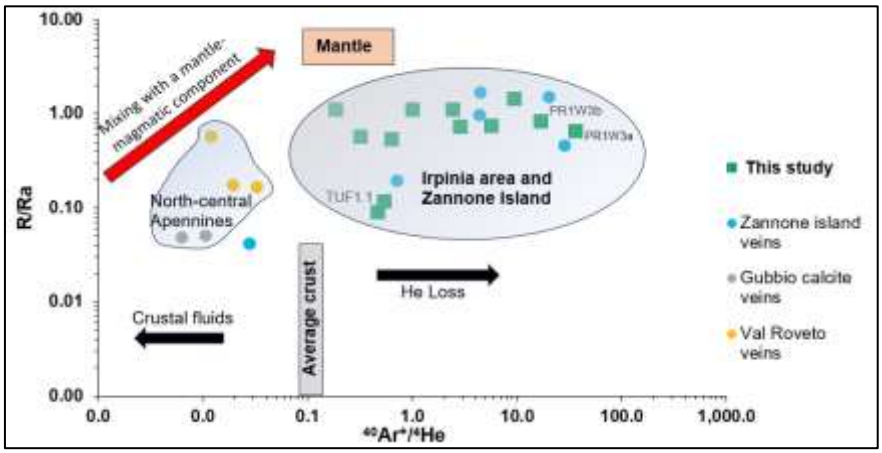

Fig. 5.7 *Plot of $^{40}Ar^{*}/^{4}He$ versus $^{3}He/^{4}He$ (as R/Ra). The compositions of the following two fields are from Kendrick and Burnard (2013): (1) average crust, (2) mantle. Red arrow shading indicate mixing between the crustal and mantle-magmatic fluids.*

Summarizing, the noble gases (He, Ne, Ar) in the fluid inclusions (FIs) trapped in the calcite veins sampled along high-angle fault zones of the Contursi hydrothermal basin, indicate that most of the studied samples are characterized by a noble gases isotopic signature consistent with the mixing of volatiles derived from both crustal and mantle sources with a negligible atmospheric component. The variability of the He isotopic signature in the FIs (three of 10 FIs are out of the mixing trend) can be mainly due to early trapping processes (probably earthquakes occurred in the past). Regarding the outliers, sample PR1W3 showed an atmospheric component possibly masking the original He signature, sample TUF1.1 displayed a very negligible mantle contribution and a dominant crustal contribution, and sample MC3_V2 shown the highest He isotopic signature in the FIs (1.38 Ra). The latest He isotope values revealed mantle contribution up to 20% of the total He component and fits well with the 1.41Ra of the currently high flux CO2 gaseous emission, indicating that the pristine mantle contribution did not vary over time (Zummo et al., 2024).

5.3 CRUSTAL-SCALE CONCEPTUAL MODEL OF FLUID CIRCULATION THROUGH SEISMIC EXTENTIONAL FAULT OF THE IRPINIA AREA (SOUTHERN ITALY)

The Contursi hydrothermal basin is characterized by a high seismogenic potential (Slejko et al., 1998) and currently background seismicity (Mw < 4). This basin is between 1 and 5 km far from the epicentral area of the Mw.6.9 Irpinia earthquake (November 1980, Bernard & Zollo, 1989). As reported by geophysical studies and continuous seismicity monitoring conducted in the study area (Amoroso et al., 2017; De Landro et al., 2022), the Vp/Vs and Vp*Vs changes are located at depths of 1-5 km and 8-12 km (Fig 5.8a). The shallower rock volume, which is encompassed between the Apennines carbonate and the tectonic mélange, is characterized by a pronounced fracture permeability and fluid saturation at hydrostatic pressure conditions. The deeper volume is located beneath the tectonic mélange, which is invoked as the main structural seal for overpressured fluids located within the Apulian carbonate (Impronta et al., 2014; Amoroso et al., 2014), and in deeper volumes of other seismogenic zones of the southern Apennines chain (Chiodini et al., 2004, 2020). The aforementioned scientific articles proposed that the seismic velocity changes in the shallower volume (1-5 km) are caused by meteoric water recharge processes, while in the deeper volume (8-12 km) by pore pressure pulsations.

Based on this consideration, understanding the main sources of paleofluids responsible for the $CaCO_3$ precipitation within the studied fault-related veins, it is possible to propose a general model of fault-related fluid circulation in the Contursi Hydrothermal basin (Fig 5.8b). The main reservoir of the paleofluids was located in the Apulian Carbonate platform, from which the deep crust fluids characterized by a not negligible mantle component ascended towards a shallower crustal depth (1-5 km). There, the deeper-derived paleofluids mixed and interacted with meteoric and/or shallow fluids in both thermal and isotopic equilibrium with Appenine Carbonate Platform. The latter paleofluids precipitate calcite veins reporting: a) $\delta^{13}C$ and $\delta^{18}O$ values similar to those of the Appenine

carbonates; b) variability of the He isotopic ratios with crustal and mantle (up to 20%) component; and c) homogenization temperatures of FIs (between 100 and 130°C) similar to the maximum burial temperature experienced by the Apennine carbonates attesting to a more intense and long-lasting interaction between paleofluids and carbonate host rock.

Differently, other calcite veins and associated FIs are characterized by a marked depletion in $\delta^{18}O$ and higher homogenization temperatures (between 200 and 320 °C). These data are consistent with a burial environment from marine-derived fluids (i. e., connate fluids). These paleofluids ascendent from the deep reservoir (depth greater than 7 km), formed by the Apulian carbonates, and infiltrated the shallower carbonates forming a thermal and disequilibrium with these rocks. It has been noted that large earthquakes can rupture impermeable horizons (i. e. Irpinia tectonic Melange) allowing the release and rising to the surface of overpressured deep crustal fluid in recent work (Schirippa Spagnolo et al., 2024). As reported by Smeraglia et al. (2018 and reference therein), during strong earthquakes, the co-seismic dilatancy (i. e fracture opening) promoted the upward squeezing of overpressured deep fluid along the main slip surfaces of single faults. Sudden fluid depressurization and ascent, coupled with seismic shaking, could foster rapid CO_2 degassing causing carbonate oversaturation and consequent calcite precipitation into co-seismic Comb and Slip-Parallel (C and SP, respectively) fractures. This model is consistent with isotopic and structural-microstructural data of the thesis and with the "early trapping" hypothesis for He isotopic signal measured in FIs. The "early-trapping" hypothesis suggests that the mineralizing fault-related fluids captured the ^4He released by the fractured and fragmented host rocks due to dilatancy of these rocks (Caracausi et al., 2022; Zummo et al., 2024). The dilatancy could occur during the preparatory phase of main earthquakes (foreshock events), producing the release of crustal ^4He (Bauer et al., 2016; Honda et al., 1992) into atmosphere due to volumetric stress changes (Ballantine and Burnard, 2022; Caracausi et al., 2022). The early-trapping hypothesis is supported by the high degree of fracturing documented for most of the studied calcite veins (Chapter 4.1). If so, the pronounced release of ^4He from the fault-related fractured and fragmented rock volumes could be associated with the main shocks that occurred in the studied area (i.e. Mw.6.9 Irpinia earthquake), and likely with the main previous high-magnitude earthquakes (Mw > 6) that have devastated the study area in the last 0.5 ka (Bello et al., 2021). Consequently, the conceptual model points out to the direct link between seismicity and the impulsive nature of crustal ^4He degassing (Caracausi et al., 2022; Buttitta et al., 2020) as already documented by Sano et al. (1998, 2016) through the increase of crustal ^4He in natural fluids during strong earthquakes in Japan (such as the Mw = 7.3 of Kumamoto earthquake, and Mw = 7.2 of Kobe earthquake, respectively in 2016 and 1995). Furthermore, it is noted that to 20 years of low-frequency geochemical monitoring of the Contursi hydrothermal basin has revealed a 0.2 Ra variability of the He isotopic signature of the currently outgassing fluids (Buttitta et al., 2023 and reference therein). During this time span, the background seismicity (Mw < 4) of the area was not linked to any short-term variation in the He isotopic signature (Caracausi et al., 2022 and reference therein).

In some of the studied samples, the mineral precipitation possibly took place during co-seismic deformation. There, variable sizes of the incremental crack and seal growth were documented along both C and SP-veins. These variable different sizes was recorded by syn-kinematic fibrous calcite minerals, which therefore recorded small-to-large slip events, and possibly were associated with the recent seismicity activity that effected the studied Irpinia area of southern Italy.

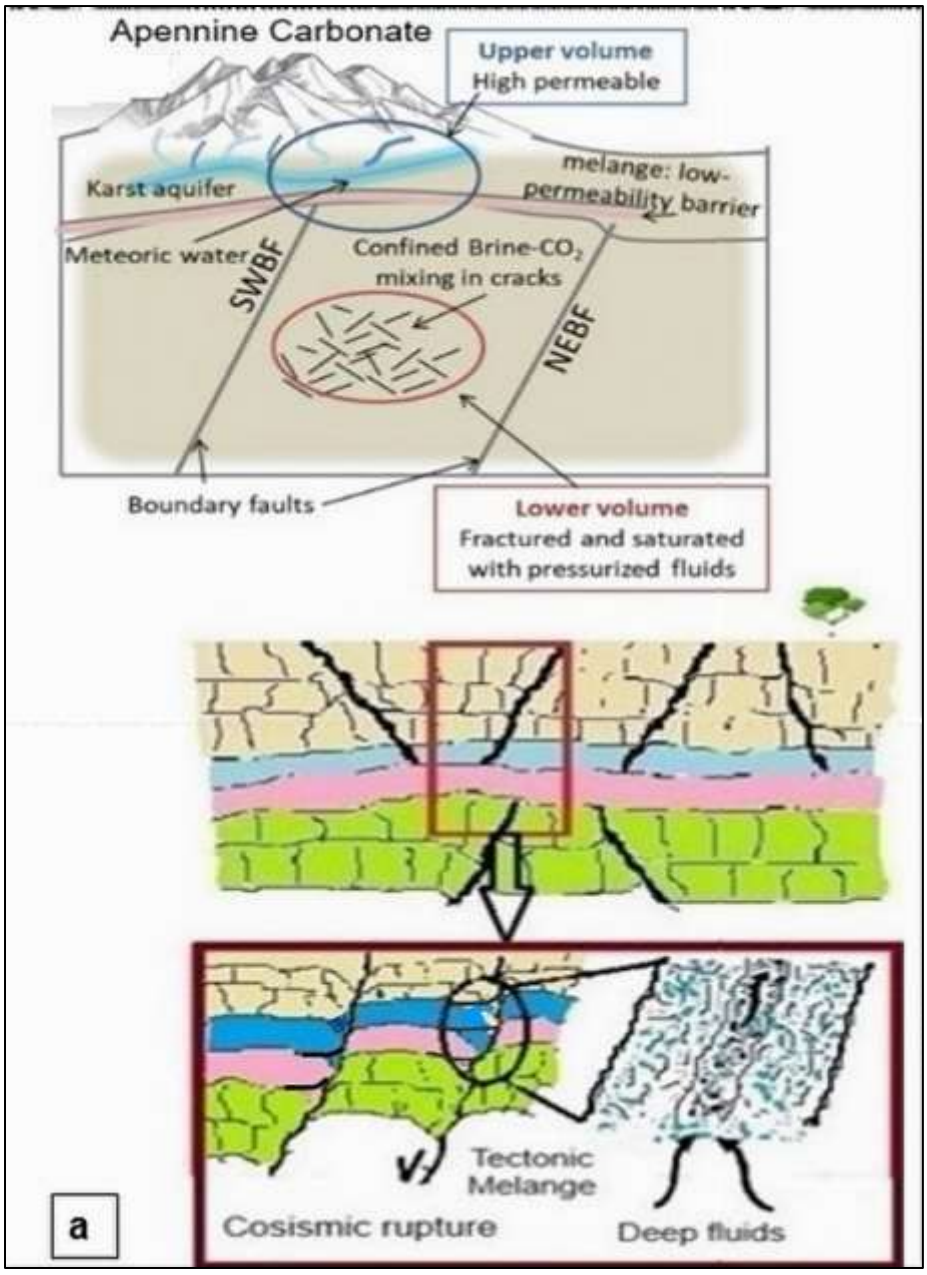

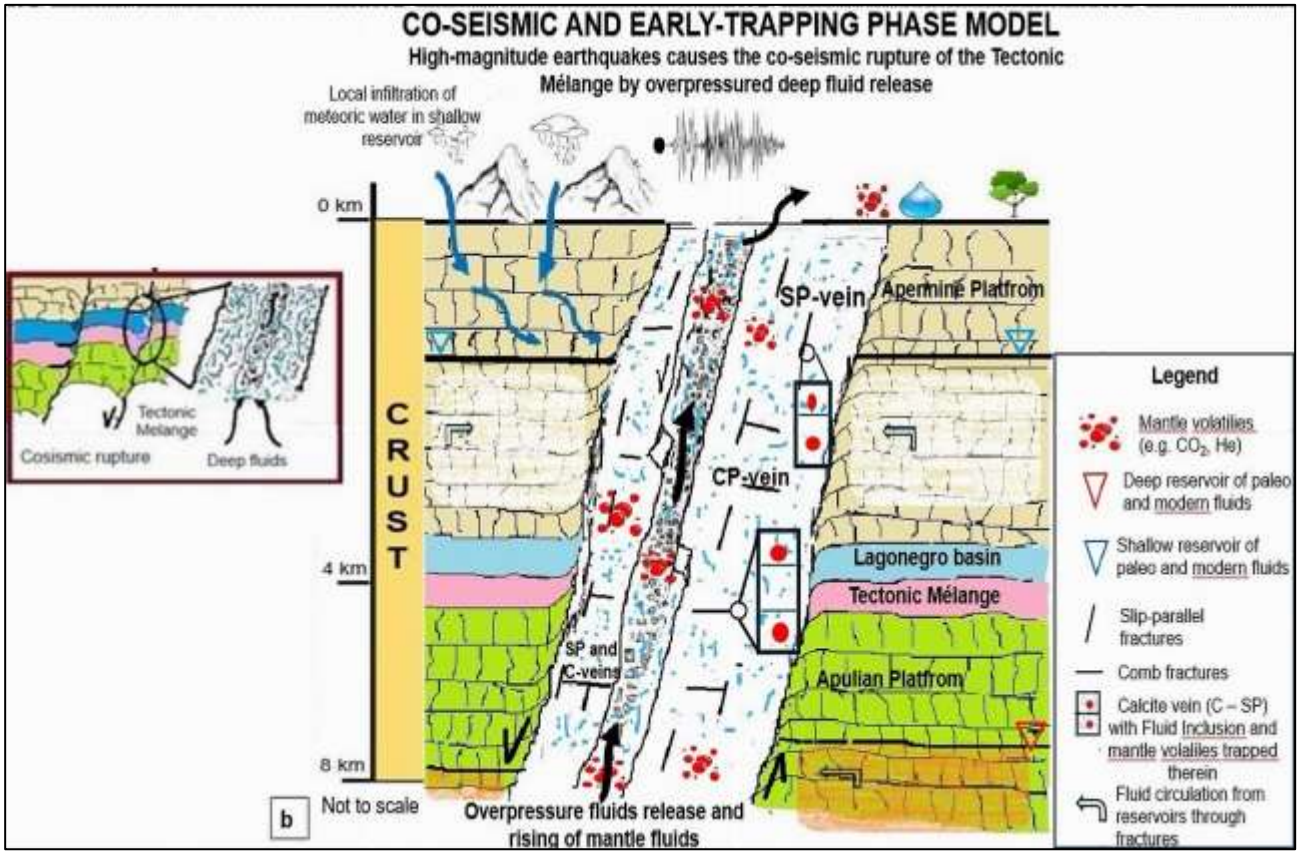

Fig 5.8 (a) *Cartoon showing the conceptual model for seismic-related fluid circulation and the main two rock volumes, where the VP/Vs and Vp*Vs changes a 1-5 and 8-12 km by pulse of overpressure deep fluids release with the co-seismic rupture of impermeable Tectonic Mélange (Amoroso et al., 2017; De Landro et al., 2022).* **(b)** *Cartoon showing the conceptual model for seismic-related fluid circulation implying: Overpressure deep fluids release and rising of mantle fluids from host carbonate at depths of about 8~10 km, in the Apulian carbonate host reservoir causes high-magnitude earthquakes with the co-seismic rupture of impermeable Tectonic Mélange. Some these, are trapped in shallow (3- 4 km) Apennine carbonate host reservoir and mixing with a meteoric and/or shallow derived water. The downward infiltration of meteoric water and/or shallow groundwater into Apennine carbonate-hosted reservoirs at depth and consequent fluid heating and fluid–rock interactions.*

Chapter 6 –Final remarks

By mean of the combined structural, geochemical and isotopic analyses of the faults-related calcite veins sampled from Contursi area (Irpinia, southern Italy) the following results were achieved:

- The studied mineralization veins cutting Apennine Carbonate platform sequences were collected in an area of about 40 km^2-wide, from medium-high angle fault segments. These faults show two mains roughly strike NE-SW and WNW-ESE within Contursi hydrothermal system. The mineralization veins related to these faults show two mains roughly strike: NNW-SSE and ENE-WSW.
- Calcite-filled both Comb and Slip parallel (C and SP, respectively) veins occurs along the fault planes of the active extensional Irpinian fault systems and very close to the epicentral area of the last catastrophic Mw 6.9 Irpinia earthquake (November 1980), which is between 1 and 5 km away from the Contursi Hydrothermal basin. In accordance with previous works, both C and SP-veins are interpreted as co-seismic or early post-seismic features developed as a result of multiple displacement episodes linked with seismic slip along the fault. The slight discrepancy with theoretical angles documented for both C-and SP-veins and the slip vector, can be interpreted as due to variation of the fault slip direction over time. We note that the attitude of C-veins, and their relations with the slip vector, is somehow compatible with the present-day extensional stress regime.
- Regardless of sampling sites, host-rock lithology and fault-strike directions, most of the studied calcite veins included blocky texture crystals. Despite the crosscutting relations and vein dip angles, the mineral precipitation probably post-dated the occurrence of brittle fracturing. The rapid fracture opening, possibly mediated by fluid overpressure, and later precipitation in a fluid-saturated open space likely occurred in the study rock. In only two cases we found a fibrous texture of calcite crystals that were formed by progressive small increments of opening shearing and mineral precipitation in a potentially co-seismic phase. Episodic displacements and/or multiple stick-slip episodes are consistent with the crack-and-seal textures observed within fault-related mineralization. In these two latter studied cases, new cracking events occurred only after the complete sealing of fractures, as shown by well-developed wall rock inclusions bands. The studied C- and SP-veins, are characterized by variable sizes of the incremental crack and seal growth within the same vein. The different sizes of incremental crack and seal growth may account for small-to-large slip events recorded along extensional faults by crack episodes of different magnitudes. This incremental growth may, in particular, be consistent with the recent extensional seismic sequence that lasted for months-to years with tens of thousands of earthquakes of various magnitudes of 1694 and 1980 Irpinia-Lucania seismic sequence.
- The $\delta^{13}C$ values of the studied calcite veins range between 0.59 ‰ and 3.17 ‰ and overlap the range of 0.82 – 2.78 measured in the associated host rocks, formed by limestone and dolomitic limestone (Lower Jurassic-Upper Paleogene). These isotopic values are comparable with $\delta^{13}C$ values of 2.21 ‰ assumed in the Apennine aquifer from carbonate mineral dissolution. Known that secondary processes (i. e. equilibrium fractionation

between soil, gas and aqueous phase, mineral precipitation and CO_2 degassing) can mask the pristine carbon isotopic signature it is plausible to hypothesize that the carbon measured in calcite veins is probably derived from the decarbonization processes of carbonate rocks and/or mantle-derived CO_2. Most of $\delta^{18}O$ values in mineralization veins are like those of the corresponding host rock which in turn fall in Mesozoic marine carbonate field. These stable isotopic values can be explained from shallow marine diagenesis, where an isotopic equilibrium occurred when fluids interact with host rocks for a long time. Also, the calculated $\delta^{18}O_{parentalfluids}$ values together with δD values measured in FIs, and the homogenization temperatures (between 100° and 130°C), like the maximum burial temperatures experienced by the Apennine carbonate Platform, confirm a long residence time of the fluid mineralization in the fractured Mesozoic marine carbonate host rock and the achievement of thermal and isotopic equilibrium with host rock. Furthermore, these statements are confirmed by trace elements and REE+Y data (LREE depletion, negative Ce anomaly) that show a partner typically observed in marine carbonates suggesting an imprinting pore fluid from marine carbonate. Some calcite veins, characterized by both a marked depletion $\delta^{18}O$ compared with Mesozoic Apennine carbonate platform host rock, due to a deeper burial environment of marine-derived fluids, and higher homogenization temperatures (between 200° and 320°C) indicate that the paleofluids probably come from a deeper reservoir at depth of about 8~10 km, where the Apulian Carbonate Platform is located. In this regard, the high magnitude earthquakes can due rupture of impermeable horizons (i. e. Irpinia tectonic Melange, located about 4 km depth in the study area) and so the rise to surface of ovepressured deep fluids.

- The noble gas analyses in FIs allowed to define the presence of paleofluids characterized by a wide range of R/Ra values (0.09 – 1.38 Ra, considering a SCLM) with a crustal and mantle (up to 20%) component and a local atmospheric contribution, also confirmed by the low salinity measured in the FIs between 0.4- 0.6% NaCl values. The strongest measured He isotopic in FIs (1.38Ra) fit well with values of current high-flux CO_2 gas emission in the studied area (1.41Ra). This similarity indicates that the ratio of crust-to mantle He remained approximately constant over time along the studied faults. The variability of He isotopic signature in FIs, that is not consistent with narrower range of He ratios for the current outgassing, can be mainly due to early trapping processes occurred in the area.

The multiple co-seismic dilatancy model, applied to the above-reported data allows to propose a general model of fault-related fluid circulation in the Contursi Hydrothermal basin, in which the overpressured fluids, characterized by crustal and mantle derived He (up to 20 %), uprise from a deep reservoir, located in the Apulian Carbonate platform, and reach shallower crustal levels (1- 5 km) where come into thermal and isotopic dis-and-equilibrium with Apennine carbonate host rock. This generates the two distinct groups of studied mineralization calcite veins and associated FIs. The uprising of overpressured deep fluids is facilitated by crossing on the impermeable horizon (Irpinia tectonic Mélange) caused by probable past strong earthquakes. This high permeability pathway is still

active, as suggest by soil gas measurement in the investigated, indicating a current outgassing of mantle derived fluids. However, the origin of mantle component recorded in FIs it is not clear yet and two possible explanations can be given: (1) The mantle-derived fluids are due to degassing of magmatic intrusion at depth; (2) a lithospheric discontinuity down to the mantle is present.

Future investigations on dating of calcite veins may better indicate the actual timing of the precipitation of calcite veins in relation to studied faults and the relationship between fluid origin, their uprising toward shallower crust levels and the related secondary processes that can occur. In addition, such investigations are fundamental to understanding the role of fluids in crustal deformations over time and in processes of earthquake nucleation and to furnish an answer upon long time monitoring in this region (i. e. IRPINIA Near Fault Observation) and other general worldwide fault zone.

APPENDICES – Analysis methods

APPENDICES 1 – STRUCTURAL AND MICROSTRUCTURAL METHODS

1.1 - Structural analysis of mineralization veins fault-related and fractures

Calcite (CaCO3), a trigonal mineral, is the most stable form of calcium carbonate is commonly found as a precipitated element within open fractures, and as coating of the fault planes. The types and origin of fault-related calcite fills have been reviewed extensively in the literature, e.g. Bons et al. (2000, 2012, 2022 and reference therein), Passchier and Trouw (2005).

These authors defined veins as "distinct polycrystalline mineral volumes that formed within a rock and that are filled with one or more minerals that precipitated from an aqueous fluid" (Bons, 2000). One could say that veins are structures that reveal a deformation history for structural geologists, while veins are principally indicators of past fluid flow for geochemists. The veins represent planar mineralization zones formed by precipitation from paleo-fluids derived from a variety of sources (atmosphere, crustal, hydrothermal activity, mantle) and represent a fundamental key to understanding fluid-rock interaction during the seismic cycle and related mechanisms and formation phase (pre, co and post-seismic). Accordingly, the veins within extensional faults can be record of dynamic dilation and potentially fracture opening during seismic events.

In the field, the attitude of main fault planes, kinematic indicators such as striae and calcite steps, and minor slip surfaces, barren fractures, and veins was measured. For this PhD thesis were found and studied only:

- ***Comb and slip-parallel veins***, as reported above, are respectively oriented perpendicular and parallel to the main fault planes (Fig.1.1, Hancock and Barka, 1987; Stewart and Hancock, 1990; Curzi et al., 2024 and reference therein). These veins were initially interpreted as “tension cracks reflecting down-dip stretching during localized post-slip stress reorientation” (Hancock and Barka, 1987; Stewart and Hancock, 1990). However, it has more recently been proposed that comb and slip-parallel veins can also form potentially during co-seismic down-dip displacement of the footwall block, and co-seismic stress release localizing deep overpressured fluids ingress and flow (Smeraglia et al., 2018 and reference therein).

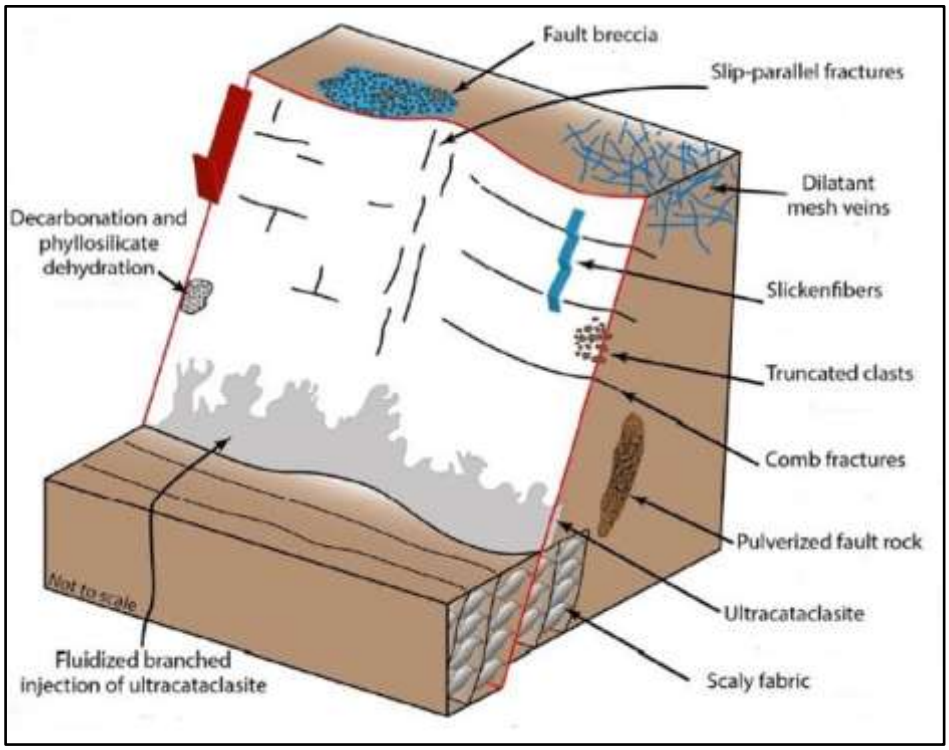

Fig. 1.1. *Conceptual cartoon showing meso- and microstructural indicators of fossil seismic cycles, earthquakes described in Stewart and Hancock, 1990. (Cartoon modified from Curzi et al., 2024).*

On the basin of the information provided in figure 1.1, other meso-and microstructures, reported by Curzi et al. (2024 and reference therein), but not include in the present PhD thesis are the following:

- *Scaly fabrics*

Scaly fabrics, including S-C fabrics (Fig.1.1), accommodate a combination of pressure solution and frictional sliding associated with fluid pressure fluctuations. They commonly form in suitable lithotypes and during inter-seismic phases, when slow aseismic (creep) deformation occurs in response to elastic strain accumulation. Pressure solution mobilizes pore fluids from the host rock (likely in isotopic and thermal equilibrium with it), and leads to precipitation of tectonic veins and slickenfibers, enhancing the healing of the fault zone and promoting elastic strain accumulation.

- *Fading grain boundaries, voids and/or vesicles*

Such structures, occur along fault planes and form in response to high strain rates (co-seismic slip) and associated frictional heating, which may induce decarbonation and/or phyllosilicate dehydration and transformation via mixed layer minerals, in the first few millimeters off the fault planes. Hence, these micrometric scale structures are diagnostic of fossil earthquakes.

- *Ultracataclasite layers*

Ultracataclasite layers commonly occur along the fault plane and consist of matrix and clasts < 10 μm in diameter. Locally, they contain fluidized injectites that localize displacement during repeated co-seismic slips (Fig.1.1).

- *Truncated clasts*

These elements are locally found along discrete fault planes, where they are thought to undergo a sharp truncation during co-seismic fault slip.

- *Pulverized rocks*

These rocks are extremely comminuted rocks that commonly localize at the fault core-damage zone transition (Agosta and Aydin, 2006), within the fault core (Doan et al., 2012), and/or within the damage zone (Curzi et al., 2024). The pulverized rocks are crosscut by numerous dilational microfractures, and are indicative of high strain rates, and, possibly, seismic faulting (co-seismic phase, Fig.1.1). They are commonly associated with physical processes including dynamic unloading dynamic fragmentation, in situ shattering, and transient tensile pulses. Very recently, the pulverized rock were associated to accumulation and rapid decompression of pressurized CO_2 rich gases (Billi et al., 2023) suggesting the involvement of deep and/or exotic fluids likely in chemical-physical disequilibrium with the host rock.

- *Mesh (or stockwork) veins*

Mesh veins are defined as sets of dilatants, randomly-oriented veins (Fig.1.1), which form due to hydraulic fracturing (accordingly, these veins are after mineral infilling of hydrofractures) under low or even null differential stress, and fluid overpressure conditions associated with pre/co-seismic phases. The development of hydrofractures, which is genetically associated with crack opening and rapid infilling by pressurized fluids, can potentially account for the rapid ascent of deep fluids in chemical-physical disequilibrium with the host rock during earthquakes.

- *Crackle and chaotic cement-supported fault breccias*

These types of breccias (Fig. 1.1) develop during co-seismic implosive brecciation with episodic fluid overpressure episodes, and subsequent rapid depressurization during fluid venting. The crackle and chaotic cement-supported breccias may hence record episodes of pronounced dilatancy, and of the possible involvement of possibly exotic pressurized fluids.

- *Slickenfibers*

Slickenfibers develop along fault planes and surfaces along which slip localizes (Fig.1.1) and track the displacement (slip) vector. They form during shear associated with (i) slow inter-seismic or post-seismic deformation, during which fluid pressure fluctuations can be associated with slow shear events (ii) and/or rapid co-seismic deformation occurring under repeated fluid overpressure and associated rapid shear events. The association of slickenfibers with specific deformation-precipitation processes, and with a specific phase of the seismic cycle, requires the identification of their internal textures.

1.2 - Microstructural and textural mineralization veins

Microstructural analysis of calcite veins was performed by employing optical microscopy on polished 40-50 µm-thick sections, which were previously prepared at the University of Basilicata (Italy) and at the University of Salamanca (Spain). This analysis is used to investigate the texture of calcite minerals and crosscutting relations of calcite veins. In Fig. 1.2 are shown a the most common of types of fault-related calcite veins (Roberts and Holdsworth, 2022).

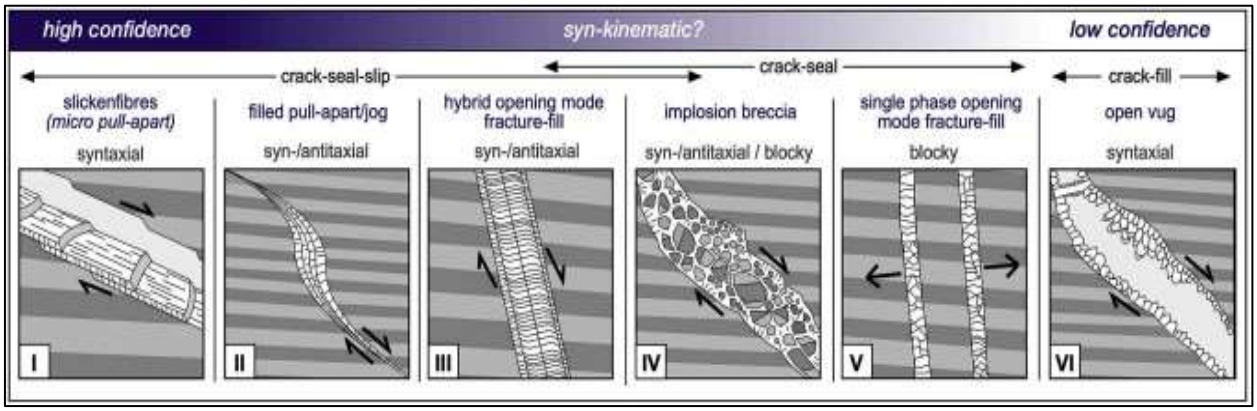

Fig. 1.2. Types of fault-related calcite fracture-fills (veins)**,** Roberts and Holdsworth, 2022

The cemented fractures (veins) shown in Fig. 1.2 display the information we can derive to assess either the timing and/or the kinematics of fault slip. In the aforementioned figure, the veins are drawn so that those on the left are easiest to unequivocally linked to fault slip, whilst those on the right are less reliable. Furthermore, the most common growth morphologies documented for the single vein types are shown. The terminology is purposely restricted to syntaxial and antitaxial to respectively describe the mineral growth from the host rock towards the center of the open void (syntaxial), and from a nucleation point within the void or vein towards the host rock (antitaxial). Stretching fibres may exist with both of these opposing growth structures, and various other terms are in use in the literature (see Bons et al., 2012).

Morphology of internal structure

As expanded below, the internal structure of mineralization veins (Fig.1.3) allows one (i) discriminating high vs. low fluid pressure (ii) constraining the deformation of mechanisms and strain rate. Here distinguish four primary textures (Bons, 2000; Bons et al., 2012):

1. Blocky
2. Elongate blocky
3. Fibrous
4. Stretched

A blocky texture (Figs. 1.3a; 1.2V) is characterized by roughly equidimensional and randomly-oriented crystals, and implies the rapid crack opening possibly mediated by fluid overpressures, and the fast precipitation on fluid-

filled open cracks (Passchier and Trouw, 2005; Bons et al., 2012 and Curzi et al., 2024 and reference therein). Blocky texture indicates rapid deformation and fracture filling likely associated with the involved overpressured fluids. However, blocky texture does not directly provide evidence of fossil earthquakes and can be also associated with fluid overpressures during pre – and post seismic phases. Recent studies (Manniello et al., 2023; Todaro et al., 2024), documented widespread calcite blocky textures in fractured and faulted platform carbonates of southern Italy, wich was interpreted as due to mineral precipitation in phreatic conditions.

Elongate blocky texture (Fig. 1.3b, b') contains rod-shaped crystals characterized by high length/width ratio and implies the repeated increments of fracture opening, and the progressive incremental precipitation (Passchier and Trouw, 2005; Bons et al., 2012). This type of texture is not directly associated with fluid overpressure and does not directly provide information on the phases of seismic cycles. Some crystals are more favoribly crystallographically-oriented than others with respect to the general growth direction, and hence outgrow the unfavorably-oriented ones.

Fibrous texture (Figs.1.3c, c'; 1.2III), is characterized by stretched or rod-shaped crystals with a much higher length/shear and precipitation (Passchier and Trouw, 2005). This opening-mode or hybrid (shear) veins may form adjacent to major fault planes, or along minor fractures within fault demage zone. In such cases, this texture allows the assessment of the mutual crosscutting relations among the various fibrous minerals, hence permitting the characterization of the deformation increments associated to fault slip. In case of crack-seal slip of cemented fractures along individual faults, the fibrous minerals commonly display curved or inclined shapes forming the "Slickenfibre steps", that are commonly employed for the assessment of the sense of shear (Passchier and Trouw, 2005). Because such minerals growth forms synchronously with displacement along shear fractures, these types are desirable for confidently linking dated mineral growth to fault slip (Robert and Holdsworth, 2022). This texture is thus indicative for a potentially past earthquake occurred.

Stretched crystals texture, forms when additional mineral precipitation occurs on the surface of existing grains. The primary distinction between the previous textures and the stretched crystals is that the latter ones are characterized by an additional growth that took place inside the grains (on the surfaces of the half grains), with the space for new growth provided by (micro) fractures that cut through the grains.

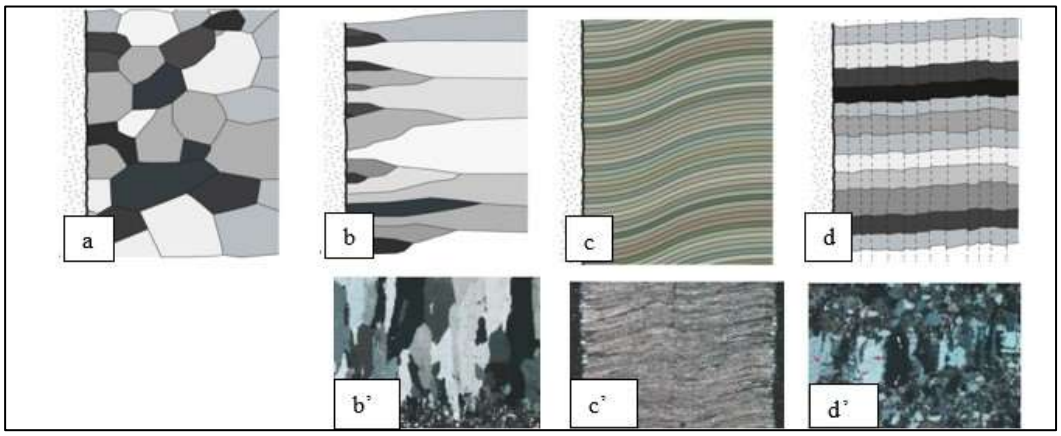

Fig.1.3 *Morphology of internal structure.* ***(a)*** *blocky texture;* ***(b, b')*** *Elongate blocky texture;* ***(c, c')*** *Fibrous texture;* ***(d, d')*** *Stretched crystals texture. Modified after Bons, 2000.*

Vein Formation

Vein formation essentially involves two steps (Bons, 2000, 2012 and reference therein):

A. transport of vein forming material (nutrients) to the growing vein.

B. precipitation of the vein forming mineral(s) in the growing vein.

As veins were defined as forming from precipitation from an aqueous fluid (possibly containing CO_2, but excluding melt), it is clear that material transport involves transport in solution and that precipitation involves supersaturation of a fluid.

Precipitation in a vein

The crack-seal mechanism

The crack-seal mechanism was first introduced by Ramsay (1980), and then has quickly become the most accepted mechanism for the formation of fibrous/elongate blocky veins. The mechanism itself does not dictate any fluid or solute transport mechanism, nor a specific cause for precipitation inside a vein. The essence of the crack-seal mechanism is the repeated formation of a fracture, which is subsequently sealed by precipitation of vein sealing the fracture. The crack-seal cycle can be repeated hundreds of times, typically adding about 10 μm to a vein each cycle. The crack-seal mechanism can explain many parallel walls rock inclusion trails that are often found in veins. The effect of the crack-seal mechanism on the morphology of vein forming crystals (stretched / elongate blocky / fibrous).

Vein growth without fracturing

Probably the most clear-cut case of vein growth without fluid flow, but by diffusional solute transport is a pressure fringe adjacent to a rigid object (e.g. a pyrite grain). The presence of a rigid object in a deforming/stressed rock causes a perturbation of the stress and pressure field around the object. The sides of the object facing the highest compressive normal stress experience the highest pressure, while the sides facing the lowest normal stress experience a relative low pressure. This pressure difference can drive dissolution at the high-pressure sides,

diffusional transport to the low-pressure sides and precipitation there to form the pressure fringes. This process can occur without the formation of a (thin) fracture at the low-pressure sides of the rigid object. It may be important that pressure fringes are usually fibrous (not elongate blocky) and appear to form without any brittle failure: there are no microstructural indicators for fracturing and the stress and pressure field around the object provide the driving force for material transport and precipitation in the fringe. This supports the hypothesis that the fibrous crystal morphology may form in the absence of fracturing. In the absence of fractures, diffusion is the only viable transport mechanism, and we may infer that fibrous veins are indicative of diffusional material transport.

Vein growth in fractures

Fractures are the most common sites for veins to form, as fractures provide space for precipitation and preferred pathways for fluids to flow through. Two main causes for precipitation inside fractures can be distinguished (Bons, 2000):

Vein-forming material is derived from a fluid that resides in both fractures and surrounding wall rock. The conditions inside the fracture and in the wall, rock is different, such that a fluid that does not produce any (significant) precipitation in the wall rock does precipitate one or more minerals inside the fracture. Vein formation can then occur in the fracture by either diffusional transport in a possibly stagnant fluid or by flow of a fluid that brings local fluid from the wall rock into a vein. Again, two scenarios can be proposed:

- the fluid is supersaturated with respect to the vein forming minerals in both fracture and wall rock, but precipitation is inhibited in the wall rock. This is supposed to occur in low porosity rock, which can inhibit precipitation determining that a pore fluid can remain significantly supersaturated until a fracture provides a possible site for precipitation. Material transport to such fractures can be by diffusional transport or by advective flow.
- the difference in conditions between fracture and wall rock causes dissimilarities in the chemistry of the fluid residing in fracture and wall rock. Such a dissimilarity could be due to a difference in fluid pressure in both reservoirs. Silica solubility is pressure dependent, and therefore it can be argued that a constant concentration of silica, fluid may be undersaturated in a high fluid pressure wall rock and supersaturated in a low fluid pressure fracture, where precipitation then occurs. Veins are often associated with deformation by dissolution-precipitation creep or ‘pressure solution’.

Vein forming material is derived from an extraneous fluid that enters the fractures, where it is/becomes supersaturated with respect to the vein forming minerals. Fractures, of course, provide high conductivity pathways for channelized fluid flow and their presence thus allows fluid to flow over long distances and, in the process, become over- or undersaturated in its solute, primarily due to changes in pressure and temperature. Minerals precipitating in a fluid filled fracture grow into an open fluid, even though there may only be a few microns of free space before the other side of the fracture is encountered.

Calcite twins: stress-strain markers and indicators of paleo-tectonic regime

Calcite twinning can be used an indicator of strain direction, intensity and temperature of deformation (Ferrill et al., 2004). Twin lamellae are a widespread feature in calcites of any type and origin. Twinning of calcite permits an important intracrystalline deformation at very low temperatures and very small confirming pressures (Burkhard, 1992). The appearance of calcite twin lamellae changes systematically as a function of deformation temperature (Burkhard, 1993). For example, Ferrill et al., (2004) correlated the mean width of twin lamellae with the temperature of deformation such that thin twins (approximately 1 μm) are predominantly below 170°, whereas thick twins (> 2 μm) are predominantly above 200°C (Fig. 1.4). Furthermore, above approximately 200 °C, curved twins, twinned twins and completely twinned grains indicate the progressive importance of other slip systems, and larger intracrystalline strains are possible. At ca. 250 °C and above ancient straight twin lamellae are modified into irregular geometries by recrystallization and grain-boundary migration.

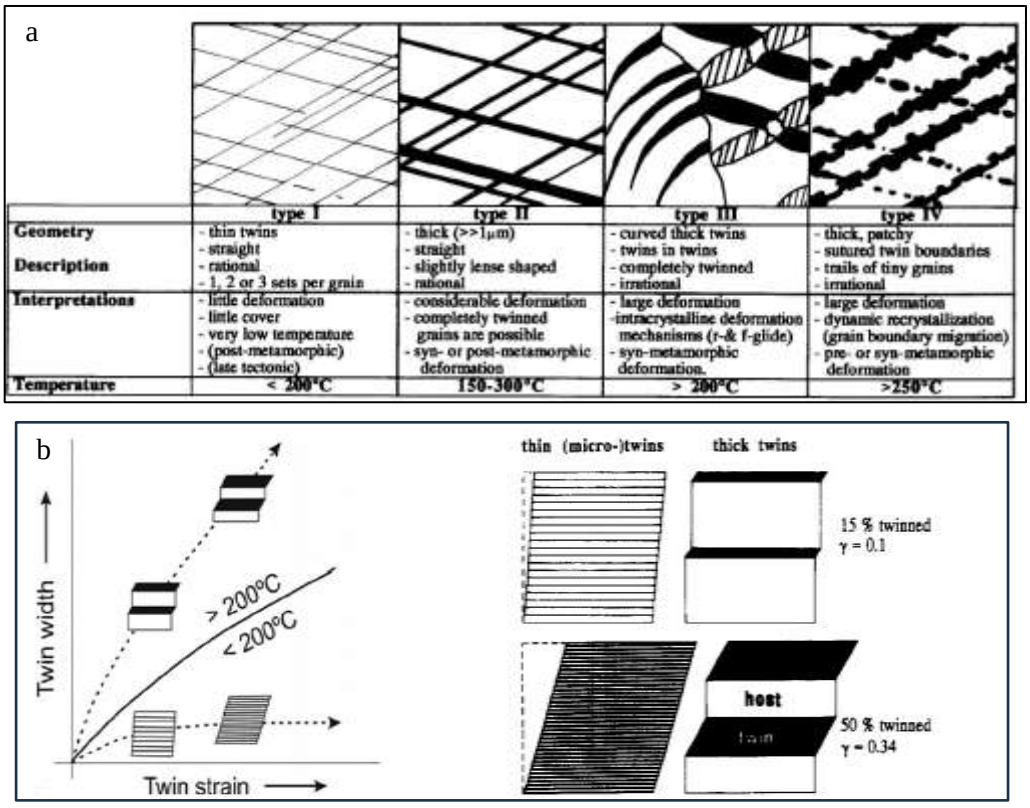

Fig. 1.4 (a) *Classification of twins according to their appearance in section. Four different types of twins are distinguished and interpreted in terms of deformation temperature and mechanisms (Ferrill, 1992).* ***(b)*** *Schematic diagram illustrating the difference between thin and thick twins, twin density (number of twins per mm) and percentage volume fraction of twin lamellae. By Lacombe et al. (2021 and reference therein).*

APPENDICE 2 - GEOCHEMICAL AND ISOTOPIC METHODS

This sub-chapter is providing to describe all the geochemical methodologies used in this PhD work such as: major element analysis, trace and REE-Y patterns; stable isotopes analysis of carbon ($\delta^{13}C$), oxygen ($\delta^{18}O$) in bulk calcite crystals to investigate the fluid source of calcite vein precipitation, crustal residence times, fluid-host rock carbonate interaction and finally the modalities of fluid circulation patterns in the upper crust. Deuterium (δD-H_2O), and noble gases helium (He), neon (Ne), argon (Ar) their concentrations and isotope ratios within Fluid inclusions (FIs) entrapped in calcite minerals that are excellent tracers of both fluid sources and physical processes within the crust.

2.1 Major, Trace elements and REE+Y patterns

Through this analysis makes it possible to characterize the chemistry of the mineralization, and the host rock hosted. The major elements (such as, Mg Ca, Al, Fe, Si) expressed in % weight; the trace elements (such as V, Rb, Sr, Ba, Pb, U, Th, etc.) and the REEY (such as La, Ce, Eu, Y etc.) patterns, expressed in ppm.

Through these analyses, one can also investigate the degree of interaction with the host rock and the residence time of these paleofluids in the lower and/or upper crust. Finally, by analyzing certain dissolved elements such as Sr, Y, La, Ce it is also possible to investigate the aqueous source and the environmental conditions from which this mineralization precipitated (groundwaters, meteoric, brines, hydrothermal fluids).

Major elements, trace Elements and REEY-patterns were analysed through an inductively coupled plasma-mass spectrometry (ICP-MS) at the Actlabs research laboratories (https://actlabs.com/geochemistry/lithogeochemistry-and-whole-rock-analysis/lithogeochemistry), with WRA+Trace 4 Lithoresearch + 4B1 methodology, illustrated below.

Sample are prepared and analyzed in a batch system. Each batch contains a method reagent blank, certified reference material and 6 % replicated. Samples are mixed with a flux of lithium metaborate and lithium tetraborate and fused in an induction furnace. The molten melt is immediately poured into a solution of 5 % nitric acid containing an internal standard and mixed continuously until completely dissolved. The samples are run for major, oxides and selected trace elements (4B) on an ICP. Calibration is performed using 14 prepared USGS and CANMET certified reference materials. One of the 14 standards is used during the analysis for every group of the samples. Totals should be between 98.5% and 101%. If results some out lower, samples are scanned for base metals. Low reported totals may indicate sulphate being present or other elements like Li which won't normally be scanned for. Samples with low totals however are automatically re-fused and reanalyzed. A 0.30 g sample is digested with four acids beginning with hydrofluoric, followed by a mixture of nitric and perchloric acids, heated using precise programmer-controlled heating in several ramping and holding cycles which takes the samples to dryness. After dryness is attained, samples are brought back into solution using hydrochloric acid. With this digestion certain phases may be only partially solubilized. In-lab standards (traceable to certified reference

materials) or certified reference materials are used for quality control. Sample are analyzed an ICP, and elements and Detection Limits are expressed in ppm.

Generally, the most common elements in rocks are oxygen: 46.6%; silicon: 27.7%; aluminum: 8.1%; iron: 5.0%; calcium: 3.6%; sodium: 2.8%; potassium: 2.6%; magnesium: 2.1% (values are expressed as percentages by weight). These eight elements, which each have a percentage greater than 1%, make up almost 99% and are called *major elements.*

The other elements (less than 0.1%) are called *trace elements.*

In the limestone the correlation between CaO and SiO_2 is generally high; similar relations were observed between CaO and Al_2O_3, CaO and Fe_2O_3. Limestones show general negative correlations between CaO and SiO_2, Al_2O_3 and Fe_2O_3 indicating that Ca in the carbonates is of biogenic origin (Zhang et al., 2017). The low abundance of Al_2O_3 and Fe_2O_3, their good positive correlation along with the weak correlation between Al_2O_3 and MnO suggest the limestone formed at distance from the continent (Zhang et al., 2017) with the little contamination from terrestrial particulate matter.

The concentration of trace elements is very low, generally < 0.1 % (< 1000 ppm), such that they do not alter the stability of the phases present (they are not stoichiometric constituents of a mineral). Their distribution between the given mineral and the coexisting fluid, being linked to the occupation of precise lattice sites in the various minerals, can be calculated on the basin of solid/liquid distribution coefficients Kd= s/l

$$Kd^{s/l} = \text{concentration in the mineral/concentration in the liquid} \quad (1)$$

INCOMPATIBLE elements (in minerals) are preferentially concentrated in the liquid: $Kd^{s/l} < 1$; The COMPATIBLE elements are concentrated in the mineral phases $Kd^{s/l} > 1$.

The incompatible elements are divided into 2 groups:

- *Large Ion Lithophile Elements (LILE)*: K^{+}, Rb^{+}, Ba^{+2}, La^{+3}, $Ce^{+3,+4}$, $U^{+3,+4,+5+6}$ $Pb^{+2,+4}$, Th^{+4}

They are effectively complex by aqueous fluids and are mobile during alterations processes, weathering.

- *High Field Strength Elements (HFSE):* Zr^{4+}, Pb^{4+}, Ta^{5+}, Nb^{5+}, Ti^{4+}

They are very slightly soluble in aqueous fluids and generally immovable during the alteration processes.

The *LILE* and transition metals have been normalized to upper continental crust (UCC, McLennan, 2001); the limestones have much lower trace elements contents that average upper crust (i.e. < 1) except for Sr and U. The Sr values in the limestones lie between 42 ppm and 838 ppm, with an average of 293 ppm which is lower than the average Sr content (350 ppm) of the Post-Archean Australian Shales (PAAS, Poumand et al., 2012) commonly used as the reference reservoir for normalizing limestone values. V, Cr, Ni, Co and Cu are one order of magnitude depleted in comparison to UCC values.

As defined by *IUPAC* (International Union of Pure and Applied Chemistry), the Rare Earth Elements (REE)

+Yttrium is a group of 17 chemical elements, 15 of which are found in the penultimate row of the periodic table. The REE-Y normalized to PAAS (REY_{PAAS}) show variation of three orders of magnitude, and all are depleted relative to PAAS. The REY_{PAAS} patterns for the limestone display an overall progressive enrichment of heavy REE (HREE) and light REE (LREE). The relative enrichment of HREE over LREE observed is typical of seawater sediments (Fig. 2.1) and has been attributed to the formation of complexes with CO_3^{2-}. Other common features include the negative Ce anomaly and a positive Y anomaly (Tostevin et al., 2016). Other anomalies e.g. may be positive in the Eu content for High T hydrothermal fluid.

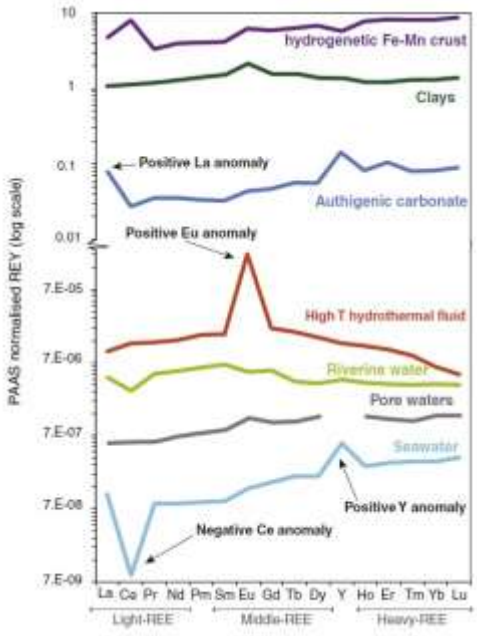

Fig. 2.1. *Shale normalized REEY patterns representing key natural environments and minerals, showing typical anomalous features such as Ce, La, Eu and Y anomalies (Tostevin et al.,2016).*

2.2 Mineralogical analyses by XRPD (X-Ray Powder Diffraction)

Mineralogical analysis of veins and host rock associated, were performed on specimens obtained by either bulk rock and vein infill, by using a Siemens D5000 equipment with CuKα radiation, 40 kV and 32 mA. The powdering of the samples for chemical and mineralogical analysis was made by using a Retsch RS 100 planetary mill equipped with agate jars and agate milling balls. This analysis makes it possible to characterize the various mineralogical phases present in both the veins and the associated host rocks.

In all the diffractograms of the analysed samples, are clearly visible the intensity mains peaks of the calcite mineral (CaCO3), present at positions [2 Theta] = 29, and 48-49. Theta (θ) is the angle of x-ray incidence in the reticular plane of minerals, derived from Bragg's equation:

$$2d\text{sen}\theta = n\lambda \quad (2)$$

From the angle 2θ, relative to the various peaks (diffraction effects), in the diffractogram it is calculate the

interplanar distance of the corresponding to a reticular planes family can be calculated. We then proceed to mineral recognition using the Hanawalt's handbook, which of each known minerals, reports the interplanar distances corresponding to the most intense diffraction effects. Based this diffractogram results, for example, the percentages of the main constituents of a carbonate rock such as calcite and dolomite are obtained: calcite (CaCO3) with 2θ angle = 29 and dolomite ($CaMg(CO_3)_2$) at 2θ angle = 31. From a semi-quantitative analysis, the area subtended by the intensity peak, the various mineralogical phases constituting that particular rock are calculated.

2.3 Stable Carbon and Oxygen isotopic signature of carbonate

This analysis performed to investigate the *stable C isotopic signature ($\delta^{13}C$) in calcite minerals forms veins.*

Using a microdrilling with diamond tips of different sizes to extract the mineralization from whole rock (ca. 20 mg of powder's samples); the extracted sample is placed inside the gas extraction and purification line with H_3PO_4 'phosphoric acid" causing them to react: $CaCO_3+H_3PO_4 \longrightarrow CaHPO_4+CO_2+H_2O$.

After a heating and subsequent cooling phase using liquid nitrogen, the gas extracted (CO_2) from the previous reaction between calcite and phosphoric acid is analyzed for C isotopes in the CO_2 obtained using a mass spectrometer (Sira-II, "dual inlet" produced by VG-Isotech) at stable isotopes laboratory of the University of Salamanca (Spain). The experimental values were normalized with internal standards (EEZ-1). Results are reported according to the conventional δ notations Vienna Pee Dee Belemnite (PDB). The analytical error derived from this analysis is ± 0.2 ‰.

Carbon stable isotopes (^{12}C and ^{13}C), conversely to the unstable ones (e.g., ^{14}C), are not subjected to radioactive decay. Indeed, their abundance in natural fluids, is controlled by physical and biological processes such as equilibrium reactions and plants photosynthesis (Laughrey and Baldassare, 2003). Stable carbon isotope geochemistry aims to identify the carbon origin in natural fluids.

Indeed, carbon occurs in a wide variety of compounds and is a widespread element in nature in both oxidized environments, such as sedimentary carbonate rocks or gaseous CO_2 to organic substances produced in highly reduced conditions in the biosphere. Given the differences in isotopic mass, different isotopes assume different behavior during natural processes such that, sedimentary carbonates and organic matter possess distinct stable carbon isotope compositions, related to two main reaction mechanisms (Hoefs, 1987): (1) isotope equilibrium exchange reactions in the inorganic carbon cycle (atmospheric CO_2-dissolved bicarbonate-solid carbonate) leading to an enrichment of ^{13}C in carbonate rocks; (2) kinetic isotope effects during plants photosynthesis make ^{12}C the most abundant carbon isotope in organic matter. Similarly, to eq. (delta notation water stable isotopes), the stable carbon isotopic composition is expressed by the delta notation:

$$\delta^{13}C = (R_{sample}/R_{std} - 1)\ x\ 1000\ (‰) \quad (3)$$

With the carbon isotopic ratio (R) for both a given sample and the standard is given by R = $^{13}C/^{12}C$. For carbon isotopic composition, the international standard is the Pee Dee Belemnite (PDB) (Hoefs, 1987) for which have a $\delta^{13}C$=0 ‰ have been estimated. The carbon isotopic composition ($\delta^{13}C$) of carbonates reflects the composition and origin of dissolved inorganic carbon in the fluids because carbon isotope fractionation at low temperatures is only minimally temperature-dependent (Hoef, 1997). Marine carbonates are characterized by $\delta^{13}C$ value close to 0 ‰ (V-PDB). Carbonates of tectonic origin characterized by negative $\delta^{13}C$ values and hosted in marine carbonates indicate a contribution of carbon derived from organic carbon respiration in soil and/or from the interaction of fluids with organic matter-rich rocks (Sharp, 2017).

Deep CO_2 arising from the mantle is characterized by $\delta^{13}C$ values between – 5 ‰ to -3 ‰ (Chiodini et al., 2000). Deep CO_2 arising from the decarbonation of carbonate-rich rocks at depth is instead enriched in the heavy carbon isotope ^{13}C with respect to the parental carbonate (Sharp, 2017). Deep CO_2 produced by decarbonation can be characterized by $\delta^{13}C$ comprised between 4 ‰ and, when produced from organic-rich carbonate, -7 ‰ (Rielli et al., 2022). In tectonically active regions, such as the Apennines, deep CO_2-rich fluids can flow upward especially during pre-to-co-seismic phases (Caracausi and Paternoster, 2005; Di Luccio et al., 2018) and lead to tectonic carbonate precipitation during co-seismic rapid CO_2 degassing (Billi et al., 2023). Tectonic carbonates precipitating from such a rapid degassing of deep CO_2-rich fluids show $\delta^{13}C$ values > ~ 6-8 ‰, thus clearly accounting for an isotopic fluid-rock disequilibrium associated with the involvement of deep CO_2-rich fluids (Di Luccio et al., 2018; Billi et al., 2023).

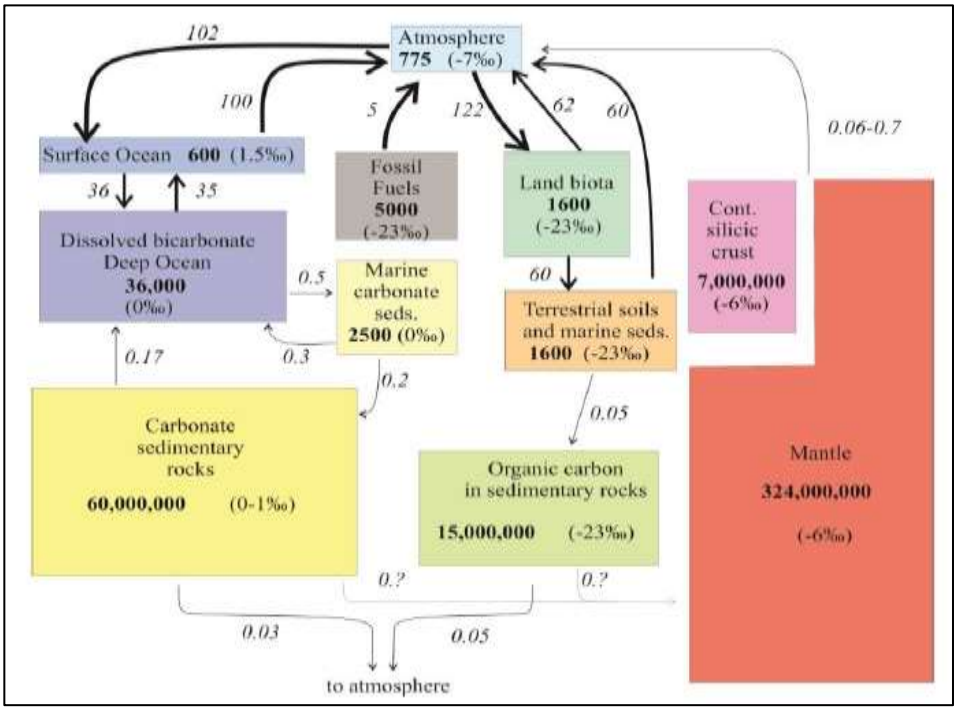

Fig. 2.2 *Carbon cycle, showing amounts, fluxes and $\delta^{13}C$ values of different reservoirs. Abundance shown in bold in 10^{15}g. Flux is shown in italics in 10^{15} g/yr. $\delta^{13}C$ values are in parent (Sharp, 2017).*

The stable oxygen isotope composition ($\delta^{18}O$) of carbonates depends on the $\delta^{18}O$ and the temperature of the fluid from which they precipitate (e.g., Sharp, 2017). Different fluids and rock types have different ranges of $\delta^{18}O$ values but when fluid interact within rocks for a long time they can equilibrate and reach isotopic equilibrium (Hoefs, 1997). By comparing the $\delta^{18}O$ of tectonic carbonates and host rocks, it is possible to deduce whether mineralization fluids were in isotopic (dis)equilibrium with the host rocks provides that the temperature of precipitation of the carbonates can be constrained.

Using a microdrilling with diamond tips of different sizes to extract the mineralization veins from whole rock (ca. 20 mg of powder's samples). Oxygen isotopic analyses were carried out at the Servicio General de Análisis de Isótopos Estables (NUCLEUS - University of Salamanca, Spain). Oxygen in calcite crystals was extracted by fluorination (Clayton and Mayeda, 1963) employing a Synrad 25W CO2 laser (Sharp, 1990) and ClF3 as reagent (e.g. Borthwick and Harmon, 1982), and oxygen isotope ratios were measured on a VG-Isotech SIRA-II dual-inlet mass spectrometer. Both internal and international reference standards (NBS-28, NBS-30) were run to check accuracy and precision. Results are reported in $\delta^{18}O$ notation relative to the Vienna Standard Mean Ocean Water (V-SMOW) standard, using a $\delta^{18}O$ value of 9.6‰ for NBS-28 (quartz) for the mass spectrometer calibration. Long-term reproducibility for repeated determination of reference samples was better than ±0.2‰ (1σ).

To quantify the stable isotope relative ratio between the analyzed samples and the standard, the delta (δ) notation:

$$\delta^{18}O = (R_{sample} - R_{std}/R_{std})\ x\ 1000 = (R_{sample}R_{std} - 1)\ x\ 1000\ (‰) \quad (4)$$

where R is the isotopic ratio of concentrations between the rare and abundant molecules for each element for the oxygen R = ^{18}O / ^{16}O. The isotopic composition of carbonates has values $\delta^{18}O_{cal}$ vs SMOW= 26-34 ‰ in marine Limestone, -7 ‰ in meteoric water (Minissale, 2004), from 9 to 17 ‰ in brine and connate marine (Shah et al., 2012; Veigas et al., 2018).

The oxygen isotope composition of carbonate is function of the isotope composition and temperature of the water in which the carbonate minerals were precipitated (Boggs, 2009). This relationship is determined by:

$$T\ (°C) = 16.9 - 4.2\ (\delta_c - \delta_w) + 0.13\ (\delta_c - \delta_w)^2 \quad (5)$$

where δ_c is the equilibrium oxygen isotope composition of calcite; δ_w is the oxygen composition of the water from which the calcite was precipitated. Hence, the oxygen isotope composition become more negative as the burial depth and temperature increase. If one assumes, that the diagenetic fluids for the calcite veins only consist of original seawater, using equation 7, the result of calculation of the temperature of the calcite veins would be around 52.3 to 53.2 °C, when given a $\delta^{18}O$ value of -5 to -6 ‰ PDB. This indicates that the diagenetic fluids from which calcite was precipitated could have more negative oxygen isotope composition, and ^{18}O-depleted water constituent. The mixing of seawater and isotopically light meteoric waters would affect the overall $\delta^{18}O$ signatures of the

calcite precipitation (Fig.2.3). There are two references scales for oxygen, the SMOW and PDB scale. The value of PDB on the SMOW scale (or VPDB on the VSMOW scale) is 30.91‰. In order to convert a $\delta^{18}O$ value from the SMOW to PDB scale the equation is used (Sharp, 2017):

$$\delta\ ^{18}O_{SMOW} = 1.03091 \times \delta\ ^{18}O_{PDB} + 30.91 \quad (6)$$

The $\delta^{18}O$ of tectonic carbonates reflects fractionation processes and depends on the $\delta^{18}O$, and temperature of the fluid; the $\delta^{18}O$ of tectonic carbonates provide also, an overall view of the fluid source, although the temperature-dependent fractionation requires to constrain the fluid temperature.

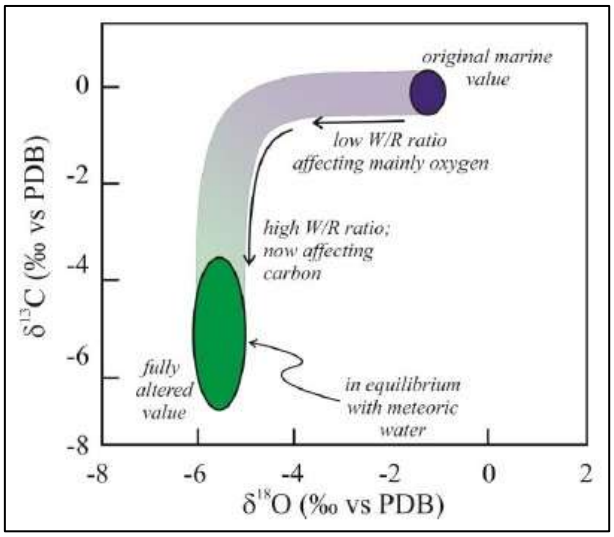

Fig.2.3 *Illustration of changes in $\delta^{18}O$ and $\delta^{13}C$ that accompany alteration of a marine carbonate by meteoric water. Initial dissolution and reprecipitation by interaction with pore water fluids with a small meteoric component will shift carbonate to lower $\delta^{18}O$ values but leave $\delta^{13}C$ values relatively unchanged (point 1). Only after W/R ratio become very large will $\delta^{13}C$ value decrease. The vertical line defined by increasing W/R interaction is the "meteoric calcite line", which defines the $\delta^{18}O$ value of meteoric water responsible for precipitation of late calcite cements (Sharp, 2017 and reference therein).*

Furthermore, combining the values of $\delta\ ^{13}C_{calcite}$ with the $\delta^{18}O_{calcite}$ (Fig. 2.4) can be investigate the main isotopic field for a different representative fluid (pore and/or deep water, seawater, meteoric water) and rock types (marine carbonate, metamorphic rocks, freshwater carbonates).

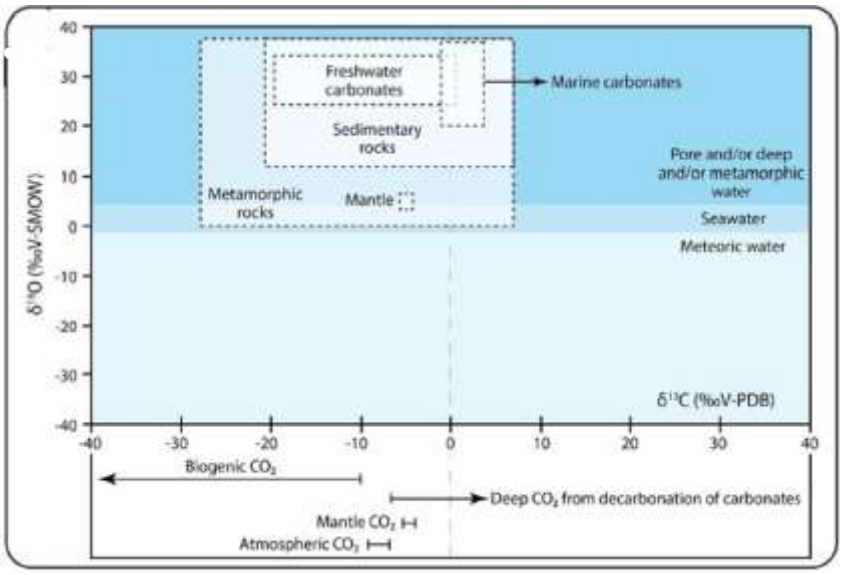

Fig. 2.4 *Reference $\delta^{18}O$ (V-SMOW) vs. $\delta^{13}C$ (V-PDB) diagram showing the main isotopic field for representative fluids and rock types. Data from Rollinson and Paese (1993), Nelson and Smith (1996), Hoefs (1997), Hayes et al. (2001), Valley et al. (2005), Misra (2012), and Sharp (2017). Cartoon and reference by Curzi et al. (2024).*

2.4 Stable isotopes (δD, $\delta^{18}O$) and water content (H_2O wt%)

The hydrogen isotopic analyses in Fluid Inclusion (FIs) trapped in calcite minerals, described later, we carried out at the Servicio General de Análisis de Isótopos Estables (NUCLEUS - University of Salamanca, Spain). D/H ratio were determined on another SIRA-II mass spectrometer on H_2 gas obtained by reduction over hot depleted-U of the water released by induction heating of samples. A vacuum line (Bigeleisen et al., 1952), following the procedures described by Godfrey (1962) with modifications (Jenkin, 1988), was used for gas extraction. The samples (calcite crystals) were loaded into degassed platinum crucibles that were placed in quartz reaction tubes and heated under vacuum to 125 °C overnight to remove any adsorbed H_2O. Results are reported in δD notation relative to the V-SMOW standard, using a δD = −66.7‰ for NBS-30 (biotite) for the mass spectrometer calibration. The amount of the H_2 recovery is known by a baratron gauge reading, which records/measures the total hydrogen (non-condensables) derived from water according to the ideal gas law. Then, we calculated the water content (% H_2O), as a function of the amount of H_2 obtained and the sample weight (wt%). Long-term reproducibility for repeated determination of reference samples was better than ± 2‰ (1σ). Obtaining D/H values in calcite crystals requires significant amount of gas released from fluid inclusions.

Isotopic analysis on water stable isotopes (atoms of the same element with different number of neutrons and mass) are important tools in geochemistry as traces of water origin, recharge areas, circulation paths, mixing or exchange processes, as well as for the study of the global and local water cycle. The hydrogen (D) and oxygen (^{18}O) water stable isotopes have a larger number of neutrons lends and a larger atomic weight with their corresponding most abundant isotopes (^{1}H and ^{16}O, respectively) which induce measurable physical and chemical effects. During phase changes, such as evaporation and condensation, stable isotopes become enriched in one phase and depleted in the other (isotopic fractionation). Fractionation processes leading to a reservoir isotopic enrichment or depletion are quantified through isotope ratios expressed with respect to a standard.

When studying water stable isotopes, it is important to identify the linear relation between δD and $\delta^{18}O$ meteoric water line, first introduced by (Craig, 1961) for global meteoric waters in the form and defined as Global Meteoric Water Line (GMWL):

$$\delta D = 8\delta^{18}O + 10 \quad (7)$$

With the y-intercept 10 representing the deuterium excess (d-excess). The d-excess may vary locally because it is strictly related to the evaporation conditions. For this reason, regional meteoric water lines have been introduced (e.g., the Mediterranean Water Line (MWL): $\delta D = 8\delta^{18}O + 22$, Gat and Carmi, 1987). Given the high small-scale variability of the evaporation condition and consequently, of the reference meteoric water lines, to increase the accuracy of detailed hydrogeochemical studies, local meteoric water lines (LMWL) are estimated. For the Irpinia region, regional reference water lines are: (a) the Southern Italy Water Line (SIMWL: $\delta D = 6.7\delta^{18}O + 5.7$,

Longinelli and Selmo, 2003); (b) with the Northern Calabria Meteoric Water Line (NCMWL: $\delta D = 6.22\delta^{18}O$ +5.21, Vespasiano et al., 2015).

2.5 Noble gases (He, Ne, Ar) systematics

The noble gases, chemically inert elements (substances characterized by low reactivity, the ability of a substance to interaction with other substances resulting a chemical reaction), they constitute the 18th group of the periodic table according to current nomenclature IUPAC (Fig. 2.5). They are excellent tracers of both the fluids sources and the physical processes within the crust (Pik and Marty, 2009; Kendrick and Burnard, 2013; Caracausi and Paternoster, 2015; Curzi et al., 2022).

Do to their high volatily, they have a strong affinity for the gas phase.

Three large terrestrial reservoirs contribute to the inventory of noble gases in terrestrial fluids:

- ✓ The air in the atmosphere or dissolved in water (ASW);
- ✓ The Earth's crust where radiogenic noble gases are produced by the radioactive decay of elements such as U and Th and K dispersed in the rock matrix and/or in embedded fluids by nucleogenic production.
- ✓ The terrestrial mantle, which has a significantly different signature from other reservoirs due to its high enrichment in ^3He

All of these reservoirs have their own characteristic isotopic signature that allows them to be traced efficiently the relative contribution in the various geological matrices. Noble gases have found great applications as tracers in exploration in hydrogeology, geothermal energy, volcanology, geochemical reservoir management and hydrocarbons, evaluation and monitoring of sites for geological storage of CO_2, origin of paleofluids trapped in fluid inclusions in minerals and rock.

Fig.2.5 *Periodic table of chemical elements; in red box the noble* gases.

Helium (He)

Helium is the second most abundant element in the observable universe, being present in approximately 24 % of the total elemental mass. He in the lightest of noble gases (Ozima and Podosek, 2002 and reference therein). In natural fluids is present with two isotopes, ^{3}He and ^{4}He, with the former being mainly primordial and stored in the mantle, the latter continuously produced by U and Th decay in the Earth interior (Ozima and Podosek, 2002). In stable continental regions, the He flux is dominated by the radiogenic ^{4}He produced in the crust (O'Nions and Oxburgh, 1988). In contrast, the primordial ^{3}He escapes into the atmosphere in tectonically active regions and/or in areas characterized by volcanic activity (Caracausi and Sulli, 2019; O'Nions and Oxburn, 1983; Boles et al., 2015). As such, the He isotopic ratio ($^{3}He/^{4}He$), is a powerful tool for recognizing mantle and crust components in absence of other geological and geochemical evidence (e.g., Caracausi and Sulli, 2019; O'Nions and Oxburg, 1988).

In general, the helium isotope ratio is expressed as R/Ra, where:

$R \approx {}^{3}He/^{4}He$ ratio in the sample

$Ra \approx {}^{3}He/^{4}He$ ratio in the atmosphere = 1.382×10^{-6} (Mabry et al., 2013)

Therefore, the following notation is used to express the helium isotope ratios of any sample:

$$R/Ra \approx ({}^{3}He/^{4}He)_{sample} / ({}^{3}He/^{4}He)_{atmosphere} \quad (8)$$

This ratio is corrected for atmospheric contamination based on the $^{4}He/^{20}Ne$ ratio measured in the sample, using isotope balance formula (Sano and Wakita, 1985):

$$Rc/Ra \approx [(R/Ra) \text{ campione-r}] / (1\text{-r}) \quad (9)$$

where:

Rc/Ra is the correct $^{3}He/^{4}He$ ratio;

$r \approx (^{4}He/^{20}Ne)_{air} / (^{4}He/^{20}Ne)_{sample}$

The study of the $^{3}He/^{4}He$ isotope ratio makes it possible to discriminate the origin of the fluid studied, as the different sources are characterized by a specific value. In the case of helium, there are basically three possible sources (Fig.2.6):

- *Atmosphere*
- *Crust*
- *Mantle*

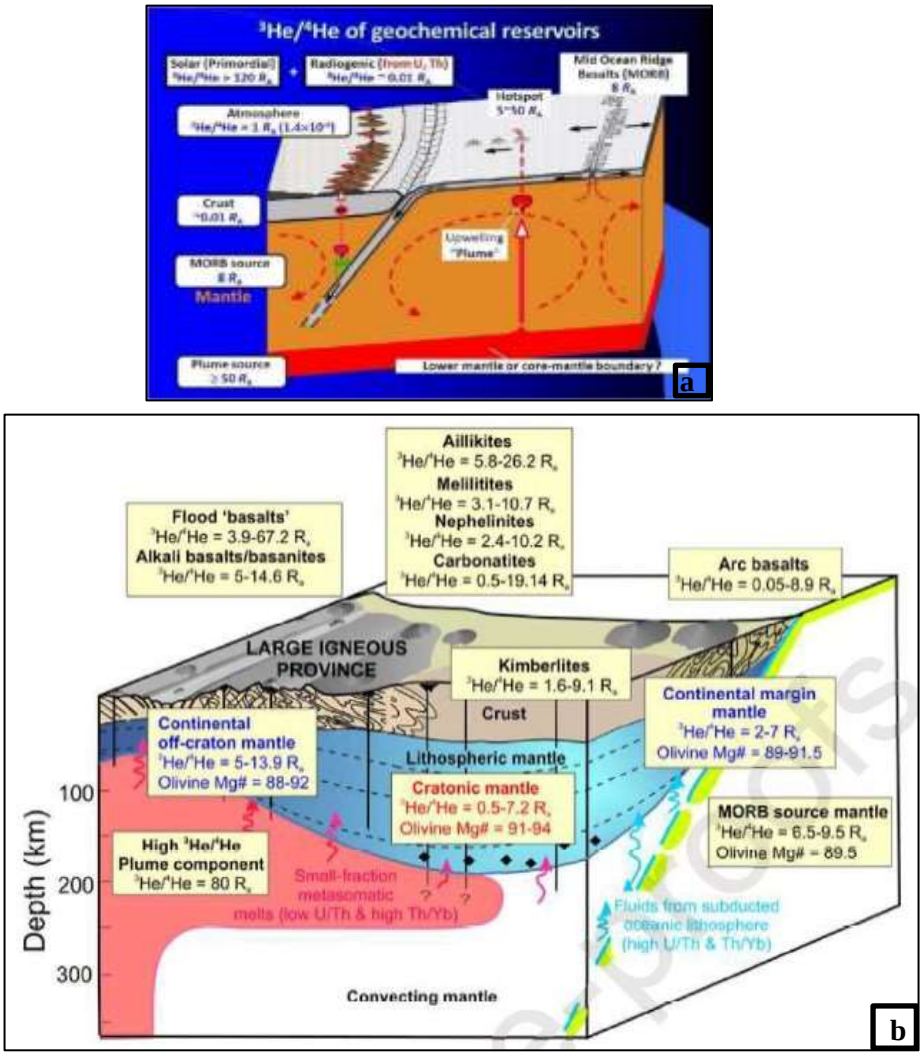

Fig.2.6. ***(a)*** *$^{3}He/^{4}He$ of geochemical reservoirs (Sano and Wakita, 1985);* ***(b)*** *Summary diagram showing variations in $^{3}He/^{4}He$ of the lithospheric mantle at different tectonic settings, based on data from mantle xenoliths presented. The $^{3}He/^{4}He$ of various reservoirs in the convecting mantle are shown for comparison (Gibson et al., 2024, pre-proof).*

Tab.2.1 Helium and Neon isotope values in the atmosphere, Air Satured Water (ASW), Curst and mantle. MORB = Middle Ocean Ridge Basalts; SCLM = Sub Continental Lithospheric Mantle. (Gautheron and Moreira 2005; Ozima and Podosek, 2002; Sano and Wakita, 1985; Mabry et al., 2013; Gibson et al., 2024, pre-proof).

Sources	R/Ra	$^{4}He/^{20}Ne$
Atmosphere	1	0.318
Air Satured water (ASW)	1	0.285
Crust	0.01-0.05	≥ 1000
Mantle (MORB)	7-9	≥ 1000
Mantle (SCLM)	6.1 ± 0.9	≥ 1000

Generally, samples are the result of mixing at least two of this contribution. By means of mass balance and isotope balance, it is possible to understand how these sources have contributed to the isotopic signal of the sample under investigation:

$(He)_{tot} \approx [He]m*Xm+[He]a*(1-Xm)$ (Mass balance) (10)

$(^3He/^4He)_{tot}*[He]_{tot} \approx (^3He/^4He)_m*[He]_m*Xm + (^3He/^4He)_a*[He]_a*(1-Xm)$ (Isotope balance) (11)

"m" and "a" represent the mantle and atmospheric components, while "x" is the mixing fraction of two end members.

Furthermore, based on the production equation of ^4He by U and Th decay (Ballantine and Burnard, 2002 and reference therein):

$$^4He \text{ atoms } g^{-1} yr^{-1} = (3.115 \times 10^6 + 1.272 \times 10^5) [U] + 7.710 \times 10^5 [Th] \quad (12)$$

where [U] and [Th] are the amounts of U and Th respectively (here, assumed both close to 1 ppm, we computed the amount of He produced within 1 gr of calcite (6.66×10^{-18} moles/yr) and we should assume that the ^4He produced in 0.1 Myr per gram of calcite is totally transferred in the FIs.

Neon (Ne)

Neon is the second most abundant noble gas in the atmosphere, after argon, in terms of abundance (18 ppm). In fluid of magmatic origin, however, it is present in quantities of the order of a few ppb. It has three stable isotopes: ^{20}Ne (90,48%), ^{21}Ne (0,27%) and ^{22}Ne (9,25%).

To express relative abundances, neon isotopes are normalized relative to ^{22}Ne (Ozima & Podosek, 1983; Moreira, 2013). In the atmosphere, the theoretical values of these ratios are follows: $^{20}Ne/^{22}Ne = 9.8$, $^{21}Ne/^{22}Ne = 0.029$. In the crustal lithologies, on the other hand, a significant production of nucleogenic neon $^{20}Ne/^{22}Ne = 0.3$; $^{21}Ne/^{22}Ne = 0.47\text{-}0.76$ (Ballantine et al., 2005).

This difference can be exploited to determine the degree of atmospheric contamination that fluids have undergone during ascent. In particular, the ratio $^4He/^{20}Ne$ which in atmosphere (AIR) and air-saturated water (ASW), are 0.319 and 0.285, respectively, at 25°C (Ozima and Podosek, 2002), and in a MORB and/or SCLM is > 1000.

Argon (Ar)

Argon represents up about 0,94% of the Earth's atmosphere and is not very abundant in magmatic fluids (1-10 ppm). It has five isotopes, three of which are stable (^{36}Ar, ^{38}Ar,^{40}Ar) and two unstable (^{37}Ar and ^{39}Ar). The most abundant of these is ^{40}Ar (99,6%), which is mainly derived from the radioactive decay of ^{40}k. Generally, those most studied are the stable ones, the others, however, are mostly used for radiometric dating. The isotope ratios of

argon are usually normalized with respect to ^{36}Ar.

Similar to $^{4}He/^{20}Ne$ ratio, the isotopic ratio $^{40}Ar/^{36}Ar$ is useful for discriminating the atmospheric component in the sample under investigation. The value of this ratio in air is $^{40}Ar/^{36}Ar = 298.6$ (Lee et al., 2006).

Furthermore, in order to compute the amount of deep-sourced ^{40}Ar (due to the ^{40}k decay in the mantle and/or in the crust) it has been used a formula proposed by Graham, (2002):

$$^{40}Ar^* \approx [(^{40}Ar/^{36}Ar)_{sample} * (^{36}Ar)_{sample}]-[(^{40}Ar/^{36}Ar)_{air}*(^{36}Ar)_{sample}] \quad (13)$$

where $(^{40}Ar/^{36}Ar)_{sample}$ and $(^{36}Ar)_{sample}$ are the measured values, and $(^{40}Ar/^{36}Ar)_{air}$ is the aforementioned isotopic value in atmosphere.

In addition to helium isotopes, a comparison of radiogenic helium and radiogenic argon concentrations also provides information on the fluid source. In absence of a preferential leakage of He the ratio between radiogenic crustal ^{4}He and $^{40}Ar^*$ is expected to be similar to the crustal production ($^{40}Ar^*/^{4}He \sim 0.1–0.2$; Kendrick and Burnard, 2013). Alternatively, this ratio can be similar to the mantle production ($^{40}Ar^*/^{4}He \sim 0.1$-1; Curzi et al., 2022 and reference therein).

For this PhD, the noble gases (He, Ne, Ar concentrations and their isotope ratios) in FIs trapped in calcite, were analyzed at the noble gas laboratory of the Istituto Nazionale di Geofisica e Vulcanologia (INGV) in Palermo-Italy, following the preparation and analytical protocols described by Rizzo et al. (2018, 2021). After manually selecting the calcite crystals (ca. 1 g for sample) under a binocular microscope, the separated crystals were thoroughly cleaned in an ultrasonic bath in order to remove any impurities remained attached to their surfaces. The washing process in the ultrasonic bath took 45 minutes and was carried out using Millipore water and acetone. Selected sample materials were loaded into a stainless-steel crusher baked for 48–72 h at 120 °C in order to achieve ultra-high-vacuum conditions (10^{-9} mbar), using procedures described by Tantillo et al. (2009) in INGV Technical Reports. FIs from minerals were released by an in-vacuum single-step crushing processes, with an external pressure of 250 bar applied by a hydraulic press. This conservative procedure was used to minimize the contribution of cosmogenic ^{3}He and radiogenic ^{4}He that might have grown or been trapped in the crystal lattice (Rizzo et al., 2018 and references therein). Each session involved analyzing at least one standard sample for each of He, Ne and Ar with the standards corresponding to purified aliquots of air stored in a tank connected to a pipette with a calibrated volume. The air sample stored in the tank was originally collected close to the sea near to Palermo and then cleaned using standard protocols in the preparation system at the INGV-noble gas laboratory in Palermo. Noble gases were separated from the other volatiles by using a “cold finger” trap immersed in liquid nitrogen (*temperature* = −196 °C) that allows freezing of H_2O and CO_2, and were successively further cleaned in an ultra-high vacuum ($10^{-9} – 10^{-10}$ mbar) purification line, with all species the gas mixture other than noble gases, being removed using four getters. He (^{3}He and ^{4}He) and Ne (^{20}Ne) isotopes were measured separately using two

different split-flight-tube (Helix SFT-Thermo). The analytical uncertainty of the He isotope ratio was ≤ 4%. The ^{20}Ne isotope ratio was corrected for isobaric interferences at *m*/*z* values of 20 ($^{40}Ar^{2+}$). Ar isotopes (^{36}Ar, ^{38}Ar and ^{40}Ar) were analysed using a multicollector mass spectrometer (GVI Argus) with an analytical uncertainty of 1.0%. The uncertainty in the determinations of the elemental contents of He, Ne, and Ar was < 5%.

APPENDICE 3 - FLUID INCLUSIONS (FIs) ANALYSES

3.1 Petrography and microthermometry methodologies

Fluid inclusions (FIs, i.e., small volumes, µm, of paleo-fluids entrapped within host minerals, Fig.3.1), trapped in minerals which provide indispensable information about geological processes, such as: temperature, from high temperature at depth towards low temperature near Earth's surface, composition and time of entrapment and thereby providing direct information about the conditions at which given minerals and rocks are formed.

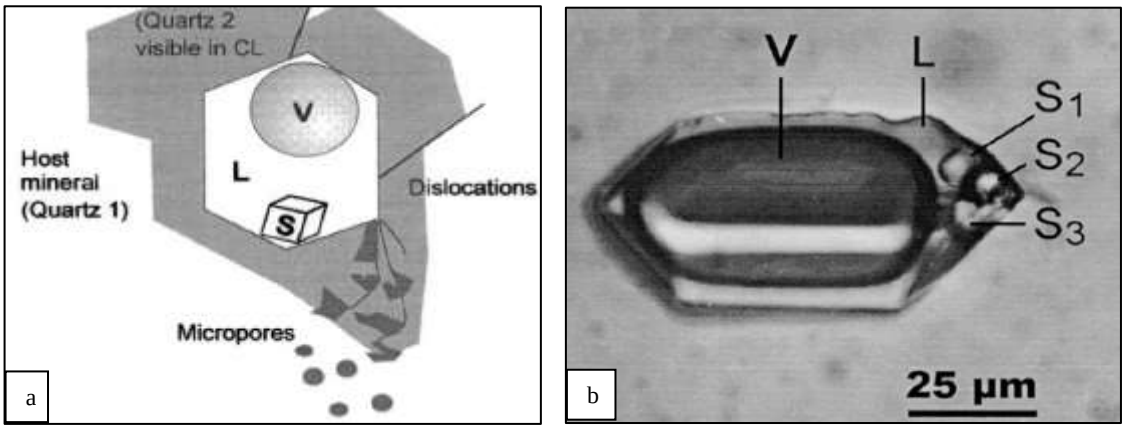

Fig. 3.1 (a) *The integrative fluid inclusion-mineral system. The most important elements in and around a fluid inclusion in quarz are schematically drawn. Fluid inclusions may be surrounded by pure secondary quartz as a result of partial quartz recovery (here: re-crystallization and diffusion);* ***(b)*** *multi-phase fluid inclusion in smoky quartz containing a large bubble (V) of CO_2, saturated salt solution (L) and various daughter phases denoted by S1, S2, and S3 (Van De Jerkhof and Hein, 2001)*

For this PhD study, the petrographic study of FIs was performed on doubly-polished thin sections (60-80 µm think) by using a Leica DM750P polarized optical microscope at 40x and 100x magnification at the University of Salamanca and a Zeiss Axiophot polarizing microscope hosted at the Laboratory of Fluid Inclusions of Sapienza-IGAG-CNR of Rome.

Following the normal protocol of cooling the fluid inclusions to the lowest temperature that the stage can achieve and subsequently observing the phase changes during heating. The stage was cooled with liquid nitrogen and calibrated using a single standard crystal with pure H_2O inclusion. In order to minimize the effect of metastable transformations during cooling, very common in fluids inclusions, melting and homogenization, temperature were determined during heating at the minimum rate (1 °C/min). Densities were firstly calculated on the basis of the equation provided in Sterner and Bodnar and finally corrected according to Hansteen and Klügel (2008). Salinities

were calculated according to Bodnar (1993), while isochore curves were calculated using the software "FLUIDS" (Bakker, 2003). Analytic Procedures and reference can describe by Carnevale et al. (2022). The trapped fluids may be liquid, vapor or supercritical fluid, and the composition of trapped fluid may include assent describe water, brines of various salinity, gas or gas-bearing liquids and silicate or carbonate melts (Roedder, 1984; Bodnar, 1994). FIs occur in different patterns, they are found isolated in a host crystal trapped during initial crystallization or in trail along former microfractures or grain boundaries. The study of abundance, orientation and chemistry of fluid inclusion provides a history of formation and alteration over time, contributing to both fundamental processes in geology (Randive et al., 2014). Important areas of the study include hydrothermal environments, sedimentary environments and diagenetic processes, volcanic areas, mantle environments and tectonic history of deformed areas.

Classification of Fluid Inclusion

There are many ways to classify fluid inclusions, but one of the most useful classification schemes relates the timing of formation of the inclusion relative to that of the host mineral (Bodnar, 2003). Based on their origin, fluid inclusions are of following types (Goldstein, 2003; Randive et al., 2014):

- *Primary:* fluid inclusions which are formed during the formation of the enclosing crystal are primary in origin. They are generally trapped along the growth zones and crystal faces or tends to occur in small cluster and/or isolated inclusions in calcite crystals. These are very good indicators of the condition of crystallization of host minerals.
- *Secondary:* Fluid inclusion which are trapped in the fractures which are developed after the formation of host mineral and caught due healing of fractures. These inclusions occur as trail or clusters which often cut across the grain boundaries.
- *Pseudosecondary:* fluid inclusions which are trapped during formation of the host minerals are referred to as pseudosecondary. These inclusions occur along trail that end abruptly grain boundaries or one of the growth zones.

Depending upon the observed trails in minerals different terminologies used are given below (Fig.3.2):

- *Transgranular:* a trail of fluid inclusions cutting across different minerals grains throughout the rock;
- *Intergranular:* a trail of fluid inclusions crossing the grain boundary and continues into another mineral grain;
- *Intragranular:* A trail of fluid inclusions confined to a particular mineral grain. In such cases the trail of fluid inclusions either, (i) remain confined to the crystal interior, (ii) remain within grain-boundary and crystal interior, or (iii) continues from grain-boundary to grain-boundary;
- *Interphase:* a trail of fluid inclusion starts from one phase and continuous into another phase;
- *Transphase:* a trail of fluid inclusions cutting across different phases.
-

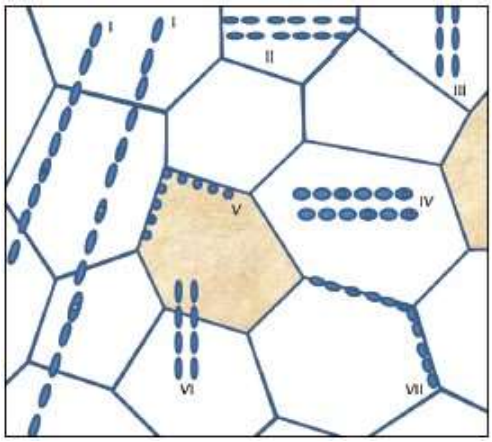

Fig.3.2. *Terminologies used for fluid inclusions (I) Transgranular, (II) Intragranular (grain boundary to grain boundary), (III) Intragranular (grain boundary to crystal interior, (IV) Intragranular (crystal interior), (V) Interphase, (VI) Transphase, and (VII) Intergranular (Randive et al., 2014).*

Modification of fluid inclusions

Originally trapped fluid inclusions are sometimes modified because of several processes subsequent to their trapping. These modifications cause reduction in their volume, change in morphology and often loss of originally trapped fluid. The most important modifications are (Randive et al., 2014; Goldstein, 2003):

- *Recrystallization:* crystallization of fluids and re-crystallization of solids trapped within fluid inclusions can lead to substantial change in the fluid inclusion morphology and lead to the development of negative crystals shapes.
- *Stretching and Necking-down:* necking-down is a typical dissolution-precipitation processes, which finally leads to negative crystal shapes. The phenomenon of necking-down corresponds to the evolution of decreasing temperature.
- *Explosion/implosion Decrepitation:* due to changes in pressure-temperature conditions, large fluid inclusions get busted or decrepitated into smaller inclusions. When pressure increases (overpressure), the decrepitation is said to be "explosion decrepitation".

Microthermometry

The microthermometric study of fluid inclusions is done using a heating and cooling stage, a device that allows increasing or decreasing temperature over a wide range, between -200°C and +1500°C. This stage is placed on a microscope, so that the phase changes occurring as well as the temperature at which these changes taking place can be observed. As a normal working protocol, the fluid inclusions are cooled to the lowest temperature that the stage can achieve and the phase changes taking place are observed while the temperature rises towards room temperature again. The first change of phase that should be observed in the liquid phase is the appearance of the first liquid in the cavity (eutectic temperature) This temperature is characteristic of each system and helps to

associate the composition of the fluid inclusion with a chemical system.

Temperature of Entrapment of Fluid

One the most important aspects of fluid inclusions study is its ability to measure the temperature of entrapment of fluids in the system by direct measurement using microthermometry. In this technique two phases inclusion are heated till they homogenize. The temperature at which homogenization takes place, is the minimum temperature of entrapment of that fluid. If the pressure of system is known, then the temperature of entrapment can be estimated from intersection of isochore passing through the temperature of homogenization.

Salinity of Fluids

Salinity can be measured by observing the depression of the freezing point of the aqueous fluids in the inclusion. The salinity is expressed as NaCl equivalent since, the presence of other ions such as Ca^{2+}, cannot be determined and will greatly influence the salinity estimes. For determination of salinity, the stage is cooled with the help of liquid N_2 during cooling. After the liquid in the inclusion completely solidifies, the stage is heated slowly while the inclusion is observed. The temperature at which the last piece of solid melts (Tm_f) is then recorded. This will correspond to freezing temperatures of the inclusion.

Composition of Fluids

Information about the composition of the fluids can be obtained indirectly by measuring the first melting temperature (Te or Tm_e). After freezing the inclusion, it is heated slowly while being carefully observed under the microscope. The temperature of first melting of solid (ice) is recorded. Comparing this temperature to eutectic melting points on published phase diagrams for binary and ternary system are used to estimate the composition of the fluids.

Acknowledgements

The moment of writing the acknowledgments is extremely intense, because all emotions are transformed into words, and this is certainly not an easy work.

Leaving from the hot city of Palermo, to go to the city of Potenza, without hardly knowing where the city was, leaving home, family, affections and friends was not an easy moment. The PhD is a journey, it is that phase of life between student and professor. During this journey, I have had to come to terms with many of my limitations and impulsive attitudes, and in some cases, it may be that I have learned to overcome them. If I did, it must certainly have been thanks to the people who stood by me throughout the adventure, but also thanks to all the 'wayfarers' with whom I shared short stretches of the path. All those who ultimately gave me a part of themselves and who, in turn, agreed to receive a part of me in return.

Firstly, I would like to thank my tutor Professor Michele Paternoster, the person who gave me the opportunity to go through this course of study, a scientific guide, a person with a strong character, but very empathetic with me, both in criticism and congratulations when things were going well. A person who helped me grow both in character and professionally.

One of the most beautiful "discoveries" that has positively changed my career is certainly my co-tutor Dott. Antonio Caracausi. I learned many qualities from him, such as the scientific rigor, teamwork, passion for everything, and he really puts a lot of it into all his works. Not only a tutor for me, but also a greater friend. During the months I spent in Salamanca (Spain), I had the opportunity to work with him a lot, learning every single word he said to me between departments and between a cerveza and a Spanish meat meal. A person, a researcher with a great passion and dedication for his work and a great aptitude for following young people to get them interested in the world of research with a critical spirit.

I thank Professor Fabrizio Agosta, who passed on notions of structural geology, unknown to me before I started my PhD, and academic and other advice on the many occasions we spoke about our mutual passions. I have great respect for him both academically and personally.

I thank Antonio M. Álvarez-Valero who kindly hosted me in his département, stable isotope laboratory and allowed me to learn a new analysis technique.

Specially, I want to thank my parents who, with their help, support and great sacrifices over all these years, allowed me to study, and shape me both as a student and as a MAN. Sometimes they neglected themselves so that I could go on to achieve my goals. A simple but profound THANK YOU, to them I owe everything. I hope I have made you proud.

Other thanks go to a person who slowly came into my life... a girl met so casually, in the middle of making arancine that over time, knowledge turned into a real feeling, complicity, love. A little girl, with a big heart and character almost as big as they would say in Palermo 'Corna dura". We have had happy moments alternated with nervous

moments from overwork. To trips together around Italy and Spain, to moments when I was already asleep at 9 p.m. because I was too tired.
To trips together around Italy and Spain, to moments when I was already asleep at 9 p.m. because I was too tired. I don't know what paths we will take in the future and/or what life will hold in store for us, whether we will still be together, whether we will build a family or what, but I would like to say that at least these two years spent together with you have been less grey, more colourful and more cheerful. So, a big thank you goes to Antonella.
I would like to thank my PhD colleagues: Canio, Ian, Fabio, Giammarco, Antonio Polo and especially Gabriele Carnevale, companions in adventures, sampling, discussions on different work topics and lots of laughs.
Special thanks, for good reason, go to a master student, Carmela, a sweet, warm-hearted but at the same time fragile girl, and to the whole Geobas association.
A special thanks to all the guys/girls I met during my way here in Potenza: Donato, Silvia, Antonio 'Cugi', Pino, Claudia, Vincenzo, Liuk, Carmine Cisullo. I hope I took something from each of you and left a little part of me.
Finally, thanks go to my lifelong friends who, despite the distance, by phone or when I came home, never let me lack their advice, their support and great evenings of joy and carefreeness. Thanks to Michele, Schirò, Domenico, Lino, Andrea, Attilio, Samuela, Giovanni, Federica, Francesco, Ferdinando, Alberto, Giusy, Ciccio, Naomi, and the entire Mentor association of which I am part. All of you, represent, family, friends, home. Thanks for everything.

"Look wide, and even when you think you are looking wide – look wider still". **Robert Baden-Powell**

References

Agosta, F., Kirschner, D. L. (2003). Fluid conduits in carbonate-hosted seismogenic normal fault of central Italy. *Journal of Geophysical Research, 108, B4, 2221.* doi:10.1029/2002JB002013

Agosta, F., Aydin, A. (2006). Architecture and deformation mechanism of a basin-bounding normal fault in Mesozoic platform carbonates, central Italy. *Journal of Structural Geology 28, 8, 1445–1467.*

Agosta, F., Alessandroni, M., Tondi, E., Aydin, A. (2009). Oblique normal faulting along the northern edge of the Majella Anticline, central Italy: Inferences on hydrocarbon migration and accumulation. *Journal of Structural Geology, 32, 9, 1327-1333.* doi: 10.1016/j.jsg.2010.10.007

Aldega, L., Corrado, S., Giampaolo, C., Mazzoli, S., 2003. Studio della mineralogia delle argille per la ricostruzione dei carichi tettonico/sedimentari; esempi dalle Unita Lagonegresi e Liguridi della Lucania sud-occidentale (Appennino Meridionale). *Bollettino della Societa geologica italiana 122 (2), 203–216.*

Amoroso, O., Russo, G., De Landro, G., Zollo, A., Garambois, S., Mazzoli, S., Parente, M., & Virieux, J. (2017). From velocity and attenuation tomography to rock physical modeling: Inferences on fluid-driven earthquake processes at the Irpinia fault system in southern Italy. *Geophysical Research Letters, 44, 6752–6760.* https://doi.org/10.1002/2016GL072346

Amoroso, O., Ascione, A., Mazzoli, S., Virieux, J., Zollo, A. (2014). Seismic imaging of a fluid storage in the actively extending Apennine Mountain belt, southern Italy. *Geophysical Research Letters, 41, 3802–3809.* https://doi.org/10.1002/2014GL060070

Ascione, A., Mazzoli, S., Petrosino, P., Valenti, E. (2013). A decoupled kinematic model for active normal faults: Insights from the 1980, MS = 6.9 Irpinia earthquake, southern Italy. *Geological Society of America Bulletin, 125, no7/8 p. 1239–1259. 125.* https://doi.org/10.1130/B30814.1

Ballentine, C. J., Burgess, R., Marty, B. (2002). Tracing fluid origin, transport and interaction in the crust. *Reviews in Mineralogy and Geochemistry, 47(1), 539–614.* https://doi.org/10.2138/rmg.2002.47.13

Ballantine, C. J., and Burnard, P. G. (2002). Production, Release, and transport of noble gases in the continentalcrust. *Reviews in Mineralogy and Geochemistry, 47(1), 481-538.* DOI: 10.2138/rmg.2002.47.12

Balsamo, F., Clemenzi, L., Storti, F., Mozafari, M., Solum, J., Swennen, R., Taberner, C., Tueckmantel, C. (2016). Anatomy and Paleofluids evolution of laterally restricted extensional fault zones in the Jabal Qusaybah anticline, Salakh arch, Oman. *The Geological Society of America, 128, 957-972.* Doi: 10.1130/B31317.1

Barberio, M.D., Barbieri, M., Billi, A., Doglioni, C., Petitta, M. (2017). Hydrogeochemical changes before and during the 2016 Amatrice-Norcia seismic sequence (central Italy). *Sci. Rep.7, 11735.* https://doi .org /10 .1038 /s41598 -017 -11990 -8.

Bauer, S. J., Gardner, W. P., Heath, J. E. (2016). Helium release during shale deformation: Experimental

validation. *Geochem. Geophys. Geosystems 17, 2612–2622.* DOI: 10.1002/2016GC006352 (2016b).

Bello, S., De Nardis, R., Scarpa, R., Bozzetti, F., Cirillo, D., Ferrarini, F., Di Lieto, B., Arrowsmith, R. J., Lavecchia, G. (2021). Fault Pattern and seismotectonic style of the Campania-Lucania 1980 earthquake (Mw 6.9, southern Italy): New multidisciplinary constrains. Frontier in earth Science,8. Doi: 10.3389/feart.2020.608063

Bernard, P., and Zollo, A. (1989). The Irpinia (Italy) 1980 Earthquake: Detailed Analysis of a Complex Normal Faulting. *Journal of Geophysical of Research 94, B2, 1631-1647.* https://doi.org/10.1029/JB094iB02p01631

Bigeleisen, J., Perlman, M.L., Prosser, H.C. (1952). Conversion of hydrogenic materials to hydrogen for isotopic analysis. *Anal. Chem. 24, 1536–1537.*

Billi, A., Smeraglia, L., Aldega, L., Balsamo, F., Barberio, M. D., Boschi, C., Caracausi, A., Carminati, E., Iannace, A., Mercuri, M., Pizzati, M., Tavani, S. (2023). Dolostone pulverization induced by coseismic rapid decompression of CO2-rich gas in nature (Matese, Apennines, Italy). *Earth and Planetary Science Letters, 604, 117996.*

Bodnar RJ (2003). Reequilibration of fluid inclusions. In I. Samson, A. Anderson, & D. Marshall, eds. Fluid Inclusions: Analysis and Interpretation. *Mineral. Assoc. Canada, Short Course 32, 213-230.*

Bodnar, R.J. y Vityk, M.O (1994). In: Fluid Inclusions in Minerals: Methods and Applications *(B. De Vivo and M.L.Frezzotti, Eds.). Blacksburg, VA, 117-130.*

Boles, J. R., Garven, G., Camacho, H., Lupton, J. E. (2015). Mantle helium along the Newport-Inglewood fault zone. *Geochemistry, Geophysics, Geosystems, 16, 2364-2381.* DOI: 10.1002/2015GC005951

Bons, P. D. (2000). The formation of veins and their microstructures. In: Stress, Strain and Structure, *A volume in honour of W D Means. Eds: M.W. Jessell and J.L.Urai. Volume 2, Journal of the Virtual Explorer*

Bons, P. D., Elburg, M. A., Rivas, E. G. (2012). A review of the formation of the tectonic veins and their microstructures. *Journal of Structural Geology, 43, 33-62.* http://dx.doi.org/10.1016/j.jsg.2012.07.005

Bons, P, D., Cao, D., De Riese, T., Gonzalez-Esvertit, E., Koehn, D., Naaman, I., Sachau, T., Tian,H., Gomez-Rivas, E. (2022). A review of natural hydrofractures in rocks. *Geological Megazine, 159,1952-1977.* DOI:10.1017/S0016756822001042

Boncio, P., Mancini, T., Lavecchia, G., Selvaggi, G., 2007. Seismotectonics of strike–slip earthquakes within the deep crust of southern Italy: geometry, kinematics, stress field and crustal rheology of the Potenza 1990–1991 seismic sequences (Mmax 5.7). *Tectonophysics 445, 281–300.* https://doi.org/10.1016/j.tecto.2007.08.016.

Borthwick, J., Harmon, R.S. (1982). A note regarding ClF3 as an alternative to BrF5 for oxygen isotope analysis. *Geochim. Cosmochim. Acta 46, 1665–1668.*

Boullier, A.M., Fujimoto, K., Ohtani, T., Roman-Ross, G., Lewin, E., Ito, H., Pezard, P., Ildefonse, B. (2004). Textural evidence for recent co-seismic circulation of fluids in the Nojima fault zone, Awaji island, Japan. *Tectonophysics378, 165–181.* DOI: 10.1016/j.tecto 2012.01.026

Burkhard, M (1992). Calcite twins, their geometry, appearance and significance as stress-strain markers and indicators of tectonic regime: a review. *Journal of Structural Geology, 15,* 3-5, 351 to 368

Burnard, P. G., Hu, R. Z., Turner, G., Bi, X. W. (1999). Mantle, crustal and atmospheric noble gases in Ailaoshan gold deposits, Yunnan Province, China. *Geochimica et Cosmochimica Acta, 63(10), 1595–1604.* https://doi.org/10.1016/S0016-7037(99)00108-8

Buttitta, D., Caracausi, A., Chiaraluce, L. et al. (2020). Continental degassing of helium in an active tectonic setting (northern Italy): the role of seismicity. *Scientific Reports 10, 162*. https://doi.org/10.1038/s41598-019-55678-7

Buttitta, D., Capasso, G., Paternoster, M., Barberio, M. D., Gori, F., Petitta, M., Picozzi, M., Caracausi, A. (2023). Regulation of deep carbon degassing by gas-rock-water interactions in a seismic region of Southern Italy. *Science of the Total Environment, 897.* https://doi.org/10.1016/j.scitotenv.2023.165367

Caracausi, A., M. Martelli., Nuccio, P. M., Paternoster, M. (2013). Active degassing of mantle-derived fluid: A geochemical study along the Vulture line, southern Apennines (Italy), J. Volcanol. Geotherm. Res., 253, 65–74.

Caracausi, A., and Paternoster, M. (2015). Radiogenic helium degassing and rock fracturing: A case study of the southern Apennines active tectonic region. *Journal of Geophysical Research: Solid Earth. 120, 2200–2211*. https://doi.org/10.1002/2014JB011462

Caracausi, A., Buttitta, D., Picozzi, M., Paternoster, M., Stabile T. A. (2022). Earthquakes control the impulsive nature of crustal helium degassing to the atmosphere. *Communications earth & environment 3, 224.* DOI: 10.1038/s43247-022-00549-9

Caracausi, A, and Sulli, A. (2019). Outgassing of mantle volatiles in compressional Tectonic regime away from volcanism: The role of Continental delamination. *Geochemistry, Geophysics, Geosystems 20, 2007–2020.* https://doi.org/10.1029/2018GC008046

Caracausi, A., Favara, R., Italiano, F., Nuccio, P. M., Paonita, A., Rizzo, A. (2005). Active geodynamics of the central Mediterranean Sea: Tensional tectonic evidence in western Sicily from mantle-derived helium. *Geophysical Research Letters, 32, L04312.* https://doi.org/10.1029/2004GL021608

Carnevale, G., Caracausi, A., Correale, A., Italiano, L., Rotolo, S. G (2021). An Overview of the Geochemical Characteristics of Oceanic carbonatites: New Insights from Fuerteventura Carbonatites (Canary Island). *Minerals, 11, 203.* https://doi.org/10.3390/min11020203

Celico, F., Petrella, E., Celico, P. (2006). Hydrogeological behaviour of some fault zones in a carbonate aquifer

of Southern Italy: an experimentally based model. Terra Nova 18 (5), 308–313.

Celico, P., Civita, M. (1976). Sulla tettonica del Massiccio del Cervialto (Campania) e le implicazioni idrogeologiche ad essa connesse. Boll. Soc. Natur. in Napoli 85, 555–580.

Ciotoli, G., Bigi, S., Tartarello, C., Sacco, P., Lombardi, S., Ascione, A., Mazzoli, S. (2013). Soil gas distribution in the main coseismic surface rupture zone of the 1980, Ms = 6.9, Irpinia earthquake (southern Italy). *Journal of Geophysical Research: Solid Earth 119, 2440–2461.* Doi:10.1002/ 2013JB010508.

Chiodini, G., Cardellini, C., Amato, A., Boschi, E., Caliro, S., Frondini, F., Ventura, G. (2004). Carbon dioxide Earth degassing and seismogenesis in Central and southern Italy. *Geophisical Research Letters, 31, L07615*. doi:10.1029/2004GL019480, 2004

Chiodini, G., Granieri, D., Avino, R., Caliro, S., Costa, A., Minopoli, C., Vilardo, G. (2010). Non-volcanic CO_2 Earth degassing: Case of Mefite d'Ansanto (southern Apennines), Italy. *Geophysical Research Letters, 37, 303.* https://doi.org/10.1029/2010GL042858

Chiodini, G., Cardellini, C., Di Luccio, D., Selva, J., Frondini, F., Caliro, S., Rosiello, A., Beddini, G., Ventura, G. (2020). Correlation between tectonic CO_2 Earth degassing and seismicity is revealed by a 10-year record in the Apennines, Italy. *Science Advances, 6, 35.* DOI: 10.1126/sciadv.abc2938

Chi, G., Diamond, L. W., Lu, H., Lai, J., Chu, H. (2021). Common problems and Pitfall in fluid Inclusion Study: A Review and discussion. *Minerals*, *11*(1), 7; https://doi.org/10.3390/min11010007

Ciarcia, S., Vitale, S., DI Staso, A., Iannace, A., Mazzoli, S., Torre, M. (2009). Stratigraphy and tectonics of an Internal Unit of the southern Appennines: implications for the geodynamic evolution of the peri-Tyrrhenian Mountain belt. Terra Nova, 21, 88-96. DOI: 10.1111/j.1365-3121.2008. 00859.x

Ciotoli, G., S. Bigi, C. Tartarello, P. Sacco, S. Lombardi, A. Ascione, and S. Mazzoli. (2014). Soil gas distribution in the main coseismic surface rupture zone of the 1980, Ms = 6.9, Irpinia earthquake (southern Italy). *J. Geophys. Res. Solid Earth, 119, 2440–2461.* DOI: 10.10002/2013JB010508

Clayton, R.N., Mayeda, T.K. (1963). The use of bromine pentafluoride in the extraction of oxygen from oxides and silicates for isotopic analysis. *Geochim. Cosmochim. Acta 27, 43–52.*

Collettini, C., Carpenter, B.M., Viti, C., Cruciani, F., Mollo, S., Tesei, T., Trippett, F., Valoroso, L., Chiaraluce, L. (2014). Fault structure and slip localization in carbonate-bearing normal faults: an example from the Northern Apennines of Italy. *J. Struct. Geol.67, 154–166.* https://doi .org /10 .1016 /j .jsg .2014 .07.017.

Coltorti, M., Boraso, R., Mantovani, F., et al. (2011). U and Th content in the Central Apennines continental crust: A contribution to the determination of the geo-neutrinos flux at LNGS. *Geochimica et Cosmochimica Acta, 7, 9, 2271-2294.* https://doi.org/10.1016/j.gca.2011.01.024

Coppola, L., and Pescatore, T. (1989). Lineamenti di neotettonica dei Monti Terminio-Tuoro, Cervialto e Marzano (Appennino meridionale). *Italian Journal of Geosciences, 108,105-119*

Coppola, M., Correale, A., Barberio, M.D., Billi, A., Cavallo, A., Fondriest, M., Nazzari, M., Paonita, A., Romano, C., Stagno, V., Viti, C., & Vona, A. (2021). Meso- to nano-scale evidence of fluid-assisted co-seismic slip along the normal Mt. Morrone Fault, Italy: Implications for earthquake hydrogeochemical precursors. *Earth and Planetary Science Letters 568.*

Corniello, A., Ducci, D., Aquino, A. (2010). Hydrogeological map of the Monti Picentini Regional Park (southern Italy) at 1: 50,000 scale. *Bollettino Geofisica Teorica ed Applicata 51 (4).*

Corrado, S., Aldega, L., Di Leo, P., Giampaolo, C., Invernizzi, C., Mazzoli, S., Zattin, M., 2005. Thermal maturity of the axial zone of the Southern Apennines fold-and thrust- belt (Italy) from multiple organic and inorganic indicators. *Terra Nova 17 (1), 56–65.* https://doi.org/10.1111/j.1365-3121.2004.00584.x.

Cox, S.F. (1995). Faulting processes at high fluid pressures: an example of fault valve behavior from the Wattle Gully Fault, Victoria, Australia. *J. Geophys. Res.100, 12841–12859.*

Craig, H., (1961). Isotopic Variations in Meteoric Waters. *Science 133, 1702–1703.* https://doi.org/10.1126/science.133.3465.1702

Curzi, M., Caracausi, A., Rossetti, F., Rabiee, A., Billi, A., Carminati, E., Aldega, L., Bernasconi., S. M., Boschi, C., Drivenes, K., Rizzo, A. L., Sorensen, B. E. (2022). From Fossil to Active Hydrothermal Outflow in the Back-Arc of the Central Apennines (Zannone Island, Italy). *Geochemistry, Geophysics, Geosystems, 23.* https://doi.org/10.1029/2022GC010474

Curzi, M., Aldega, L., Billi, A., Boschi, C., Carminati, E., Vignaroli, G., Viola, G., Bernasconi, S. M. (2024). Fossilchemical-physical (dis)equilibria between paleofluids and host rocks and their relationship to the seismiccycle and earthquakes. *Pre-proof Earth-Science Revieews.* https://doi.org/10.1016/j.earscirev.2024.104801

D'Agostino, N., Silverii, F., Amoroso, O., Convertito, V., Fiorillo, F., Ventafridda, G., Zollo, A. (2018). Crustal deformation and seismicity modulated by groundwater recharge of karst aquifers. *Geophysics Research Letters 45, 12,253–12,262.* DOI: 10.1029/2018g1079794

De Landro, G., Amoroso, O., Russo, G., D'Agostino, N., Esposito, R., Emolo, A., Zollo, A., 2022. Author correction: decade-long monitoring of seismic velocity changes at the Irpinia fault system (southern Italy) reveals pore pressure pulsations. *Scientific Reports 12, 16039.* DOI: 10.1038/s41598-022-20912-2

De Matteis, R., Matrullo, E., Rivera, L., Stabile, T. A., Pasquale, G., Zollo, A. (2012). Fault delineation and regional Stress Direction from the Analyses of background microseismicity in the southern Apennines, Italy. *Bulletin of the Seismological Society of America, 102, 1899-1907.* https://doi.org/10.1785/0120110225

Deines, P., (2004). Carbon isotope effects in carbonate systems. *Geochim. Cosmochim. Acta 68, 2659–2679.* https://doi.org/10.1016/j.gca.2003.12.002.

De Astis, G., Kempton, P. D., Peccerillo, A., Wu, T.W. (2006). Trace element and isotopic variations from Mt. Vulture to Campanian volcanoes: contstrain for slab detachment and mantle inflow beneath southern Italy. Contrib Mineral Petrol (2006) 151: 331–351 DOI 10.1007/s00410-006-0062-y

Di Luccio, F., Ventura, G., Di Giovambattista, R., Piscini, A., Cinti, F. R. (2010). Normal faults and thrusts reactivated by deep fluids: the 6 April 2009 Mw 6.3 L'Aquila earthquake, central Italy. *J. Geophys. Res.115.* DOI: 10.1029/2009jB007190

Di Luccio, F., Chiodini, G., Caliro, S., Cardellini, C., Convertito, V., Pino, N.A., Tolomei, C., Ventura, G. (2018). Seismic signature of active intrusions in mountain chains. *Sci. Adv. 4, e1701825.* https://doi.org/10.1126/sciadv.1701825

Doan, M. L., & d'Hour, V. (2012). Effect of initial damage on rock pulverization along faults. *Journal of Structural Geology, 45*, 113-124.

Dogan, T., Sumino, H., Nagao, K., Notsu, K., Tuncer, M. K., Celik, C. (2009). Adjacent releases of mantle helium and soil CO_2 from active faults: Observations from the Marmara region of the North Anatolian Fault zone, Turkey. *Geochemistry, Geophysics, Geosystems, 10.* https://doi.org/10.1029/ 2009GC002745

Doglioni, C., Harabaglia, P., Martinelli, G., Mongelli, F., & Zito, G. (1996). A Geodinamic model of the southern Appenines accretionary prism. *Terra Nova, 8, 540-547.* DOI: 10.1111/j.1365-3121.1996.tb00783.x

Doglioni C., Barba S., Carminati E., & Riguzzi F. (2013). Fault on-off versus coseismic fluids reaction, *Geoscience frontiers, 5(6*), 767-780. http://dx.doi.org/10.1016/j.gsf.2013.08.004.

Drever, J.I., 1997. The geochemistry of natural waters: surface and groundwater environments, 3rd edn. Prentice Hall, Upper Saddle River.

Falcone, R.A., Carucci, V., Falgiani, A., Manetta, M., Parisse, B., Petitta, M., Rusi, S., Spizzico, M., Tallini, M. (2012). Changes on groundwater flow and hydrochem-istry of the Gran Sasso carbonate aquifer after 2009 L'Aquila earthquake. *Ital. J. Geosci.131 (3), 459–474*. https://doi .org /10 .3301 /IJG .2011.34.

Ferraro, F., Agosta, F., Prasad, M., Vinciguerra, S., Violay, M., Giorgioni, M. (2020). Pore space properties in carbonate fault rocks of peninsular Italy. *Journal of Structural Geology, 130.* https://doi.org/10.1016/j.jsg.2019.103913

Faulkner, D. R., Armitage, P. J. (2013). The effect of tectonic environment on permeability development around faults and in the brittle crust. *Earth and Planetary Science Letters, 375, 71-77.* https://doi.org/10.1016/j.epsl.2013.05.006

Ferril, D.A., Morris, A, P., Evans, M.A., Burkhard, M., Groshong, R, H., Onasch, C, M. (2004). Calcite twin morphology: a low-temperature deformation geothermometer. *Journal of structural Journal 2,6 1521-1529. doi:10.1016/j.jsg.2003.11.028*

Frondini, F., Cardellini, C., Caliro, S., Beddini, G., Rosiello, A., Chiodini, G. (2019). Measuring and interpreting CO2 fluxes at regional scale: the case of the Apennines, Italy. J. Geol. Soc. London 176, 408‑416. https://doi.org/10.1144/jgs2017-169.

Gautheron, C., Moreira, M., & Allegre, C. (2005). He, Ne and Ar composition of the European lithospheric mantle. *Chemical Geology, 217, 97–112.* https://doi.org/10.1016/j.chemgeo.2004.12.009

Gautheron, C. and Moreira, M. (2002). Helium signature of the subcontinental lithospheric mantle. *Earth and Planetary Science Letters, 199, 39-47.* https://doi.org/10.1016/S0012-821X(02)00563-0

Gat, J., Carmi, I. (1987). Effect of climate changes on the precipitation patterns and isotopic composition of water in a climate transition zone: Case of the Eastern Mediterranean Sea area. Proceedings of the Vancouver Symposium 168.

Gibson, S.A, Crosby, J.C., Day, J. A.F, Stuart, F. M., Di Nicola, L., Riley, T. R (2024). Systematic behaviour of $^{3}He/^{4}He$ in Earth's continental mantle. Geochimical et Cosmochimica Acta

Gilfillan, S.M.V., Lollar, B.S., Holland, G., Blagburn, D., Stevens, S., Schoell, M., Cassidy, M., Ding, Z., Zhou, Z., Lacrampe-Couloume, G., Ballentine, C.J. (2009). Solubility trapping in formation water as dominant CO2 sink in natural gas fields. *Nature 458, 614–618*.https://doi.org/10.1038/nature07852.

Giuffrida, A., Agosta, F., Rustichelli, A., Panza, E., La Bruna, V., Eriksson, M., Torrieri, S., Giorgioni, M. (2020). Fracture stratigraphy and DFN modelling of tight carbonates, the case study of the Lower Cretaceous carbonates exposed at the Monte Alpi (Basilicata, Italy). *Marine and Petroleum Geology, 112, 104045*. https://doi.org/10.1016/j.marpetgeo.2019.104045

Godfrey, J.D. (1962). The deuterium content of hydrous minerals from the east-Central Sierra Nevada and Yosemite National Park. *Geochim. Cosmochim. Acta 26, 1215–1245.*

Goldstein, R. H (2003). Petrographic analysis of fluid inclusions, in: Fluid inclusions: Analysis and Interpretation: *Mineralogical Association of Canada, edited by: Samson, I., Anderson, A., and Marshall, D., 1–45.*

Goodwin, N. R., Burgess, R., Craw, D., Teagle, D. A., and Ballentine, C. J. (2017). Noble gases fingerprint a metasedimentary fluid source in the Macraes orogenic gold deposit, New Zealand. *Mineralium Deposita, 52*(2), 197–209. https://doi.org/10.1007/s00126-016-0648-x

Gori, F., Paternoster, M., Barbieri, M., Buttitta, D., Caracausi, A., Parente, F., Sulli, A., Petitta, M. (2023). Hydrogeochemical multi-component approach to assess fluids upwelling and mixing in shallow carbonate-evaporitic aquifers (Contursi area, southern Apennines, Italy). *Journal of Hydrology, 618, 129258.* https://doi.org/10.1016/j.jhydrol.2023.129258

Graham, D. W. (2002). Noble Gas Isotope Geochemistry of Mid-Ocean Ridge and Ocean Island Basalts: Characterization of mantle source reservoirs. *Reviews in mineralogy and geochemistry, 47, 247-317.* DOI: 10.2138/rmg.2002.47.8

Gratier, J. P., and Gamond, J. F. (1990). Transition between seismic and aseismic deformation in the upper crust. *Geological Society of London, 54, 461-473.* https://doi.org/10.1144/GSL.SP.1990.054.01.42

Halford, D.T., Karolytė, R., Barry, P.H., Whyte, C.J., Darrah, T.H., Cuzella, J.J., Sonnenberg, S.A., Ballentine, C. J. (2022). High helium reservoirs in the four corners area of the Colorado Plateau, USA. *Chemical. Geology, 596, 120790.* https://doi.org/10.1016/j.chemgeo.2022.120790

Hancock, P. L. and Barka, A. A. (1987). Kinematic indicators on active normal faults in western Turkey. *Journal of Structural Geology 9, 5/6, 573-584.* DOI: https://doi.org/10.1016/0191-8141(87)90142-8

Haney, M.M., Snieder, R., Sheiman, J., Losh, S. (2005). Geophysics: a moving fluid pulse in a fault zone. *Nature 437, 46.*

Hilgers, C., Dilg-Gruschinski, K., Urai, J.L. (2004). Microstructural evolution of syn-taxial veins formed by advective flow. *Geology 32, 261–264.* https://doi .org /10 .1130 /G20024 .1.

Hoefs, J., (1987). Variations of Stable Isotope Ratios in Nature, in: *Hoefs, J. (Ed.), Stable Isotope Geochemistry, Minerals and Rocks. Springer, Berlin, Heidelberg, pp. 66–197.* https://doi.org/10.1007/978-3-662-09998-8_3

Hoefs, J., 2009. Stable Isotope Geochemistry. 6th ed. Springer Science & Business Media, Berlin, Germany https://doi.org/10.1007/978-3-540-70708-0.

Hoefs, J., 2015. Isotope Fractionation Processes of Selected Elements, in: Hoefs, J. (Ed.), Stable Isotope

Honda, M., Kurita, K., Hamano, Y., Ozima, M. (1982). Experimental studies of He and Ar degassing during rock fracturing. *Earth Planetary Sci. Letters. 59, 429–436,* DOI: 10.1016/0012-821X(82)90144-3

Horita, J., (2014). Oxygen and carbon isotope fractionation in the system dolomite–water–CO2 to elevated temperatures. Geochim. Cosmochim. Acta 129, 111–124. https://doi.org/10. 1016/j.gca.2013.12.027.

Italiano, F., Martelli, M., Martinelli, G., Nuccio, P. M. (2000). Geochemical evidence of melt intrusions along lithospheric faults of the Southern Apennines, Italy Geodynamic and seismogenic implications. *Journal of Geophysical Research 105, B6, 3,569-13,578.* DOI: https://doi.org/10.1029/2000JB900047

Improta, L., De Gori, P., Chiarabba, C. (2014). New insights into crustal structure, Cenozoic magmatism, CO2 degassing, and seismogenesis in the southern Apennines and Irpinia region from local earthquake tomography: seismic tomography of Apennines. J. Geophys. Res. Solid Earth 119, 8283–8311. https://doi.org/10.1002/2013JB010890.

Jenkin, G.R.T., (1988). Stable Isotope Studies in Caledonides of SW Connemara, Ireland. *PhD thesis. Univ. Glasgow, UK.*

Karolytė, R., Johnson, G., Györe, D., Serno, S., Flude, S., Stuart, F.M., Chivas, A.R., Boyce, A., Gilfillan, S.M.V. (2019). Tracing the migration of mantle CO2 in gas fields and mineral water springs in south-East Australia using noble gas and stable isotopes. *Geochim. Cosmochim. Acta 259, 109–128.*

https://doi.org/10.1016/j.gca.2019.06.002

Kendrick, M. A., and Burnard, P. (2013). Noble gases and halogens in fluid inclusions: A journey through the Earth's crust. *In The noble gases as geochemical tracers (pp. 319–369). Springer*. DOI: 10.1007/978-3-642-28836-4_11

Kennedy, B. M., and Van Soest, M. C. (2007). Flow of mantle fluids through the ductile lower crust: Helium isotope trends. *Science, 318 (5855), 1433–1436.* https://doi.org/10.1126/science.1147537

Kim, S.-T., & O'Neil, J.R. (1997). Equilibrium and nonequilibrium oxygen isotope effects in synthetic carbonates. *Geochimica et Cosmochimica Acta 61*, 3461–3475.

Kulongoski, J. T., Hilton, R. D., Barry, P. H., Esser, B. K., Hillegonds, D., Belitz, K. (2013). Volatile fluxes through the big bend section of the San Andreas Fault, California: Helium and carbon-dioxide systematics. *Chemical Geology, 339, 92-102.* DOI: 10.1016/j.chemgeo.2012.09.007

Lacombe, O., Parlangeau, Beaudoin, N., Amrouch, K (2021). Calcite Twins formation, measurement and use as stress-strain indicators: a review of progress over the last decade. *Geosciences, 11, 445 0.3390/geosciences11110445*

Laughrey, C.D., Baldassare, F.J. (2003). Some applications of isotope geochemistry for determining sources of stray carbon dioxide gas. *Environ. Geosci. 10, 107–122*. https://doi.org/10.1306/eg100303003

Lee, J. Y., Marty, K., Severinghaus, J. P., Kawamura, K., Yoo, H.-S., Lee, J. B., & Kim, J. S. (2006). A redetermination of the isotopic abundances of atmospheric Ar. *Geochimica and Cosmochimica acta, 70 (17), 4507-4512.* https://doi.org/10.1016/j.gca.2006.06.1563

Liu, W., Zhang, M., Chen, B., Liu, Y., Cao, C., Xu, W., Zheng, G., Zhou, X., Lang, Y-C., Sano, Y., Xu, S. (2023). Hydrothermal He and CO_2degassing from a Y-shaped active fault system in eastern Tibetan Plateau with implications for seismogenic processes. *Journal of Hydrology, 620, B, 129482.* https://doi.org/10.1016/j.jhydrol.2023.129482

Longinelli, A., Selmo, E. (2003). Isotopic composition of precipitation in Italy: a first overall map. *Journal of Hydrology 270, 75–88.* https://doi.org/10.1016/S0022-1694(02)00281-0

McLennan, S. M (2001). Relationship between the trace element composition of sedimentary rocks and upper continental crust. Geochemistry Geophysics Geosystems, 2

Mabry, J., Lan, T., Burnard, P., & Bernard, M. (2013). High-precision helium isotope measurements in air. *Journal of analytical Atomic Specttrometry, 28, 1903–1910.* DOI: 10.1039/c3ja50155h

Manniello, C.; Abdallah, I. B.; Prosser, G.; Agosta, F. (2023). Pressure Solution-Assisted Diagenesis and Thrusting-Related Deformation of Mesozoic Platform Carbonates. *Journal of structural geology, 173, 104906.* https://doi.org/10.1016/j.jsg.2023.104906

Marchesini, B., Carminati, E., Aldega, L., Mirabella, F., Petrelli, M., Caracausi, A., Barchi, M. R. (2022). Chemical interaction driven by deep fluids in the damage zone of a seismogenic carbonate fault. *Journal of Structural Geology, 161.* https://doi.org/10.1016/j.jsg.2022.104668

Mariucci, M.T., Montone, P. (2020). Database of Italian present-day stress indicators, *IPSI 1.4. Sci. Data 7 (1), 298.* https://doi.org/10.1038/s41597-020-00640-w.

Miller, S. A., Collettini, C., Chiaraluce, L., Cocco, M., Barchi, M., & Kaus, B. J. P. (2004). Aftershocks driven by a high-pressure CO_2 source at depth. *Nature 427, 724-727.* DOI: 10.1038/nature02251

Minissale, A (2004). Origin, transport and discharge of CO_2 in central Italy. *Earth-Science Reviews 66, 89–141* doi:10.1016/j.earscirev.2003.09.001

O'Neil, J. R., Clayton, R. N., & Mayeda, T. K. (1969). Oxygen isotope fractionation in divalent metal carbonates. *The Journal of Chemical Physics, 51(12*), 5547-5558.

O'Nions, R. K and oxburn, E. H. (1983). Heat and helium in the Earth. Nature, 306, 429-431

O'Nions, R. K., and E. R. Oxburgh. (1988). Helium volatile fluxes and the development of continental crust *Earth Planetary. Sci. Letters, 90, 331–347.* DOI: 10.1016/0012-821X(88)90134-3

Ozima, M., & Podosek, F. A. (2002). Noble Gas Geochemistry. *Cambridge University Press.* DOI:10.1017/cbo9780511545986

Nelson, C. S., & Smith, A. M. (1996). Stable oxygen and carbon isotope compositional fields for skeletal and diagenetic components in New Zealand Cenozoic nontropical carbonate sediments and limestones: a synthesis and review. *New Zealand Journal of Geology and Geophysics, 39(1)*, 93-107.

Nuriel, P., Rosenbaum, G., Uysal, I.T., Zhao, J.-X., Golding, S.D., Weinberger, R., Karaba-cak, V., Avni, Y. (2011). Formation of fault-related calcite precipitates and their implications for dating fault activity in the East Anatolian and Dead Sea fault zones. *In: Fagereng, Å., et al., (Eds.), Geology of the Earthquake Source: A Volume in Honour of Rick Sibson. Geol. Soc. (Lond.) Spec. Publ.359, 229–248*. DOI: 10.1144/SP359.13.

Nuriel, P., Weinberger, R., Rosenbaum, G., Golding, S.D., Zhao, J.-X., Uysal, I.T., Bar-Matthews, M., Gross, M.R., 2012. Timing and mechanismof late-Pleistocene calcite vein formation across the Dead Sea Fault Zone, northern Israel. *Journal of Structural Geology 36, 43–54*. DOI:10.1016/j.jsg.2011.12.010

Pik, R., and Marty, B. (2009). Helium isotopic signature of modern and fossil fluids associated with the Corinth rift fault zone (Greece): Implication for fault connectivity in the lower crust. *Chemical Geology, 266, 67-75.* DOI: 10.1016/j.chemgeo.2008.09.024

Patacca, E., and Scandone, P. (2007). Geology of the Southern Appennines. *Bollettini Società Geologica Italiana, 7, 75-119*

Passchier, C. W., and Trouw, R. A. J. (2005). Microtectonic. *Springer Berlin Heidelberg, Berlin, Heidelberg.*

Patacca, E., Sartori, R., Scandone P., 1990. Tyrrenian Basin and Apenninic Arcs: Kinematic relations since late Tortonian times. *Italian Journal of Geosciences, 45, 425-451*.

Petitta, M., Mastrorillo, L., Preziosi, E., Banzato, F., Barberio, M.D., Billi, A., Cambi, C., De Luca, G., Di Carlo, P., Di Curzio, D., Di Salvo, C., Nanni, T., Palpacelli, S., Rusi, S., Saroli, M., Tallini, M., Tazioli, A., Valigi, D., Vivalda, P., Doglioni, C. (2018). Water-table and discharge changes associated with the 2016–2017 seismic sequence in central Italy: hydrogeological data and a conceptual model for fractured carbonate aquifers. *Hydrogeol. J.* https://doi .org /10 .1007 /s10040 -017 -1717 -7.

Picozzi, M., Bindi, D., Festa, G., Cotton, F., Scala, A., D'Agostino, N. (2022). Spatiotemporal evolution of microseismicity seismic source properties at the Irpinia near-fault observatory, southern Italy. *Bull. Seismol. Soc. Am. 112, 226–242.* https://doi.org/10.1785/ 0120210064.

Piper, D.Z., Bau, M. (2013). Normalized Rare Earth Elements in water, sediments, and wine: identifying sources and environmental redox conditions. *Am. J. Anal. Chem. 4, 69–83*.

Pourmand A., Dauphas N., Ireland T.J. (2012). A novel extraction chromatography and MC-ICP-MS technique for rapid analysis of REE, Sc and Y: Revising Cl-chondrite and Post-Archean Australian Shale (PAAS) aboundances. *Chemical Geology, 291, 38-54.*

Ramsay J.G (1980). The crack–seal mechanism of rock deformation. *Nature 284,135–9.*

Randazzo, P., Caracausi, A., Aiuppa, A., Cardellini, C., Chiodini, C., D'Alessandro, W., Li Vigni, L., Papic, P., Marinkovic, G., Ionescu, A. (2021). Active degassing of deeply sourced fluids in central Europe: New evidence from a geochemical study in Serbia. *Geochemistry, Geophysics, Geosystems, 22.* DOI: 10.1029/2021GC010017

Randive, K. R., Hari, K.R., Dora, M. L., Maple, D.B., Bhondwe, A. A. (2014). Study of fluid inclusions: Methods, Techniques and Applications. *Gond. Geol. Mag., V. 29(1 and 2), June and December, 2014. pp.19-28.*

Rielli, A., Boschi, C., & Dini, A. (2022). Tectonically driven carbonation of serpentinite by mantle CO2: genesis of the Castiglioncello magnesite deposit in the Ligurian ophiolite of central Tuscany (Italy). *Ore Geology Reviews, 149, 105022.*

Rizzo, A. L., Pelorosso, B., Coltorti, M., Ntaflos, T., Bonadiman, C., Malek, M. M., Italiano, F., Bergonzoni, G. (2018). Geochemistry of Noble Gases and CO_2 in fluid inclusion from lithospheric mantle Beneath Wilcza Gora (Lower Silesia, Southwest Poland). *Frontiers in earth Sciences, 6:215.* doi: 10.3389/feart.2018.00215

Rizzo, A. L., Faccini, B., Casetta, F., Faccincani, L., Ntaflos, T., Italiano, F., Coltorti, M. (2021). Melting and metasomatism in West Eifel and Siebengebirge Sub Continental Lithospferic Mantle: Evidence from concentrations of volatilies in fluid inclusions and petrology of ultramafic xenoliths. *Chemical geology, 581*. https://doi.org/10.1016/j.chemgeo.2021.120400

Rizzo, A. L., Uysal, I. T., Mutlu, H., Unal-Imer, E., Dirik, K., Yuce, G., Caracausi, A., Italiano, F., Misseri, M., Temel, A., Bayari, S., Ozyurt, N., Zhao, J, X., Deniz, K. (2019). Geochemistry of fluid inclusions in travertines from Western and Northern Turkey: Inferences on the Role of Active faults in fluids circulation. *Geochemistry, Geophysics, Geosystems, 20.* 5473-5498. https://doi.org/10.1029/2019GC008453

Roedder, E. (1984): Fluid Inclusions, Min. Soc. Am. Rev. in Min. v. 12, 646 pp

Roberts, N.M., Holdsworth, R.E. (2022). Timescales of faulting through calcite geochronology: *a review Journal of Structural Geology, 158, 104578.* DOI: 10.1016/j-gsj.2022.104578

Rosatelli, G., Castorina, F., Consalvo, A., Brozzetti, F., Ciavardelli,D., Perna, M. G., Bell, K., Bello, S., Stoppa, F. (2023). Elemental abundances and isotopic composition of Italian limestone: Glimpses into the evolution of Tethys. *Journal of Asian Earth Sciences: X 9, 100136* https://doi.org/10.1016/j.jaesx.2023.100136

Sano, Y., and Wakita, H. (1985). Geographical distribution of $^{3}He/^{4}He$ ratios in Japan: implications for arc tectonics and incipient magmatism. *Journal of Geophysical Research Solid Earth, 90, 8729–8741.*DOI: 10.1029/JB090iB10p08729

Sano, Y., and Marty, B. (1995). Origin of carbon in fumarolic gas from island arcs. *Chemical Geology, 119, 265-274.* DOI: /10.1016/0009-2541(94)00097-R

Sano, Y., Takahata, N., Igarashi, G., Koizumi, N. and Sturchio, N. C. (1998). Helium degassing related to the Kobe earthquake. *Chemical Geology 150, 171–179.* DOI: 10.1016/S0009-2541(98)00055-2

Sano, Y., Takahata, N., Kagoshima, T., Shibada, T., Onoue, T. (2016). Groundwater helium anomaly reflects strain change during the 2016 Kumamoto earthquake in Southwest Japan. *Scientific Reports 6,* DOI: 10.1038/srep37939 (2016).

Schirippa Spagnolo, G., Bernasconi, S. M., Aldega, L., Castorina, F., Billi, A, Smeraglia, L., Agosta, F., Prosser, G., Tavani, S., Carminati, E. (2024). Interplay and feedback between tectonic regime, faulting, sealing horizonts, and fluid flow in a hydrocarbon-hosting extensional basin: The Val D'Agri Basin case, southern Italy. *Earth and Planetary Science Letters 646, 118982.* DOI: 10.1016/j.epsl.2024.118982

Sibson, R.H. (1998). Brittle failure mode plots for compressional and extensional tectonic regimes. *Journal of Structural Geology 20.*

Sibson, R.H., Scott, J. (1998). Stress/fault controls on the containment and release of overpressured fluids: examples from gold±quartz vein systems in Juneau, Alaska, Victoria, Australia, and Otago, New Zealand. *Ore Geology Reviews 13,*

Sibson, R. H. (2000). Fluid involvement in normal faulting. *Journal of Geodynamics 29,469-499.* DOI: 10.1016/S0264-3707(99)00042-3

Sibson, R. H. (1992). Implications of fault-valve behaviour for rupture nucleation and recurrence. Tectonophysics 18, 1031-1042

Sibson, R.H. (2014). Earthquake rupturing in fluid-overpressured crust: how common? *Pure Appl. Geophys.171, 2867–2885.*

Slejko, D., Peruzza, L., Rebez, A. (1998). Seismic hazard maps of Italy. *Annals of Geophysics, 41,2*

Sharp, Z. (2007). Principles of Stable Isotope Geochemistry. Pearson Prentice Hall, p. 344pp.

Sharp, Z.D., 1990. A laser-based microanalytical method for the in-situ determination of oxygen isotope ratios of silicates and oxides. *Geochim. Cosmochim. Acta 54, 1353–1357.*

Shah, S. R., Joye, S.B., Brandes, J., Mcnichol, A. P. (2013). Carbon isotopic evidence for microbial control of carbon supply to Orca basin at the seawater-brine interface. *Biogeosciences Discuss., 9, 17913 – 17937*doi:10.5194/bgd-9-17913-2012

Shiner, P., Beccaccini, A., Mazzoli., S. (2004). Thin-skinned versus thick-skinned structural models for Apulian carbonate reservoir: constraint from the Val d'Agri Fields, S. Appennines, Italy. *Marine and Petrolium Geology,21, 805-827.* https://doi.org/10.1016/j.marpetgeo.2003.11.020

Schauble, E.A., Ghosh, P., Eiler, J.M., 2006. Preferential formation of 13C–18O bonds in carbonate minerals, estimated using first-principles lattice dynamics. *Geochim. Cosmochim. Acta 70, 2510–2529.* https://doi.org/10.1016/j.gca.2006.02.011

Smeraglia, L., Berra. F., Billi, A., Boschi, C., Carminati, E., Doglioni, C. (2016). Origin and role of fluids involved in the seismic cycle of extensional faults in carbonate rocks. *Earth and Planetary Science Letters, 450, 292-305.* DOI: 10.1016/j.epsl.2016.06.042

Smeraglia, L., Bernasconi, S.M., Berra, F., Billi, A., Boschi, C., Caracausi, A., Carminati, E., Castorina, F., Doglioni, C., Italiano, F., Rizzo, A. L., Uysal, I. T., Zhao, J. X. (2018). Crustal-scale fluid circulation and co-seismic shallow comb-veining along the longest normal fault of the central Apennines, Italy. *Earth and Planetary Science Letters 498, 152–168.* DOI: 10.1016/j.epsl.2018.06.013

Smeraglia, L., Fabbri, O., Choulet, F., Jaggi, M., Bernasconi, S. M. (2022). The role of thrust and strike-slipe faults in controlling regional-scale paleofluids circulation in fold-and-thrust belt: Insights from the Jura Mountains (eastern France). *Tectonophysics, 829, 229299.* https://doi.org/10.1016/j.tecto.2022.229299

Stewart, I. S., and Hancock, P. L. (1990). Brecciation and fracturing within neotectonic normal fault zones in the Aegean region. *Geological Society, London, 54, 105 – 110.* DOI: 10.1144/GSL.SP.1990.054.01.11

Tamburello, G., Pondrelli, S., Chiodini, G., Rouwet, D. (2018). Global-scale control of extensional tectonics on CO_2 earth degassing. *Nature Communications 9, 4608.* DOI: 10.1038/s41467-018-07087-z

Tang, Y., Bi, X., Fayek, M., Stuart, F. M., Wu, L., & Jiang, G. (2017). Genesis of the Jinding Zn-Pb deposit, northwest Yunnan Province, China: Constraints from rare Earth elements and noble gas isotopes. *Ore*

Geology Reviews, 90, 970–986. https://doi.org/10.1016/j.oregeorev.2017.04.024

Tantillo, M., Riccobono, G., & Rizzo, A. L. (2009). Sistema di frantumazione minerali e rocce (crusher) per la stima delle concentrazioni elementari ed isotopiche dei gas nobili contenuti nelle inclusioni fluide. *Rapporti tecnici INGV*

Todaro, S., Manniello, C., Pietragalla, A., Preto, N., Agosta, F. (2024). Depositional Setting diagenetic processes, and pressure solution-assisted compaction of Mesozoic Platform carbonate, southern Apennines, Italy. *Geosciences, 14, 89*. https://doi.org/10.3390/geosciences14040089

Torgensen, T. (2010). Continental degassing flux of ^{4}He and its variability. *Geochemistry, Geophysics, Geosystems, 11, 6.* doi:10.1029/2009GC002930

Toscani, L., Boschetti, T., Maffini, M., Barbieri, M., Mucchino, C. (2007). The groundwaters of Fontevivo (Parma Province, Italy): redox processes and mixing with brine waters. *Geochem.: Explor. Environ. Anal. 7 (1), 23–40.*

Tostevin, R., Shields, G. A., Tarbuck, G. M., He, T., Clarkson, M. O., Wood, R. A. (2016). Effective use of cerium anomalies as a redox proxy in carbonate-dominated marine setting. *Chemical Geology 146–162*

Ünal-¨Imer, E., Uysal, I.T., Zhao, J.X., I¸sı, k V., Shulmeister, J., Imer, A., Feng, Y.X. (2016). CO_2 outburst events in relation to seismicity: constraints from microscale geochronology, geochemistry of late Quaternary vein carbonates, SW Turkey. *Geochim. Cosmochim. Acta 187, 21–40.* DOI: 10.1016/j.gca.2016.05.006

Uysal, I.T., Feng, Y.X., Zhao, J.X., Bolhar, R., Is¸ik, V., Baublys, K.A., Yago, A., Golding, S. D. (2011). Seismic cycles recorded in late Quaternary calcite veins: geochronological, geochemical and microstructural evidence. *Earth Planetary Sciences Letters. 303 (1–2), 84–96.* DOI: 10.1016/j.epsl.210.12.039

Van Den Kerhof. A. M., Hein, U.F. (2001). Fluid inclusion petrography. Lithos, 55, 27-47

Vezzani, L., Festa, A., & Ghisetti, F. (2010). Geological-structural map of the central-southern Appennine (Italy). *Geological society of America, 469.* DOI: 10.1130/2010.2469

Vespasiano, G., Apollaro, C., De Rosa, R., Muto, F., Larosa, S., Fiebig, J., Mulch, A., Marini, L. (2015). The Small Spring Method (SSM) for the definition of stable isotope–elevation relationships in Northern Calabria (Southern Italy). *Applied Geochemistry 63, 333–346.* https://doi.org/10.1016/j.apgeochem.2015.10.001

Wang, Y., Chen, J., Li, S., Wang, S., Shi, D., & Shen, W. (2022). Coseismic fluid–rock interactions in the Yingxiu–Beichuan surface rupture zone of the Mw 7.9 Wenchuan earthquake and their implications for the structural diagenesis of fault rocks. *Journal of Structural Geology 159.* DOI: 10.1016/j.jsg.2022.104603

Wasowski, J., Pierri, V., Pierri, P., Capolongo, D. (2002). Factors controlling seismic susceptibility of the Sele valley slopes: the case of the 1980 Irpinia earthquake re-examined. Surv. Geophys. 23 (6), 563–593.

Williams, R.T., Goodwin, L.B., Sharp, W.D., Mozley, P.S., 2017. Reading a 400,000-year record of earthquake frequency for an intraplate fault. *Proc. Natl. Acad. Sci.114, 4893–4898.* DOI: 10.1073/pnas.1617945114

Wu, L. Y., Hu, R. Z., Li, X. F., Stuart, F. M., Jiang, G. H., Qi, Y. Q., Zhu, J. J. (2018). Mantle volatiles and heat contributions in high sulfidation epithermal deposit from the Zijinshan Cu-Au-Mo-Ag orefield, Fujian Province, China: Evidence from He and Ar isotopes. *Chemical Geology, 480, 58–65.* DOI: 10.1016/j.chemgeo.2017.08.005

Zhang, M., Guo, Z., Xu, S., Barry, P, H., Sano, Y., Zhang, L., Halldorsson, S. A., Chen, A. T., Cheng, Z., Liu, C. Q., Lian Li, S., Lang,Y-C., Zheng, G., Li, Z., Li, L., Li, Y. (2021). Linking deeply-sourced volatile emissions to plateau growth dynamics in southeastern Tibetan Plateau. *Nature Communications, 12, 4157.* https://doi.org/10.1038/s41467-021-24415

Zhang, K, J., Huan Li, Q., Long Yan, l., Zeng, Lu., Lu, Lu, Xiu Zhang, Y., Hui,J., Jin, X., Chun Tang, X. (2017). Geochemistry of limestone deposited in various plate tectonic settings. *Earth-Science Reviews 167, 27-46.*

Zummo, F., Agosta, F., Alvarez-Valero, A. M., Billi, A., Buttitta, D., Caracausi, A., Cranevale, G., Marchesini, B., Paternoster, M. (2024). Tracing a mantle component in both paleo and modern fluids along seismogenic faults of southern Italy. *Geochemistry, Geophysics, Geosystems, 25*. DOI: 10.1029/2024GC011816